Atomistic simulation of dealloying-made microstructures

Vom Promotionsausschuss der Technischen Universität Hamburg

zur Erlangung des akademischen Grades

Doktor-Ingenieur (Dr.-Ing.)

genehmigte Dissertation

von

Yong Li

aus

Hunan, China

2023

Erstgutachter: Prof. Dr.-Ing. Jörg Weissmüller
Zweitgutachter: Prof. Dr. rer. nat. Gerold Schneider
Vorsitzender: Prof. Dr. rer. nat. Patrick Huber

Tag der mündlichen Prüfung: April 27, 2023
Digital object identifier (DOI): 10.15480/882.5119

Acknowledgments

During my doctoral study, I received support and help from many people. I would like to express my deepest gratitude and appreciation for all of your invaluable support and guidance throughout my doctoral journey.

First of all, I would like to express my heartfelt gratitude to my supervisor, Prof. Jörg Weissmüller for providing me with this opportunity to study such a fascinating topic. I also appreciate his exceptional guidance, continuous encouragement, and insightful feedback throughout the entire research process. During our frequent discussions, I learned not only the methods and knowledge of scientific research, but also the philosophy behind it. I am truly grateful for his patience, enthusiasm, and willingness to share his wisdom and expertise.

I would also like to express my sincere appreciation to Dr. Bao-Nam Dinh Ngô for his guidance and discussion especially on programming and simulation. This helped me get started very quickly on my research. I would also like to thank Dr. Jürgen Markmann for his continuous support and patient discussion. His expertise and insights have significantly broadened my understanding of the subject matter.

In particular, I want to thank Prof. Gerold Schneider for reviewing this study and for his thoughtful suggestions for my thesis. I also want to thank Prof. Patrick Huber for being the chairman of the examination.

I want to acknowledge the support from Haide Alfort-Springer and Dr. Robert Günther in official matters over the past few years. My sincere thank also goes to my colleagues at Helmholtz-Zentrum Hereon and at Hamburg University of Technology: Shan Shi, Nadiia Mameka, Stefan Berger, Lukas Lührs, Benedikt Roschning, Birthe Zandersons, Xinyan Wu, Gideon Henkelmann. I am grateful for their advice, feedback and contributions to my research.

Finally, I am deeply appreciative of my parents, my wife and my daughter for their unwavering support, encouragement, and understanding. Their belief in my abilities and motivating words are sources of strength and inspiration.

The financial support from FOR2213 "NAGOCAT" and Hamburg University of Technology for this study is greatly appreciated.

Abstract

Nanoporous gold (NPG) prepared by dealloying forms as bicontinuous networks of nanoscale ligaments and offers opportunities for fundamental studies of the mechanics, thermodynamics, and kinetics at the nanoscale. The microstructural features of the nanoporous structure impact the functional and mechanical behavior of the material. In this thesis, kinetic Monte Carlo (KMC) and Molecular Dynamics (MD) simulation methods were used to explore the evolution of those microstructural features, such as the residual less noble component (silver in the silver-gold system) content, characteristic length scale, as well as the topological connectivity.

By using KMC dealloying model, the evolution of residual silver and silver clusters during dealloying was studied. The dissolution and diffusion events were implemented in the KMC algorithm to mimic the dealloying process in experiments. For the first time in the atomistic simulation, this work demonstrates the dealloying contains two dealloying stages: i) the primary dealloying stage generates the 3D bicontinuous network; ii) the secondary dealloying stage further removes residual silver and coarsens the ligaments. The secondary dealloying stage is for the first time investigated independent of the primary delloying. It is challenging to isolate the primary and secondary dealloying in experiments. It is found that the primary dealloying process embeds silver clusters in ligaments and coats their surfaces with a passivation layer of gold. Secondary dealloying leads to a decrease in cluster numbers as ligaments become coarser.

The evolution of the characteristic length scale during dealloying and coarsening was explored. The size of silver clusters and ligaments was analyzed for KMC dealloying simulation generated structures. The silver cluster size retains constant during the whole dealloying process and scales with the ligament size of structure at the end of primary dealloying. Our findings emphasize the size of the surviving silver clusters as an experimental marker of the initial structure size. The coarsening process of NPG was investigated by applying KMC simulation without atom removal, i.e. only surface diffusion of gold atoms was an active process. Microstructures of NPG with different solid fractions, φ, were generated by the leveled-wave model, a method based on leveled Gaussian random fields by superposing standing sinusoidal waves with random phase and direction but constant wavelength. The findings of the coarsening simulations confirm the classical time exponent $t^{1/4}$ for the size evolution and underline that the characteristic spacing size, $\tilde{L}$, is more inherently linked to the coarsening kinetics than the ligament diameter, L_{ap}. The findings in this work provided a conclusive confirmation on the huge scattered experimental results of the coarsening law of NPG.

Based on the results of our simulations, an important finding was revealed that φ is a significant factor in the evolution of NPG networks' connectivity. The connectivity, g, when $\varphi \geqslant 0.30$ during dealloying, evolves sensibly along with the g-φ curve of the

leveled-wave model, whereas g diminishes when $\varphi < 0.30$ for structures dealloyed from the parent alloy of $Ag_{75}Au_{25}$. The volume shrinkage process of NPG was studied by using MD relaxation simulations on leveled-wave model generated NPG microstructures with different φ. Our results show a larger volume contraction as φ is reduced. There is no apparent increase of connectivity when $\varphi \geqslant 0.3$ but substantial enhancement when $\varphi = 0.2$. The connectivity of coarsened structures was also analyzed. As the coarsening process progresses, structures with $\varphi < 0.3$ tend to become increasingly disconnected, while those with $\varphi \geqslant 0.3$ maintain their connectivity.

Overall, this thesis explored the evolution of three important microstructural features of nanoporous networks: the residual less noble component, characteristic length scale, and topological connectivity. Our findings revealed several fundamental insights about nanoporous structures and can provide solid signatures to the experiments.

Contents

List of Figures

List of Tables

Chapter 1

Introduction

1.1 Microstructural features of nanoporous metals

The properties of a material are always governed by the specific arrangement of its constituents [1]. The arrangement of material constituents, including dimension, shape and the spatial distribution of elements, phases, orientations, and defects, is grouped under the term microstructure [1]. The microstructure contains all the characteristic structural features of the material on a scale larger than that of the individual atoms, but smaller than the overall size of the component. Those microstructures are impacted by the element composition, production process and condition under the services of the material. The characteristic length scale is one of the most fundamental microstructural parameters for materials, e.g. the grain size in the crystalline metals. The most well-known example of how the length scale dominates the properties of a material is that of polycrystalline materials with small scale grains have higher strength than coarse-grained ones–the Hall-Petch expression,

$$\sigma_y = \sigma_0 + k_y d^{-1/2} \tag{1.1}$$

where σ_0 and the Hall-Petch constant, k_y, varies for different materials. The yield strength, σ_y, increases with grain size, d, decreasing. The mechanism of this grain refinement strengthening phenomenon is the high proportion of grain boundaries in the fine-grained material hinder the motion of dislocations [2].

If the length scale changes to nanometer size, such as nanostructured materials, many novel properties and functions will emerge for the material. Nanoporous metals (NP metals) are one kind of these nanostructured materials being studied extensively in recent years. The nanoporous metals can be fabricated by means of a self-assembling method, namely the method of dealloying. Dealloying is the selective corrosion of one or more constituents from a solid solution. To date, numerous of NP metals have been reported: the nanoporous noble metals, such as Au [3–6], Pt [7], Pd [8, 9], Ag [10] and the nanoporous cost-efficient metals, such as Cu [11, 12], Fe [13], Al [14, 15], Mg [16]. Recently, there are also nanoporous high entropy metals reported [17–19]. Typically, NP metals have these following microstructural features in common:

- The bi-continuous network of the solid branches (ligaments). Figure 1.1 shows the open porous nanostructured network of as-dealloyed and coarsened nanoporous gold (NPG) [20].

- Tailorable microstructure with which the length scale can be tuned self-similarly from several nanometers to hundreds of nanometer by thermo-coarsening (Figure 1.1) [21, 22], and the solid fraction, φ, can be changed between 0.2-0.5 by controlling the composition of the parent alloy [23, 24].

- Extraordinary high surface-to-volume ratio owing to the nanometer length scale, a value of $10^8\,\mathrm{m}^{-1}$ can be achieved for NPG [25]. The high fraction of surface atoms with low coordination provide a huge amount of active sites for functions for the NP metal [26–28].

- Tunable amount and spatial distribution for the residual less noble component. For instance, for NPG prepared from Ag-Au alloy, the residual Ag atom fraction in the as-dealloyed NPG varies between 0.60 to 0.02 [29, 30] and the spatial distribution can be changed during thermo annealing [31].

- The topological connectivity, g, (will be defined in Section 2.4) of as-dealloyed NPG depends on φ with decreasing g as φ decreases [32]. At a critical value of $\varphi^{\mathrm{p}} = 0.159$, there is a percolation-to-cluster transition. NPG structures with $\varphi < \varphi_{\mathrm{p}}$ are composed of isolated clusters and have $g = 0$.

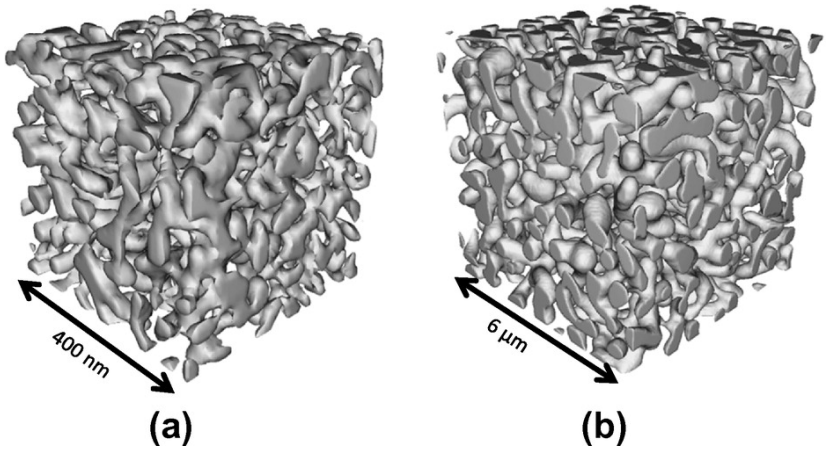

Figure 1.1: 3D-focused ion beam reconstruction of NPG. (a) NPG produced by dealloying with ligament size, L = 26 nm. (b) NPG after coarsening with L = 420 nm. Reprinted with permission from Ref [20]

A diverse range of functional applications have been proposed in various fields for nanoporous metals, such as actuators [8, 26, 33–35], sensors [36–38], bioanalytical system and bioseparations [39–41], catalysts [27, 42, 43], and energy storage [28, 44, 45]. As nanosize length scale ligaments network, the NP metals also provide a platform for the fundamental studies of small-scale mechanics [4, 6, 46–49], thermodynamics and kinetics [9, 50, 51].

By multi-scale designing, hierarchical nanoporous metals create an additional dimension for functionality [10, 52, 53] and stronger lightweight materials [54]. The microstructures have an important influence on the applications and mechanical properties of NP metals. For example, during annealing, the surface area of NP metal will

be reduced which will affect those functionalities based on the large surface area. Meanwhile the ligament size will increase during annealing and the change of length scale will also change the mechanical properties because of the Hall-Petch smaller-stronger effect. This thesis will, taking NPG as a model system, focus on the microstructure evolution of the nanoscale network for: i) residual less noble element–the composition and distribution, ii) characteristic length scale and iii) topological connectivity.

1.2 Residual silver of as-dealloyed NPG

Generally, the as-dealloyed NPG samples, by dealloying Ag-Au master alloy, comprise some residual Ag. At the beginning of dealloying, the dissolution starts from the low-coordinated Ag atoms on the surface of master alloy. Rather immediately the Au atoms aggregate and passivate large parts of the surface [55]. The passivation Au layer on the surface of the ligaments hampers the further dissolution of Ag atoms inside ligaments. As a result, there are Ag atoms left in the as-dealloyed NPG. The NPG prepared by dealloying contains residual Ag with atom fraction, $x_{\mathrm{Ag}}^{\mathrm{res}}$, in the range of 0.60 to 0.02 [29, 30]. As shown in Figure 1.2, the 3D reconstructions of an NPG structure by means of element-sensitive, transmission-electron-microscopy-based tomography and atomic simulation reveal that residual Ag takes the form of clusters [31]. These silver clusters are buried in the ligaments and maintain the precursor alloy's composition, while Au covered the surface of these ligaments. The spatial distributions of elements and phases are important aspects that characterize the microstructure. For NPG, the microstructure of silver clusters, i.e. the composition and spatial distribution, is of relevance. The residual Ag has a significant impact on the functionality, mechanical properties, and dealloying process of NPG.

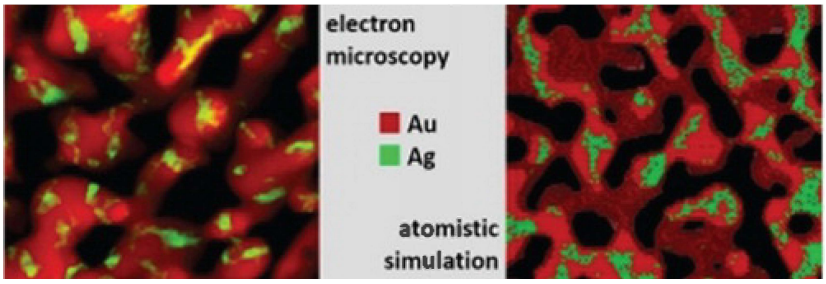

Figure 1.2: Comparison of TEM reconstruction and atomic simulation for spatial distribution of silver clusters in NPG. Reprinted with permission from Ref [31].

Residual Ag has been shown to have beneficial effects on NPG elastic properties in [56]. The surface-enhanced Raman scattering (SERS) of NPG is reinforced by residual Ag [57]. The effect of residual Ag in NPG which serves as a heterogeneous catalyst is case-dependent. The rate of CO oxidation drastically enhances as the residual Ag fraction increases [58, 59]. However, methanol oxidation shows an extreme loss of activity with increasing Ag fraction in NPG [60, 61]. The residual Ag also influences the corrosion process which is helpful to understand the dealloying mechanism. The concept of parting limit is well known in dealloying system: if the less noble content in the master alloy is lower than a certain, critical value, dealloying can not proceed

[62]. In the circumstance of multistep dealloying to generate hierarchical NPG (HNPG) with nested-network, controlling over the residual Ag during the first dealloying step is crucial for the tailoring of the microstructure of that kind of material [53, 63].

Usually, the spatial distribution of the residual Ag is of importance for the properties of NPG. The surface Ag atoms and their aggregation strongly affect the catalysis [27, 64, 65]. The multistep dealloying approach requires that the residual Ag is homogeneously distributed in the ligaments for the first dealloyed NPG, so that it can serve as a pattern for the second dealloying step [53, 63].

According to these observations, information in detail on the microstructural evolution of residual Ag and Ag distribution is crucial for understanding the mechanisms and properties of dealloyed NPG. The studies [31, 60] before this thesis revealed the existence of those silver clusters, leaving the evolution of these silver clusters unexplored. In this thesis, the evolution of silver clusters at different dealloying potentials was investigated via the dealloying simulations based on the kinetic Monte Carlo (KMC) method.

1.3 Length scale of NPG

1.3.1 Dealloying

During the dealloying process, less noble constituents are selectively removed from a solid solution by dissolution. Based on the kinetic Monte Carlo simulations (KMC), Erlebacher and co-authors [50, 55, 62, 66, 67] have established crucial definitions of the atomic-scale processes for the formation and evolution of the nanoporous network through the dealloying of Ag-Au alloy. Their numerical models simulated these main features of dealloying which are consistent with experiments, such as the porosity evolution [50], critical potential [55], parting limit [55], the characteristic size [67] and topology evolution [66]. At the beginning of the dealloying, the silver atoms are removed and Au atoms segregate to form islands with a distance comparing to a characteristic length scale. Those islands grow and are covered with a passivation layer of gold atoms. And then nanoporous networks form by undercutting and bifurcation. The layer coated with nearly passivated gold was imaged using atom probe tomography [68]. Surface gold layer prevents corrosion from attacking the buried areas of the host alloy. During the progression of the corrosion front into the primary alloy, the 3D structure of nanoporous network ligaments formed in the initial corrosion event (known as "primary dealloying" [29]) undergoes coarsening due to surface diffusion. This coarsening process, known as "secondary dealloying" [29], results in the redistribution of the Au component and gradual uncovering of buried areas, thus facilitating further dissolution of silver from the branches of network. The SEM image in Figure 1.3a shows the bicontinuous network of pore and solid phase of the microstructure of NPG, where the branch of the solid phase is referred to as a "ligament". Additionally, the large grain size of several tens of micrometers in NPG can be identified from Figure 1.3b. The crystal lattice orientation and grain size are inherited from the master alloy after dealloying [69]. There are around 10^9 nano-ligaments in each grain [6]. The characteristic length scale of nanoporous gold (NPG) is defined by the size of its ligaments or pores, rather than its grain size.

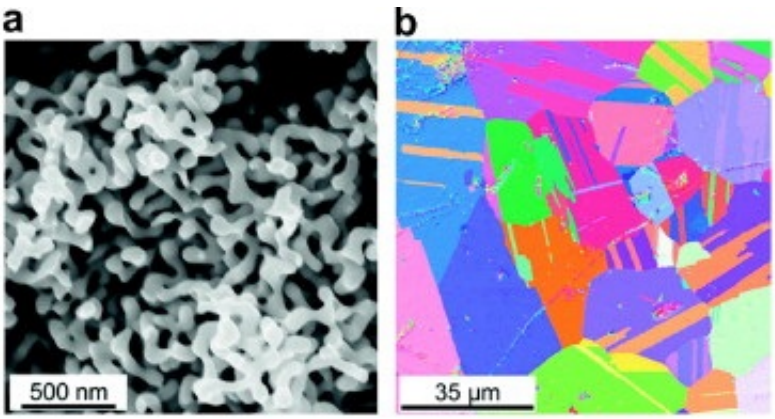

Figure 1.3: Microstructure of NPG. (a) NPG prepared by dealloying with ligament size, L = 55 nm. (b) Grains are shown in EBSD orientation map. The large grains have size of 10-100 μm with around 10^9 nanosize ligaments in each grain. Reprinted with permission from Ref [6].

Normally the initial length scale of porous structures created during the dealloying process (primary dealloying), which is important to understand the mechanism of dealloying, is difficult to measure because of the fast coarsening during secondary-dealloying even at room temperature. In-situ small angle X-ray scattering (SAXS) on the Ag-Au dealloying system shows that the initial characteristic peak on the SAXS pattern forms very fast and the initial length scale calculated from the peak position is a few nm [70]. The length scale increases during dealloying and evolves to a stable status at which the size is several tens of nm. Typically, the as-dealloyed NPG sample at room temperature shows 20-40 nm of ligament size. The porous structure is controlled by the competition in the dissolution-diffusion process. Thus the length scale of as-dealloyed nanoporous gold (NPG) can be tailored by controlling the applied potential and corrosion medium to manage the dissolution process and change the diffusivity of the more noble element. The ligament size of as-prepared NPG can also be tuned to below 5 nm by changing the dealloying temperature. The mechanism behind this is the much slower surface diffusion of gold when temperature changes from 25 ℃ to -20 ℃ [71, 72]. The length scale for an as-dealloyed NPG is 8 nm after dealloying for 5 min but it coarsened to 15 nm after 20 min. This coarsening is caused by the faster diffusion of gold in the nitric acid (70%) electrolyte [73]. The length scale of as-dealloyed NPG dealloyed at room temperature can also vary between 8 nm – 67 nm by changing the surface diffusivity of gold with additional halides in the electrolyte [73, 74]. The length scale can be below 10 nm for as-dealloyed NP noble metals with lower surface diffusivity, such as Pt [75] and Pd [76].

There is 0.02-0.6 fraction of residual silver formed as silver clusters in the as-dealloyed NPG (for a detailed discussion see Section 3). The silver content decreases during the dealloying due to the dissolution, but how the mean size of those silver clusters evolves is still unclear. The suggestion that they maintain their average size is yet to be verified [31]. This concept is significant because it suggests that the clusters are indicative of the initial ligament structure that results from self-organization at the nanoscale during the primary dealloying process. However, the experimental data

on the size of the initial ligaments, which is an essential characteristic of the process, remains unclear. This is due to the fact that coarsening occurs simultaneously with dealloying, and even in situ experiments provide only an average picture on a microscopic scale. The size of an initial ligament cannot be isolated naturally as in situ experiments average over microstructure regions that are at different stages of corrosion and roughening, which may not accurately capture the size of the initial ligament in isolation. The secondary dealloying has never been purposefully studied in KMC simulations (because it takes very much more time than primary dealloying, so this is computationally very expensive). In this thesis, the kinetic Monte Carlo (KMC) simulations of dealloying were used to isolate the primary dealloying and secondary dealloying. The evolution of length scale of ligaments and silver clusters in those two processes was studied separately. And the relationship between the two sizes will be also revealed.

1.3.2 Coarsening

NPG has a porous microstructure with interconnected ligaments and nodes. The coarsening process will change the microstructure of NPG. Particular microstructure alterations of NPG during coarsening encompass ligaments coarsening driven by surface diffusion [77], ligaments pinching off due to the Rayleigh instability [66] and specific surface area decrease resulting from minimizing overall surface energy [66, 78]. One focus of this thesis was to gain a comprehensive insights of the coarsening process in nanoporous metal networks.

Coarsening occurs during dealloying [71], post thermal annealing [77] and catalysis services [79]. Under the principle of structure determining function, a fundamental understanding of microstructural evolution in NPG during coarsening is critical for further tuning and optimizing their chemical, catalytic as well as mechanical properties. The tunable length scale can impact the properties of NPG significantly. It shows the ductule-brittle transition dominated by the length scale of NPG structure [77]. The effect of NPG's size on the surface-enhanced Ramn scattering (SERS) has been reported. This is illustrated by a remarkably enhanced SERS for the ultrafine NPG [80]. The stiffness of NPG drops as the length scale increases during coarsening and is sensitive to the solid fraction, φ, [23, 81–83].

According to Herring [84], for the thermal annealing process the length scale, L, scales with the time, t, following a coarsening law of $L \propto t^{1/n}$. Here n denotes the coarsening exponent. For a bulk-diffusion-dominated process, $n = 3$, while for the surface-diffusion-controlled process, $n = 4$. Qian et al. investigated the kinetics of pore size of NPG thin film with 0.35 initial Au fraction at the temperature of -20 ℃, 0 ℃ and room temperature [80]. The exponent, n, was identical for various temperatures with a value of $3.4-3.7$ which is very close to 4. Pia et al. reported the coarsening behavior of NPG with $\varphi = 0.30$ under thermal annealing at Ar flux condition [85]. The value of, l^4, here l is length scale, shows a linear function of annealing time, t, indicating a value of 4 for n. Nakatani et al. compared the kinetics of NPG coarsening in air and vacuum for a $\varphi = 0.35$, 100 nm thick NPG thin film [86]. The measured coarsening exponent, n, is 4.8 ± 1.9 and 5.7 ± 1.4 for annealing in air and vacuum respectively. The values of n are compatible with the exponent for surface diffusion $n = 4$ but the very small thickness

of the film used in [86] which is comparable with the length scale may influence the kinetics. Chen-Wiegart et al. used X-ray nanotomography to study the coarsening process in air of cylindrical NPG sample [87]. The length scale of NPG denoted by the inverse of the specific surface area, $1/S_{\mathrm{A}}$, shows no clear exponential increasing function versus annealing time, t. But the calculated activation energy value, Q, shows good agreement with Q of gold surface diffusion.

The aforementioned studies failed to provide a conclusive picture of the kinetic parameter on the coarsening of NPG. Another aspect that coarsening behavior for varying φ, an important parameter especially to the mechanical properties of NPG, has not been systematically discussed at the onset of this thesis. In this thesis, the coarsening behavior was studied based on KMC simulations with model parameters fitted to experimental NPG. The leveled-wave modulation (Section 2.1.1) was chosen to generate initial structures that matched the as-dealloyed NPG and have different solid fractions covered the range of experimental prepared samples. The relatively large size of simulation boxes were used to minimize the influence of their finite size on the simulations.

1.4 Topological genus– the connectivity

Studying the mechanical properties of NP metal is of relevance. Not only because of the mechanical stability or good performance required for the nanoporous metals to serve as functional or structural materials but also because their nanoscale networks provide a model system for fundamental mechanical studies at small-scale [83]. A number of studies have shed light on the determinants of small-scale plasticity, such as size [4, 6, 46, 47, 88, 89] and surface effects [90–92]. In addition, the studies on the mechanical properties of nanoporous metals have also brought attention to the role of nanoporosity in stress corrosion cracking [93, 94]. Typically, the discussion often revolves around defining microstructural parameters such as ligament size, L, and solid fraction, φ. Yet, there are contradictions among experimental results for strength or stiffness that indicates the mechanical behavior probably be influenced by additional parameters [20, 82, 83, 95]. A strong influence on the mechanical behavior of the network has therefore been noted by highlighting its connectivity [82, 96–98], which will be defined in Section 2.4, as an additional, important microstructural characteristic of NP metal [66].

The decrease in connectivity as φ decreases can be employed to account for the unexpectedly low effective Young's modulus, Y^{eff}, of as-dealloyed nanoporous metals [82, 99]. Yet, it was not able to demonstrate that the coarsened NPG samples have much larger Y^{eff} scatter at lower φ [82, 100, 101]. Erlebacher's pioneering work [66] reported the mechanism underlying the decrease in network connectivity during coarsening. The curvature-driven redistribution of matter by surface diffusion tends to pinch-off ligaments caused by the Plateau-Rayleigh instability. Simulating spinodal decomposition [96, 99, 102, 103], which can also lead to coarsened microstructures, has been used to create atomistic and finite-element models of NPG. Given the fact that connectivity affects mechanics, it is prompted to investigate the connectivity evolution during the coarsening process.

There are contradictory results in the experiments on the above topic. During

coarsening, the decreasing Young's modulus indicates that the number of disconnected ligaments increases dramatically [82]. Liu et al. argued that the rapid reduction of connectivity, caused by ligaments pinch-off during coarsening, dominated the anomalous low strength in NPG because these disconnected or dangling ligaments will not contribute to the instant strength and stiffness at macroscale. A parameter of the ratio between the effective solid fraction and solid fraction was defined to quantify the network connectivity in NPG. It was found that the defined network connectivity decreased rapidly during coarsening associated with lowered strength and stiffness.

Tomographic reconstructions of NPG, however, seem to be contrary to the above conclusion: there are constant numbers of connections in each representative component of the volume element, regardless of the ligament size, i.e. coarsening process follows a self-similar pattern [20, 104–106]. Hu et al. 3D reconstructed the network structure of annealed NPG samples with various ligament sizes of 15 – 400 nm via focused-ion-beam sectioning (FIB) method [20]. They demonstrated that the connectivity of NPG structures with different ligament sizes have almost the same value while the corresponding strengths evaluated by FEM simulation were an order of magnitude lower than the prediction from the Gibson-Ashby law. Kwon et al. investigated topology evolution during coarsening with higher mixture volume fractions of 0.36-0.50 [105, 106]. Similar results of invariant evolution of connectivity during coarsening for various volume fractions were documented.

In their review paper [95], Mameka et al. incorporated one parameter of the load-bearing paths denoted as C_c to access the network connectivity in NPG. A hypothesis was established that C_c would decrease substantially at low solid fraction instead of staying invariant at all solid fractions and there is a threshold below which the network of NPG structure becomes discontinuous. This hypothesis was verified by Soyarslan et al. [32]. They developed a random field method to generate numerical NPG structures which matched the experiments very well. The connectivity for as-created random field structures decreases as solid fraction decreases. Furthermore, there is a solid percolation threshold of $\varphi^{\mathrm{p}} = 0.159$. They found that when the solid fraction falls below φ^{p}, the connectivity of the network decreases to 0, resulting in the formation of many isolated particles. Results of network connectivity in NPG decrease as solid fraction decrease and ligaments coarsen are inconsistent with the invariant evolution observed by Hu and Kwon. Therefore, on the controversy over whether the evolution of network connectivity during coarsening is invariant, further studies are worth being carried out.

An analysis of the topology of kinetic Monte Carlo simulated nanoporous nanoparticles during coarsening by surface diffusion has been performed [66]. Massive solids without porosity are finally formed from these nanoporous particles. As a result of an analogous process, nanoporous metal forms denser layers near its surface [107]. Since the surface densification of the particles has no counterpart in the interior of the network, it is not valid to deduce the observations on the coarsening of nanoparticles in Ref.[69] to bulk network structures.

Simulations exploring how solid fractions, φ, influence the connectivity evolution in the bulk network, based on realistic network geometries and surface diffusion-induced coarsening, have not been reported yet. In Section 5.3, the connectivity of those structures generated by KMC coarsening simulations in Section 4.2 were calculated.

The evolution of connectivity during coarsening for NPG structures with different φ will be exhibited. The impact of temperature on connectivity evolution will be also discussed.

Compared to the surface diffusion-controlled coarsening process of NPG, as introduced in detail in Section 3.2, the establishing 3D network at primary dealloying, and simultaneous dealloying and coarsening at secondary dealloying make the dealloying process more complex. The relationship between φ and connectivity for as-dealloyed NPG has been established by networks based on the early-stage spinodal decomposition [32]. However, dealloying is a process with corrosion of less noble component and formation of porous due to the diffusion of more noble component, that process is different with the spinodal decomposition process which describes the spontaneously phase separation from a single phase without barrier. Also, the connectivity evolution during dealloying is still unrevealed. In this context, it is worth studying the evolution of connectivity during dealloying with respect to consider the detailed process of dealloying. In Section 5.1, based on the analysis of the connectivity for structures produced by KMC dealloying simulations in Chapter 3, the evolution of connectivity during dealloying is explored for different Au fraction in the master alloy.

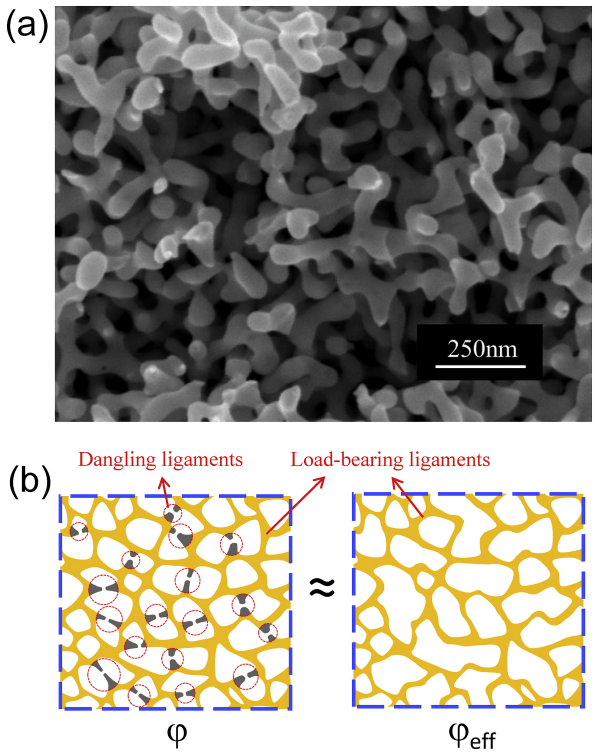

Figure 1.4: Dangling ligaments and loard-bearing network of NPG. (a) Scanning electron microscope (SEM) image of as-dealloyed NPG with solid fraction 0.25. (b) The broken/dangling ligaments in NPG and the effective load-bearing network. Reprinted with permission from Ref [82].

As shown in Figure 1.4 there are numerous broken or "dangling" ligaments which can not contribute to the effective load-bearing network in NPG prepared from $Ag_{75}Au_{25}$ [82]. The findings from the study on the evolution of connectivity during coarsening (Section 5.3) indicate that during coarsening, nanoporous networks with a

solid fraction of $\varphi \geqslant 0.30$ are more likely to preserve their connectivity, while those with $\varphi < 0.30$ are prone to reduce their connectivity. The observation of different evolution of connectivity for structures with different φ implicates that the number of "dangling" ligaments in the network also depends on φ. The dealloying process can lead to a volume shrinkage of as much as 30 vol%, depending on the Au fraction in the master alloy [69, 108–110]. It can be expected that the volume shrinkage will result in a re-connecting of these "dangling" ligaments, therefore increasing the connectivity of the as-dealloyed NPG. To verify this assumption, in Section 5.2, MD relaxation simulations of NPG networks with various φ will be conducted to investigate the connectivity evolution during shrinkage and the impact of φ on it.

1.5 Outline of the thesis

The following chapters outline this thesis:

Chapter 2 provides the basic conceptions of sample preparation, simulation methods, and data analysis. The methods and background for initial configurations are described in detail. The simulation procedures of kinetic Monte Carlo (KMC) and Molecular Dynamics (MD) methods used in this thesis are introduced. And the details of the algorithm and setting up for simulations are also illustrated. To characterize the length scale, different methods have to be used depending on the configuration of data analyzed. Those characteristic size calculation methods are given in chapter 2. The last section of this chapter focuses on the definition and calculation process of connectivity.

Chapter 3 focuses on the results of the composition profile and residual Ag evolution during dealloying. The details of dealloying concerning the dissolution flux density and two steps of dealloying are discussed in the first two sections of this chapter. Followed by the results of the composition profile and morphology of Ag distribution during dealloying.

Chapter 4 concentrates on the results of the characteristic length scale evolution. This chapter is divided into two sections to present the results of size evolution during dealloying and coarsening. The first section explores the evolution of the mean size of silver clusters and ligaments during dealloying, while the second section exhibits the evolution of morphology and characteristic size during coarsening.

Chapter 5 mainly deals with the connectivity evolution. Three sections corresponding to connectivity evolution during dealloying, shrinkage and coarsening are comprised in this Chapter.

In the final chapter, the main findings of this thesis are summarized and future possible studies are outlooked.

Chapter 2

Methods

2.1 Sample preparation

2.1.1 Leveled-wave configurations

Essentially, during dealloying, nanoporous structures are formed as a result of a chemical corrosion process at the interface between the solid and the corrosion medium, which results in increasing surface area over time [50]. An efficient and convenient numerical stochastic nanoporous microstructures generation algorithm–the leveled wave modulation, which originated from spinodal decomposition [111], was proposed by Soyarslan et al. [32].

Using the leveled-wave modulation approach, random bicontinuous networks can be generated that represent as-dealloyed NPG in a realistic manner. They have an isotropic Young's modulus and match experiments well for $\varphi = 0.25 - 0.45$. As well, the connectivity of these networks is consistent with data derived from FIB tomographic reconstructions of NPGs [20, 32]. The characteristic length scale indicated by the evident interference peak of the small-angle scattering experiments of NPG [112, 113] is also presented by the fixed characteristic wavelength in the leveled-wave algorithm.

In this thesis, the initial configurations for simulations of coarsening and shrinkage were defined based on the leveled-wave model [32]. In the leveled-wave modulation, a Gaussian concentration-field is generated by superimposing waves with the same wavelength and amplitude but stochastic orientation and phase. The leveled-wave model produces the microstructure at the end of early-stage spinodal decomposition [111].

It is demonstrated in the schematic Figure 2.1 that the leveled-wave model is carried out straightforwardly as described below.

The Gaussian concentration-field can be defined as:

$$c(\mathbf{r}) = \sqrt{\frac{2}{N}} \sum_{i=1}^{N} \cos(\mathbf{q}_i \cdot \mathbf{r} + \phi_i), \tag{2.1}$$

where $\mathbf{r}$ denotes the position vector, ϕ_i represents the phase of each wave, and N is the total number of waves which is determined by wave vectors, $\mathbf{q}_i$.

Monte Carlo and Molecular Dynamics of atomic system are always used in assessing the properties of microscopic samples. An efficient way to simulate the bulk phase is to

choose boundary conditions that simulate the existence of an infinite body surrounding the system to be studied. Periodic boundary conditions are usually used to fulfill this [114]. To achieve periodic NPG microstructures, it is essential to select finite waves with integer wavenumbers in different direction and fixed modulus:

$$\mathbf{q}_i = \frac{2\pi}{b}(h_i\mathbf{e}_1 + k_i\mathbf{e}_2 + l_i\mathbf{e}_3), \tag{2.2}$$

where b represents the edge length of the simulation box, the set of unit vectors $\{\mathbf{e}_i\}$ constitutes an orthonormal basis in the reciprocal space, the defined tuples (h_i, k_i, l_i) is restricted to integers which are selected in the manner of a constant magnitude, H, obtained. Therefore,

$$H = \sqrt{h_i^2 + k_i^2 + l_i^2} = \text{const.} \tag{2.3}$$

The wave vectors, $\mathbf{q}_i$, defined in this way have the identical modulus,

$$q_0 = \frac{2\pi H}{b}. \tag{2.4}$$

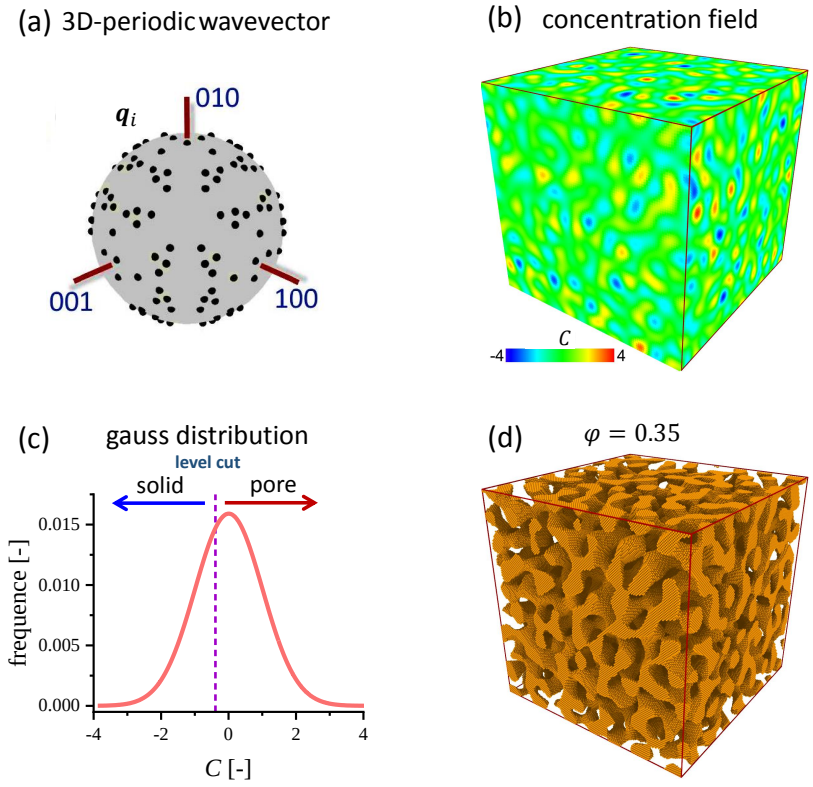

Figure 2.1: Schematic of leveled-wave modulation to generate nanoporous structure. (a) the orientation of uniformly distributed wavevectors, $\mathbf{q}_i$, projected onto the unit sphere in the reciprocal space, (b) Gaussian concentration-field, (c) the gauss distribution of concentration and tuning the solid fraction by choosing different level-cut, (d) Rendering of the produced NPG microstructure with solid fraction of φ= 0.35 by mapping the concentration field to a FCC lattice.

Figure 2.1a demonstrates the uniformly distributed orientation of 120 wave vectors on the unit sphere in the reciprocal space. These wave vectors are selected with $H = \sqrt{449}$.

The concentration-field, as shown in Figure 2.1b, is then generated by adapting, $\mathbf{q}_i$, from Eqs. 2.2-2.3 and wave phases, ϕ_i, chosen randomly in the range of $[0, 2\pi]$.

The generated random field is then mapped onto a face-centered cubic (fcc) lattice with the gold lattice constant 408 pm. Then it is binarized into solid and pore phases by selecting a level cut on the Gaussian distribution of concentration. Figure 2.1c illustrates the selection of level cut.

Finally, the desired bicontinuous nanoporous gold network is produced. The solid fraction, φ, can be tuned by changing the corresponding value of level cut. Figure 2.1d shows such a NPG structure with a random bicontinuous network.

2.1.2 Definition of ligament size

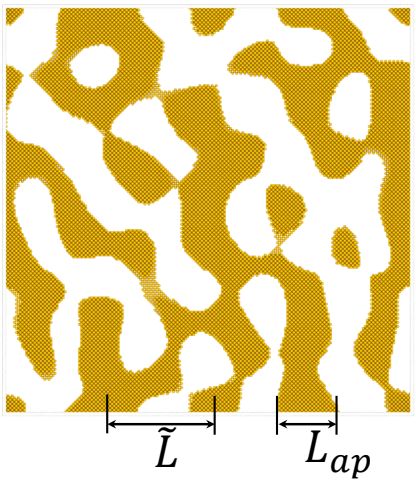

Figure 2.2: Charaterisitic sizes of NPG. the ligament spacing size, $\tilde{L}$, denotes the mean distance between the centers of neighboring ligaments; the apparent ligament size, L_{ap}, represents the mean diameter of ligaments.

As shown in Figure 2.2, two kinds of ligament size were defined to characterize the length scale of the modeled NPG structures, the apparent ligament size, L_{ap}, and the spacing size, $\tilde{L}$. The L_{ap} is the mean diameter of ligaments which is an equivalent but more descriptive parameter than the surface area, S_{V}. Whereas, $\tilde{L}$, determined via Eq. 2.25, represents the characteristic spacing between the centers of neighboring ligaments. See Section 2.3.2 for detail calculation procedure.

2.1.3 Sample preparation for coarsening simulations

Simulations of coarsening were run on a rigid face-centered cubic (fcc) lattice with a = 408 pm of gold atoms as the lattice parameter (the same value of a was used for Section 2.1.4 and Section 2.1.5). The initial structures have the cubic simulation boxes with edge length, $b = 200a$ = 81.6 nm. To reveal the impacts of the finite size of simulation boxes on the coarsening behavior, another set of initial structures with $b = 400a$ was constructed. The fcc lattice simulation boxes with edge length $b = 200a$ and $b = 400a$ have 32 and 256 million sites, respectively.

Table 2.1: Parameters of the initial microstructures construction for the 900 K coarsening simulations: edge length of simulation box, b, solid fraction, φ, magnitude, H, and their features calculated from the microstructures: surface area per solid volume, S_V, apparent ligament size, L_{ap}, and characteristic spacing between neighboring ligaments, $\tilde{L}$. See Section 2.3.2 for the definition of S_V, L_{ap} and $\tilde{L}$. Note that H is selected for each microstructures to satisfy the identical number of waves, i.e. 120 waves and the identical L_{ap} for all structures.

b [nm]	φ [-]	H	S_V[1] [1/nm]	L_{ap}[1] [nm]	$\tilde{L}$[1] [nm]
81.6	0.22	$\sqrt{266}$	1.56	2.57	6.15
81.6	0.25	$\sqrt{306}$	1.58	2.54	5.74
81.6	0.27	$\sqrt{350}$	1.63	2.46	5.36
81.6	0.30	$\sqrt{386}$	1.62	2.48	5.11
81.6	0.35	$\sqrt{449}$	1.59	2.51	4.74
81.6	0.40	$\sqrt{525}$	1.57	2.55	4.38
81.6	0.45	$\sqrt{649}$	1.59	2.52	3.94
81.6	0.50	$\sqrt{754}$	1.55	2.57	3.66

Table 2.2: Same parameters and features as Table 2.1, but for the simulations with T = 1800 K. The microstructure denoted by 0.35^* refers to larger simulation box with edge length of $b = 400a$. Note the same $\tilde{L}$ for all structures.

b [nm]	φ [-]	H	S_V [1/nm]	L_{ap} [nm]	$\tilde{L}$ [nm]
163.2	0.25	$\sqrt{449}$	1.91	2.09	4.74
163.2	0.30	$\sqrt{449}$	1.74	2.30	4.74
163.2	0.35	$\sqrt{449}$	1.59	2.51	4.74
163.2	0.35^*	$\sqrt{1817}$	1.60	2.50	4.71
163.2	0.50	$\sqrt{449}$	1.20	3.33	4.74

The parameters of magnitude, H, and solid fraction, φ, used in initial configurations generated by leveled-wave model for the coarsening simulations with temperature, T = 900 K and 1800 K are listed in Tables 2.1 and 2.2, respectively. The values of the surface area per solid volume, S_V, the apparent ligament size, L_{ap}, and spacing ligament size, $\tilde{L}$, of the corresponding generated initial configuration are also listed. The definition and calculation procedure of two sizes refer to Section 2.1.2 and Section 2.3.2, respectively. The set of initial structures listed in Tables 2.1 have the identical $L_{ap} = 2.53 \pm 0.06$ nm but various $\tilde{L}$. By contrast, the initial structures listed in Tables 2.2 have the same $\tilde{L}$ = 4.74 nm but different L_{ap}. The values of S_V, L_{ap}, and $\tilde{L}$, of the initial microstructures are analyzed by Eqs 2.26, 2.24, and 2.27, respectively.

Approximately 0.4 % of all atoms in the initial microstructure with φ = 0.22 are composed of 12 isolated small clusters. This phenomenon agrees with the percolation-to-cluster transition at a finite φ of 0.16 for the leveled-wave modulation [32]. Because

[1]Calculation details are provided in Section 2.3.2

the number of atoms in these isolated clusters is negligible, they are removed before inputted to simulations. There is only one cluster in all other initial samples.

Figure 2.3 shows the initial microstructures of leveled-wave generated NPG samples with φ of 0.25, 0.35, and 0.5. Random bicontinuous nanoporous networks are achieved. In Figure 2.3, it can be seen visually from the surface of the simulation box that the ligaments and pores are randomly distributed and the structures do not have any obvious texture. It is also seen that the denser structure has shorter ligaments and smaller pore size.

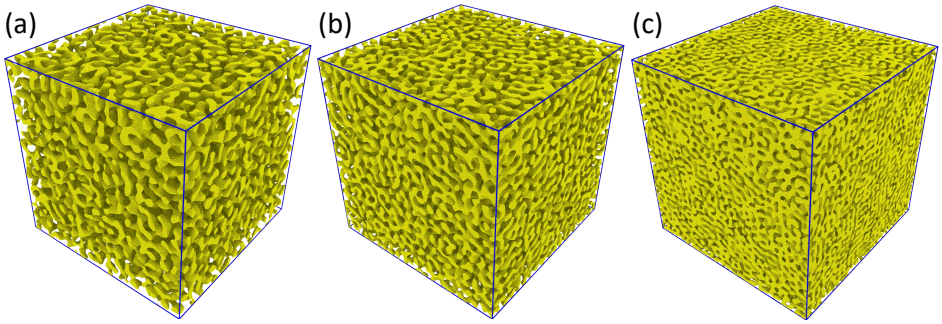

Figure 2.3: Rendering of initial, leveled-wave configurations. 120 waves were superimposed, and level cuts adjusted for solid fractions of 0.25 (a), 0.35 (b), and 0.50 (c). Edge lengths of the cubic simulation boxes are 200 lattice spacings..

2.1.4 Sample preparation for shrinkage simulations

The leveled-wave model introduced in Section 2.1.1 was used to generate the initial numerical nanoporous gold structures for molecular dynamics relaxation simulations of shrinkage. With the edge length, b = 81.6 nm, a cubic simulation box was generated with periodic boundary conditions applied in each direction. The generated microstructures, with solid fractions covering the range of 0.2 to 0.35, have identical ligament diameters of $L_{\mathrm{ap}} \approx 3.3$ nm (here, L_{ap} was calculated by Eq. 2.24 with the surface area per solid volume, S_V, derived from open-source software OVITO [115]). Tables 2.3 lists the solid fractions φ and the H values used to create these initial structures by means of the leveled-wave construction, as well as their information on the specific surface area, and sizes.

Table 2.3: Parameters of the initial microstructures construction for the shrinkage simulations. Same parameters and features as Table 2.1. Note the identical L_{ap}.

b [nm]	φ [-]	H	S_{V} [1/nm]	L_{ap} [nm]	$\tilde{L}$ [nm]
81.6	0.20	$\sqrt{125}$	1.21	3.3	6.15
81.6	0.25	$\sqrt{153}$	1.21	3.3	5.74
81.6	0.30	$\sqrt{182}$	1.21	3.3	5.11
81.6	0.35	$\sqrt{225}$	1.21	3.3	4.74

2.1.5 Initial configuration for dealloying

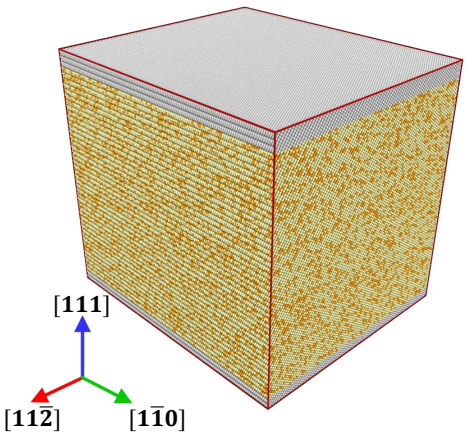

Figure 2.4: Initial configuration of random occupied fcc-lattice with composition $Ag_{75}Au_{25}$ for dealloying simulations. The simulation box is oriented in [111], [1$\bar{1}$0] and [11$\bar{2}$] direction with edge length of 30.1, 36.8 and 31.9 nm, respectively. Several layers of vacant sites are added on the top and bottom to set the free surface in direction [111]. The dealloying simulations for $Ag_{65}Au_{35}$ in Section 5.1 used the same parameter but only changed the fraction of random occupied Au atom sites. The rendered colors for Au, Ag and vacant sites are yellow, white and gray, respectively.

Figure 2.4 displays the initial configuration for the dealloying simulations in Chapter 3, Section 4.1and 5.1. Figure 2.4 shows a rectangular simulation box with face-centered cubic (fcc) lattice bound on three sides by faces of {111}-, {110}- and {112}-types. The [111] direction surface was kept free for corrosion and there are periodic boundary conditions in the lateral directions. There are several layers of vacant sites on the two {111} surfaces to allow the start of corrosion. The thickness of the simulation box ([111] orientation) is 30.1nm and the lateral edge lengths are 36.8 and 31.9 nm in the [1$\bar{1}$0] and the [11$\bar{2}$] direction, respectively. There are 2.1×10^6 atoms in the simulation box and it is randomly assigned with a net atom fraction of $Ag_{75}Au_{25}$ for the entire lattice. In Section 5.1, the connectivity evolution during dealloying is explored for different composition master alloy of $Ag_{75}Au_{25}$ and $Ag_{65}Au_{35}$. Except for the fraction of randomly occupied Au atoms changed to 0.35, the same parameters are used for the initial configuration of $Ag_{65}Au_{35}$.

2.2 Simulation methods

2.2.1 Kinetic Monte Carlo

In Monte Carlo simulations, the Metropolis approach [116] is commonly used. In this algorithm, at each step, a new configuration can be achieved from the old one depending on the variation of energy, ΔE. For an instance, Figure 2.5 displays a schematic of a swap step in Monte Carlo simulation on a simple cubic lattice, one atom o at state i can be chosen at random for moving to its nearest neighboring vacant sites to a new state j. Then the energy change, ΔE, of the swap is calculated.

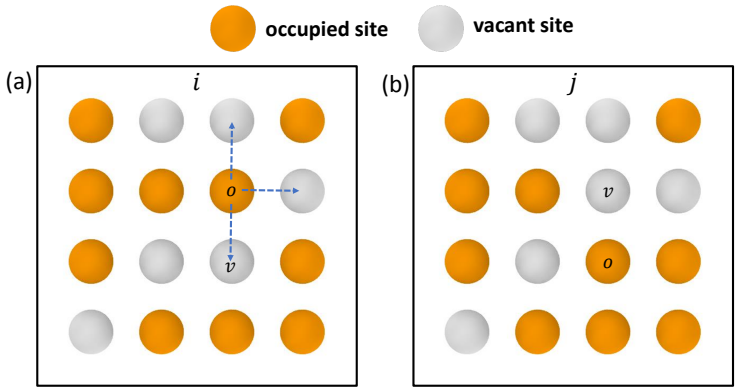

Figure 2.5: Schematic of a swap step in Monte Carlo simulation on a 2D simple cubic lattice. (a) is the old configuration state i. Atom o can move to its nearest neighboring vacant sites. (b) is the new configuration state j generated from state i by moving atom o to vacant site v. The site occupied by atom and vacant site are displayed in golden and gray, respectively.

For the Metropolis approach [117],

If $\Delta E < 0$, i.e. the swap is downhill in energy, the new configuration is accepted with probability of 1.

If $\Delta E > 0$, i.e. the swap is uphill in energy, it is accepted with probability of the Boltzmann factor of ΔE, $\exp(-\Delta E/k_{\mathrm{B}}T)$. Here, k_{B} and T represents the Boltzmann constant and the temperature, respectively. To do this, a random number $\rho \in (0, 1)$ is

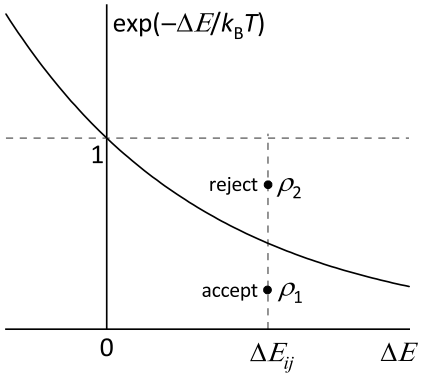

Figure 2.6: Acceptance criteria for uphill swap in Metropolis Monte Carlo simulations. Reprinted with permission from Ref [117]

generated. As illustrated in Figure 2.6, if $\rho < \exp(-\Delta E/k_{\mathrm{B}}T)$, the swap is accepted. Otherwise, the swap is rejected and the old configuration (i.e. state i) is returned to the chain as a new state.

The Metropolis algorithm will try to find the equilibrium state, i.e. the configuration with the lowest free energy. While the routine to reach an equilibrium state does not describe the physics of how the system evolves and how equilibrium is achieved. Thus, the real-time, t, is ignored in the Metropolis algorithm.

The kinetic Monte Carlo methods arise to simulate the evolution of a system over time and the systems pathway in configuration space in a physically meaningful way [118–121]. The KMC methods deliver a numerical solution to the Markovian master equation,

$$\frac{\partial P(i,t)}{\partial t} = -\sum_{j\neq i} r_{ij}P(i,t) + \sum_{j\neq i} r_{ji}P(j,t)\,, \tag{2.5}$$

where i and j are successive system states, $P(i,t)$ denotes the probability of the system to be in state i at time t, r_{ij} is the transition rate (the probability per unit time) of the system changing from state i to state j. The time derivative of Eq. 2.5, when the system is at equilibrium state, is zero. This leads to the rule of detailed-balance

$$\frac{r_{ij}}{r_{ji}} = \frac{P(j,\mathrm{eq})}{P(i,\mathrm{eq})}\,, \tag{2.6}$$

with $P(i,\mathrm{eq})$ the probability of the system being in state i at equilibrium state. In the canonical ensemble, there are the following thermodynamic averages [119, 120],

$$P(i,\mathrm{eq}) = \frac{1}{Z}\exp\frac{-E(i)}{k_{\mathrm{B}}T}\,, \tag{2.7}$$

where Z represents the partition function and $E(i)$ denotes the energy of the system. Eqs. 2.6 and 2.7 give

$$\frac{r_{ij}}{r_{ji}} = \exp -\frac{E(j)-E(i)}{k_{\mathrm{B}}T}\,, \tag{2.8}$$

Since there are many ways to fulfill the detailed balance, it is therefore that the transition rate, r_{ij}, can not be specified uniquely. For KMC simulations, two types of transition rates among those common choices which satisfy the detailed balance are [119, 121, 122]:

(a) The energy barrier, E_{ij}, in this type of transition rate, depends only on the energy, E_i, of the initial configuration i, see Figure 2.7a. In this case, E_{ij} equals to $-E_i$ and contains only the information of the old configuration i, without the information of the new configuration j. The transition rate can be written as,

$$r_{ij} = r_0\exp -\frac{E_{ij}}{k_{\mathrm{B}}T}\,, \tag{2.9}$$

where $E_{ij} = -E_i$ with E_i the total energy of configuration i and r_0 denotes the attempt frequency.

(b) The energy barrier, ΔE_{ij}, is the energy difference of the transition from configuration i to j, see Figure 2.7b. In this case, $\Delta E_{ij} = E_j - E_i$ includes the information both the old and new configuration during the transition [122]. The transition rate can be written in the way of Metropolis approach:

$$r_{ij} = \begin{cases} r_0 & \text{if} \quad \Delta E_{ij} < 0 \\ r_0 \exp -\frac{\Delta E_{ij}}{k_B T} & \text{if} \quad \Delta E_{ij} \geq 0 \,, \end{cases} \tag{2.10}$$

where $\Delta E_{ij} = E_j - E_i$ and E_i, E_j represent the total energy of configuration i and j, respectively. The attempt frequency, r_0, in Eqs. 2.9 and 2.10 can be obtained by a DFT calculation based on the Transition State Theory [119, 123].

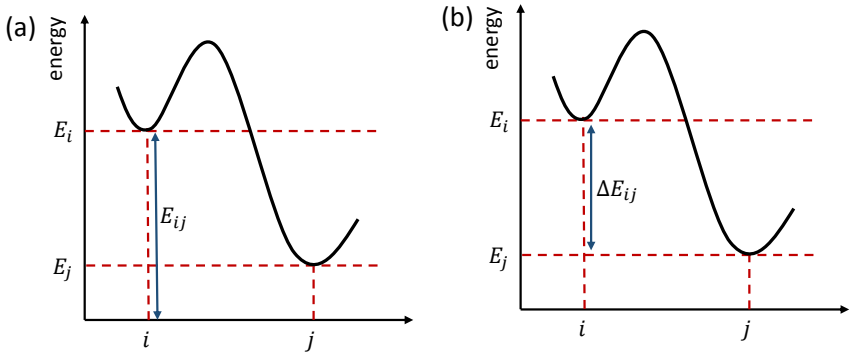

Figure 2.7: Energy barrier for two types of transition rates for the transition from configuration i to configuration j. E_i and E_j are the energy of configuration i and j, respectively. E_{ij} and ΔE_{ij} denote energy barrier of type **(a)** and **(b)**, respectively. For transition rate type **(a)**, $E_{ij} = -E_i$. For transition rate type **(b)**, the energy barrier, ΔE_{ij} is the change of energy for the transition from configuration i to j with $\Delta E_{ij} = E_j - E_i$.

If the Monte Carlo algorithm is employed to an adequately large system to ensure that the events are independent, the Poisson process can be virtually simulated. Then the increment time, Δt, for each transition can be obtained from an exponential distribution [120],

$$\Delta t = -\frac{ln(\rho)}{\sum_j r_{ij}} \,, \tag{2.11}$$

where $\rho \in (0, 1]$ is a uniformly distributed random number and $\sum_j r_{ij}$ is the total rate of all possible transitions for state i.

The KMC simulation for dealloying in this thesis is an independent implementation of the algorithm by the work of Erlebacher [55]. The transition rate type (a) in the bond-breaking model scenario was used in the KMC dealloying simulations. The energy of a atom i is $E_i = n_i E_b$ with n_i the coordination of atom i and E_b the bond energy. For type (b), in the bond-breaking model scenario, adatoms on terrace have the same rate with adatoms on steps because $\Delta n_{ij} = 0$. By contrast, adatoms on terrace ($n_i = 9$) move much fast than adatoms on steps ($n_i = 8$) for type (a) rate. There will be many Au adatoms after Ag atoms removed during dealloying. In this case, transition rate type (a) is better for describing the physical process of dealloying. The simulation result for diffusion with transition rate type (b) is qualitatively comparable with type (a) with temperature and energy scales shifted [55].

For the KMC simulations of coarsening in this thesis, the transition rate type (b) was applied. The coarsening of NPG is a process of reducing surface energy and surface area. For type (a), the target sites of hopping from atom i are treated as equivalent and independent of their coordination, n. By contrast, in type (b), the hopping to target site have various probability which is weighted with their coordination. In this case, the hopping from atom i to its target vacant sites with more reduction of surface energy will have higher probability in the chain. Thus type (b) is more efficiency to simulate the coarsening process of reducing surface energy. As the scale of coarsening simulation box in this thesis is very large, type (b) was chosen for the coarsening scenario.

2.2.2 Dealloying by kinetic Monte Carlo simulation

Based on Erlebacher's detailed description of the KMC algorithm for dealloying [55], an independent implementation was conducted by adopting also the materials parameters from that study. Dealloying signatures obtained from this approach show semi-quantitative agreement with experimental measurements [31, 55, 67, 124]. In this thesis, KMC-dealloying was used for Chapter 3, Section 4.1 and Section 5.1. The initial configuration was described in Section 2.1.5. Simulations were run upon a rectangular on-lattice face-centered cubic (fcc) unit cell with a free surface of [111] for corrosion and periodic boundary conditions applied for the lateral directions. In the KMC dealloying simulations, two kinds of events, namely "*diffusion*" and "*dissolution*" were included.

The diffusion event describes a jump of Au or Ag atom to one of the nearest vacant neighboring sites with the "bond-breaking model". The transition rate type (a) was used. The rate of an atom, which has n first nearest neighboring shell sites, associated with each diffusion event, k_n^{diff}, is

$$k_n^{\mathrm{diff}} = \nu_{\mathrm{D}} \exp \frac{nE_{\mathrm{b}}}{k_{\mathrm{B}}T} \,. \tag{2.12}$$

Here, ν_{D} is the attempt frequency, E_{b} denotes the bond energy, k_{B} and T represents the Boltzmann constant and the temperature, respectively. These parameters are adopted from earlier work [31, 55] with $\nu_{\mathrm{D}} = 10^{13}$ s^{-1} and $E_{\mathrm{b}} = -0.15$ eV. The parameter ν_{D}, taking the order of Debye frequency, can be understood as the thermal vibration frequency of the atom around its equilibrium position [125]. With these parameters used, the length scales and time scales of the simulation are comparable with experiments. The temperature, T, is fixed to 300 K for all simulations.

The dissolution event is restricted to the removal of an Ag atom only. The bond-breaking model is also used to treat dissolution events. An additional parameter, ϕ, is used here to modify the energy barrier of Ag atoms dissolution based on the "dealloying potential" in experiments, which is the charge transfer per dissolved atom, here one elementary charge. Therefore, n-coordinated Ag atoms dissolving at a rate per atom is

$$k_n^{\mathrm{diss}} = \nu_{\mathrm{E}} \exp \frac{nE_{\mathrm{b}} + \phi}{k_{\mathrm{B}}T} \,. \tag{2.13}$$

with $\nu_{\mathrm{E}} = 10^4 \mathrm{s}^{-1}$ the effective attempt frequency. For ϕ, values in the range of 1.00 eV to 1.25 eV were implemented. An interval of 3×10^4 in dealloying time can be obtained from this potential range, which is adequate for our study of dealloying kinetics.

The dissolution was restricted to Ag atoms located on the surface that have at least 3 neighboring vacant sites. Diffusion was allowed only for target vacant sites with at least 3 nearest neighbor atoms. These rules were applied due to the facts that the dissolution of those 10- and 11- coordinated Ag atoms are negligible and the simulated result of "parting limit" agrees well with experimental data [62].

For visualization, OVITO [115]-a free open-source program was used. For the identification and rendering of percolating clusters during primary dealloying, OVITO's "Cluster Analysis" modifier was used with 0.3 nm (just beyond the first neighbor shell) as the cut-off radius.

2.2.3 Coarsening by Kinetic Monte Carlo simulation

In this work, the coarsening was investigated by applying on-lattice KMC simulations [126] with periodic boundary conditions in 3D and running on the open source KMC platform SPPARKS [127]. The software SPPARKS was used for the coarsening simulation because it enables parallel computation and that was required for the computationally extremely demanding coarsening simulations. The simulation boxes for coarsening simulation with edge length $b = 200a$ and $b = 400a$ have 32 and 256 million sites, respectively. This scale of KMC simulation is by far the computationally largest study in the field which has no precedent in the prior literatures. The very large simulation box is to exclude the influence of length of box edge on the length scale of coarsened NPG network. By contrast, the dealloying process can not be implemented in SPPARKS because the dissolution event is not included. Thus KMC dealloying simulations were run on my own code which is not able for parallel computation.

KMC-coarsening was used for Section 4.2 and Section 5.3. The initial microstructures for coarsening simulations have been introduced in Section 2.1.3. NPG microstructures were generated by leveled-wave modulation and mapped to cubic simulation boxes with a rigid fcc lattice. In the simulation box, there are two kinds of sites, the ones occupied with gold atoms and vacant sites. The energy for a vacant site is 0. The energy, $\mathfrak{E}$, of each occupied site was calculated by the nearest-neighbor bond counting model,

$$\mathfrak{E} = n\varepsilon, \tag{2.14}$$

Here, the same $\varepsilon = -0.15$ eV was used here. The value of ε is selected based on the specific surface excess free energy, γ, which drives coarsening. Typically, the γ of densely packed surfaces of metal crystals is around $1\,\mathrm{J/m^2}$. Deriving from the excess energy in the broken bonds per surface area, the values of ε = -0.15 eV and a = 408 pm used here indicate the specific surface energies for terraces of {111}, {100} and {110} are 1.00, 1.16 and $1.23\,\mathrm{J/m^2}$, respectively. Despite being about 10 % lower than predictions by density functional theory (DFT) for gold [128], their ratios are in agreement with DFT results.

At each simulation step, a jump from an atom to one of its nearest neighboring vacant sites will take place. Due to the jump, the total energy will vary, ΔE, for the system,

$$\Delta E = E_{\mathrm{final}} - E_{\mathrm{initial}}, \tag{2.15}$$

where E_{initial} and E_{final} refer to the system energy before and after the jump, respec-

tively. According to Eq. 2.14, ΔE is given by

$$\Delta E = 2\varepsilon\Delta n, \tag{2.16}$$

with Δn the change of coordination number induced by the jump.

By adopting the type (b) transition rate, the rate, r, of each jump event is

$$r = \begin{cases} \nu & \text{if} \quad \Delta E < 0 \\ \nu \exp -\frac{\Delta E}{k_{\mathrm{B}} T} & \text{if} \quad \Delta E \geq 0\,. \end{cases} \tag{2.17}$$

Here ν, k_{B}, and T refer to the attempt frequency, Boltzmann's constant, and the temperature, respectively. The value of ν depends on the details of the atomic-scale diffusion mechanism and can be determined by the Transition State Theory [123]. At $T = 900$ K a value of 10^{12} s^{-1} is typically assumed [127, 129] with which the time scales are comparable with experiments. The simulations were run in parallel with 64 cores (a 3D grid of processors arrayed by $4 \times 4 \times 4$ is mapped to the global simulation box) for each simulation of simulation box edge length $200a$ and 256 cores (arrayed by $8 \times 8 \times 4$) for $400a$ edge length box.

2.2.4 Shrinkage by Molecular Dynamics simulation

The shrinkage (Section 5.2) of NPG was studied by utilizing Molecular dynamics (MD) simulations. The initial configurations of shrinkage simulations used the leveled-wave model to generate the NPG microstructure with φ in the range of 0.20 to 0.35. A cubic simulation box with an edge length of 81.6 nm was used and the generated NPG structures have identical ligament diameter size of $L_{\mathrm{ap}} \approx 3.3$ nm. A detailed description is shown in Section 2.1.3.

The procedure of the MD simulations on NPG microstructures was based on the approach established by Ngô et al. [99]. The open-source package LAMMPS [130] was used for MD simulations. An EAM potential for Au [131] describes the interaction potential. Nóse-Hoover thermostat and barostat [132, 133] were used to control the temperature and pressure. The conjugate gradient algorithm was used for athermal relaxation to minimize energy. After that, a thermal relaxation at 300 K in a state free of load was performed. The time period of this thermal relaxation is 2 ns for shrinkage. All MD simulations were conducted with a time step of 2 fs and periodic boundary conditions were satisfied in all directions during the simulation.

2.3 Analysis of characteristic size

2.3.1 Size of silver clusters and ligaments during dealloying

The approach for the analysis of the characteristic length scale, L, of silver clusters or ligaments during dealloying is based on the radial distribution function (RDF), $\rho(r)$, and the microstructural envelope function, $H(r)$ [134, 135]. Figure 2.8 shows schematic images of functions and the producing procedure of $H(r)$.

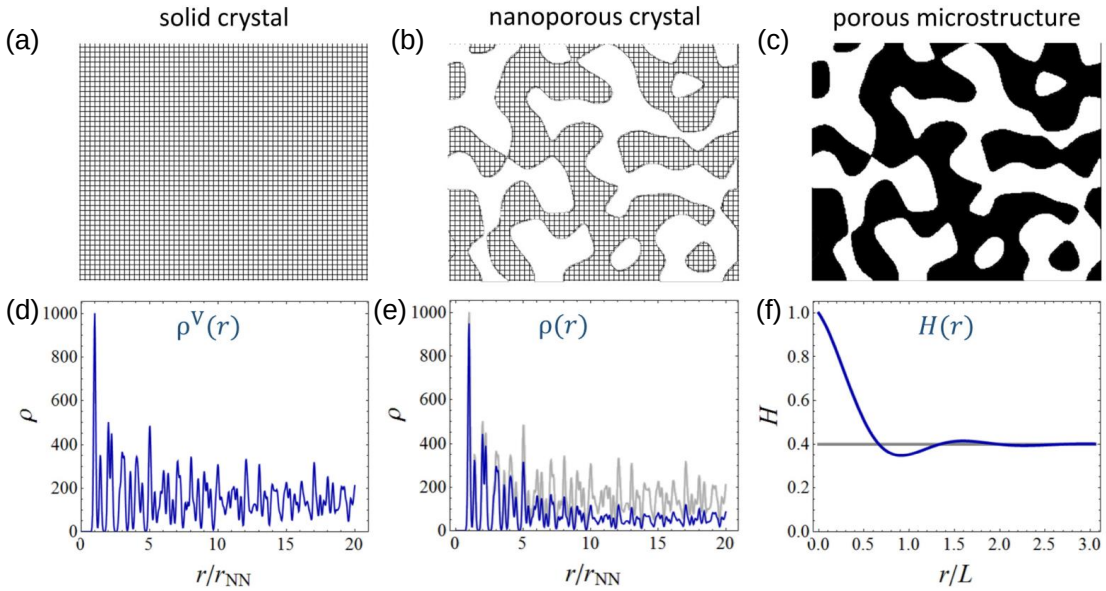

Figure 2.8: Schematic of analysis process of the envelope function, $H(r)$ for NPG structure. (a-c): 2D schematic structure for (a) solid crystal lattice, (b) nanoporous crystal lattice and (c) geometry of nanoporous microstructure. (d, e): Radial distribution function (RDF) of solid crystal, $\rho^V(r)$, (d) and nanoporous crystal, $\rho(r)$, (e). (f) is the envelope function, $H(r)$. Reprinted with permission from Ref [134].

RDF for the solid crystal (no pore phase) (Figure 2.8a), $\rho^V(r)$, is the spherical average number density of atoms with the distance r to a reference atom [136],

$$\rho^V(r) = \frac{n^V(r)}{\Delta V}, \tag{2.18}$$

where $n^V(r)$ is the total amount of atoms located in the volume shell between $r - 0.5\Delta r$ to $r + 0.5\Delta r$ and Δr is a suitable bin size for the histogram. With the volume of the shell, $\Delta V = 4\pi r^2 \Delta r$, and after normalized by the total number of atoms, N,

$$\rho^V(r) = \frac{n^V(r)}{N 4\pi r^2 \Delta r}. \tag{2.19}$$

Then, $\rho^V(r)$ represents an effective density of neigbhoring atoms which have the distance of r to the reference atom.

As compared to a solid crystal which has no pore phase, a nanoporous crystal (Figure 2.8b) can be generated by removing atoms from it. The only effect of this procedure is the reduction of the number of neighbors in the volume shell, while there

is no displacement of atom positions. As a result of the pore phase formation, the height of RDF decreases, but the peak positions remain unchanged (Figures 2.8d and e). The RDF of a nanoporous crystal, $\rho(r)$, is

$$\rho(r) = \frac{n(r)}{N_{\text{solid}} 4\pi r^2 \Delta r}, \tag{2.20}$$

with N_{solid} the total number of atoms in nanoporous crystal.

This loss of height can be evaluated by the envelope function [134], $H(r)$,

$$\rho(r) = \rho^{\text{V}}(r) H(r)\,. \tag{2.21}$$

According to Eqs 2.19, 2.20 and 2.21,

$$H(r) = \frac{1}{\varphi} \frac{n(r)}{n^{\text{V}}(r)}\,, \tag{2.22}$$

where $\varphi = N_{\text{solid}}/N$ denotes the solid fraction of the nanoporous structure. Essentially, $H(0) = 1$ and $H(r)$ tends to converge to φ at r much larger than the size of pores or ligaments in the nanoporous structure (Figure 2.8f).

The microstructure size, L, is inversely proportional to the initial slope of $H(r)$ by [135, 137],

$$L^{-1} = -\left.\frac{\mathrm{d}H}{\mathrm{d}r}\right|_{r=0}. \tag{2.23}$$

Here ligaments are approximated as long circular rods.

Therefore, the mean ligament size of the entire solid phase (including Au and Ag) was determined by analyzing its envelope function, $H_{\text{total}}(r)$. Moreover, to evaluate the mean size of silver clusters, the envelope function of Ag-Ag, $H_{\text{Ag–Ag}}(r)$, was calculated by using the Ag component only. Periodic boundary conditions were applied for lateral directions when calculating $H(r)$.

2.3.2 Ligament size during coarsening

The coarsening process reduces the surface energy, which is the product of the specific surface excess free energy, γ, with surface area, A. Therefore, the surface area per solid volume (V_{S}), $S_{\text{V}} = A/V_{\text{S}}$, is a natural microstructural parameter in coarsening studies at preserved volume [138, 139]. Similarly, this parameter is commonly estimated in NPG experiments as well [91, 140, 141]. S_{V} was calculated from A and V_{S} which are evaluated by the surface reconstruction algorithm of Ref [142]. In this algorithm, the atomic structure of the solid is tessellated using a Delaunay method. As a result of the tessellation, the algorithm is able to extract the location of a surface by convolution with a spherical probe volume [142]. The radius of the probe was fixed to 0.3 nm. To determine the growth law during coarsening, for the calculation of S_{V} of KMC-coarsened NPG structures, A and V_{S} were analyzed only for the largest contiguous cluster of the NPG network with other isolated clusters removed.

As defined in Section 2.1.2, the apparent ligament size, L_{ap}, the mean diameter of ligaments is calculated via,

$$L_{\mathrm{ap}} = \frac{4}{S_{\mathrm{V}}}\,. \tag{2.24}$$

Here, the prefactor 4 arises from the approximation of the ligaments in the NPG structure to the long circular rods, i.e. for a circular rod with L as its diameter, the relation between L and S_{V} is $L = 4/S_{\mathrm{V}}$.

According to Ref [32], S_{V} is directly related to a different measure of ligament size, namely the characteristic spacing between neighboring ligament centers, $\tilde{L}$:

$$\tilde{L} = \alpha\lambda = \frac{4}{S_{\mathrm{V}}}\,\frac{\alpha}{\sqrt{3}\varphi}e^{-[\mathrm{erf}^{-1}(2\varphi-1)]^2}\,. \tag{2.25}$$

Here $\alpha = 1.23$ and $\lambda = 2\pi/q$ denotes the wavelength of the Gaussian field. Equation 2.25 is defined for the initial microstructure generated by the leveled-wave model; it also applies to coarsened structures if the coarsening process leads to a self-similar microstructure evolution.

For those leveled-wave model generated structures listed in Tables 2.1– 2.3, leveled random fields define the specific surface areas of these initial microstructures precisely according to Eqs 7 and 13 in Ref [32] of the main text,

$$S_{\mathrm{V}} = \frac{q}{\varphi}\,\frac{2}{\pi\sqrt{3}}\,e^{-[\mathrm{erf}^{-1}(2\varphi-1)]^2}\,. \tag{2.26}$$

Here, Eq 2.2 drives the characteristic wave number q from the H values and φ is the solid fraction.

The L_{ap} is then can be evaluated by Eq 2.24 from S_{V}. The $\tilde{L}$ can be calculated from the q_0 by Eq 8 in Ref [32],

$$\tilde{L} = 1.23\lambda = 1.23\frac{2\pi}{q_0} = 1.23\frac{b}{H} \tag{2.27}$$

Eq 2.26 is only valid for initial structures generated by the leveled-wave model, by contrast, for KMC coarsened structures, S_{V} was resolved by the surface reconstruction algorithm of Ref [142] and L_{ap}, $\tilde{L}$ were determined via Eqs 2.24 and 2.25, respectively.

2.4 Connectivity: Genus and scaled genus

2.4.1 Genus

The topological microstructural parameter connectivity is characterized by the scaled genus, g, of the network. The definition of g refers to Section 2.4.2. The genus, G, provides the basis of g. In a network microstructure, G can be specified by the number of connections [20, 22, 66, 87]. More descriptively, G designates the maximum number of cuts that can be done to the network before it splits into two independent parts and collapses. A straightforward way to get G is by counting the handles or holes of the structure. For example, solid structures of a sphere, a donut, and a pretzel have G values of 0, 1, and 3, respectively.

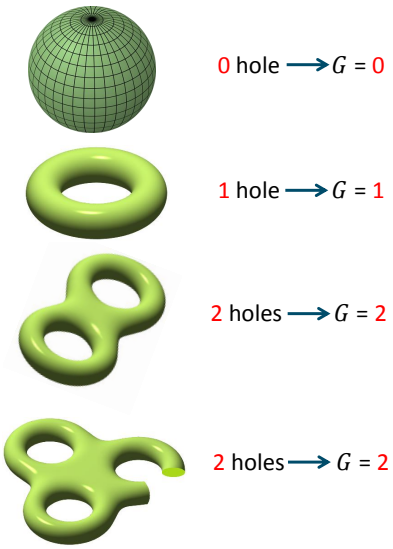

Figure 2.9: Genus-the number of connections by counting handles or holes of the structure. Examples of G values for different structures were shown. The bottom image shows a cutting on a pretzel and G of that reduced from 3 to 2. Reprinted with permission from Ref [143].

Numerical computation of G can be achieved based on the rule that $G = B_1/2$ for a surface with B_1 the first Betti number. Betti number, another topological term, reveals the homology group of a structure. The first three Betti numbers are, B_0-the number of connected components, B_1-the number of tunnels, B_2-the number of cavities [144, 145].

An indirect approach to compute B_1 is evaluating the Euler characteristic, χ, with

$$\chi = B_0 - B_1 + B_2. \tag{2.28}$$

For a closed surface, $B_0 = B_2 = 1$. Therefore, $\chi = 2 - B_1 = 2 - 2G$, indicating,

$$G = 1 - \frac{\chi}{2}. \tag{2.29}$$

The Euler characteristic, χ, can be calculated by triangulating the surface of the structure [146] and via

$$\chi = v - e + f. \tag{2.30}$$

with v, e, and f the number of vertices, edges, and triangles of the triangulated surface. The surface mesh of the triangulation is required for this approach.

The Betti numbers can also be calculated in a direct manner based on the homology theory [147]. In this thesis, the Betti numbers of KMC-generated microstructures were computed by the open source CHomP homology software [148]. Its option for periodic boundary conditions was switched on for periodic microstructures in order to avoid the effects of boundary on the topology calculation. According to the aforementioned definition, $B_0 = 1$ implies that the solid network is a single connected cluster, while larger B_0 indicates that there are isolated particles formed. The genus was determined by $G = B_1$ since the input data were solid structures.

The input data of CHmoP requires on-lattice structures. So, it can be inputted straightforward for structures generated by KMC due to they are on-lattice structures. By contrast, the MD generates off-lattice structures. Prior to CHmoP, sites of all MD-generated off-lattice structures were shifted to their nearest neighboring on-lattice sites with the same simulation box size, and all voids in the solid phase were removed.

2.4.2 Scaled genus-connectivity

G is an extensive property. G scales with the volume of the specific microstructure for a material. In light of the fact that the ligament size of the NPG microstructure increases during coarsening, it is preferable to utilize a connectivity measurement that is independent both of the volume of the sample and the length scale of the microstructure. For this purpose, a scaled genus, g, was employed by using the ligament size, L_{ligament},

$$g = G\frac{L_{\text{ligament}}^3}{V_{\text{total}}}. \tag{2.31}$$

where V_{total} is the total sample volume, including solid and pore phases. In this work, for the dealloying simulations generated structures, the ligament size, L, analyzed via the envelope function, was used to represent L_{ligament} for the evolution of connectivity during dealloying. For coarsening or shrinkage simulations produced structures, the ligament spacing, $\tilde{L}$, based on the surface reconstruction, was used to represent L_{ligament} for the evolution of connectivity during coarsening. According to its definition, g represents the number of connections in a representative volume element of size, L_{ligament}^3.

2.5 Selection of analysis methods

In this thesis, the processes of dealloying, coarsening and volume shrinkage of NPG microstructure were studied by using KMC or MD simulations. The evolution of length scales (Chapter 4) and connectivity (Chapter 5) were discussed. Various analysis method for length scales and connectivity have to be chosen depending on the different processes studied and the questions focused on. In this section, the selection of analysis methods will be introduced.

For length scale:

In Section 4.1, for the structures produced by the KMC dealloying simulations, the silver clusters are embed in the ligaments and maintain the composition of the parent alloy. So it is difficult to define the boundaries of the silver clusters. Therefore, in this case, the analysis of surface area cannot be done using the surface reconstruction method. In order to give a more accurate analysis of the characteristic length scale, L, for dealloying simulations produced structures, the envelope function was used. In a microstructure, the envelope function, H, of a phase, examines the average, over all material points in that phase, of the fraction of the phase that is confined within a spherical shell with radius r surrounding a material point. Refer to Section 2.3.1 for detailed description.

In Section 4.2, coarsening derives from the strife to reduce the specific surface area, S_{V}. In the context of coarsening at conserved volume, S_{V}, is a natural microstructural parameter. In experiment studies on NPG, this parameter is also commonly estimated [91, 140, 141]. In order to discuss the coarsening law, during coarsening, the evolution of two characteristic length scales, L_{ap} and $\tilde{L}$ were explored. In Section 4.2, for coarsening simulations generated structures, L_{ap} and $\tilde{L}$ were calculated based on S_{V}. S_{V} was obtained from the surface reconstruction method. See Section 2.3.2 for detailed information.

For connectivity:

In Section 5.1, the question "What connectivity is generated during dealloying" was discussed. The ligament size, L, of dealloying simulation generated structures in Section 4.1 was analyzed via the envelope function. Therefore, g for dealloying simulated NPG microstructures is given by

$$g = G\frac{L^3}{V_{\mathrm{total}}}. \tag{2.32}$$

with L the ligament size of dealloying simulated structures.

In Section 5.2, the ligament spacing, $\tilde{L}$, was used to scale the genus of structures outputted from shrinkage simulations. For the initial structure, $\tilde{L}$ [32] is

$$\tilde{L} = 1.23\frac{2\pi}{q_0} = \alpha\frac{b}{H} \tag{2.33}$$

here, H is the constant magnitude of waves (Eq 2.3) and b is the simulation box edge length.

Note that $\tilde{L}^3/V$ remains invariant when the simulation undergoes an essentially affine contraction during relaxation. This implies that the relative changes in g and in

G coincide. When $\tilde{L}$ is used to represent the length scale, with Eq 2.33 and Eq 2.31, the scaled genus in any state, initial as well as relaxed, is

$$g = G\left(\frac{1.23}{H}\right)^3. \tag{2.34}$$

In Section 5.3, $\tilde{L}$ was employed to scale the genus of coarsened NPG microstrutures. The findings in Section 4.2 emphasized that the ligament spacing, $\tilde{L}$, is more intrinsically associated with the coarsening kinetics than the ligament diameter, L_{ap}, with regard to the microstructure evolution by surface transport. With L_{ligament} represented by $\tilde{L}$ in Eq 2.31, the scaled genus of coarsened NPG microstrutures, is

$$g = G\frac{\tilde{L}^3}{V_{\mathrm{total}}}. \tag{2.35}$$

Chapter 3

Residual Ag and its evolution during dealloying

In this Chapter, the evolution of residual less noble element (Ag in the Ag-Au dealloying scenario) content, including the composition and distribution, during NPG dealloying will be discussed. KMC-dealloying was carried out to study the dealloying process of NPG. A rectangular box bounded by {111}-, {110}- and {112}-type faces was randomly filled with 75% atomic fraction Ag atoms and 25% Au atoms (see Section 2.1.5). The (111)-oriented surface is free from corrosion, and in the lateral directions, periodic boundary conditions apply. Dealloying simulation at potential, ϕ, various from 1.00 eV to 1.25 eV were studied. The simulation method of KMC-dealloying is described in more detail in Section 2.2.2. The dissolution flux density will be discussed first, since this is routinely recorded in experimental studies and so the validity of the dealloying approach can be assessed by looking into dissolution flux density.

3.1 Dissolution flux density

The evolution of dissolution flux density, j, during the dealloying was monitored. In accordance with Ref.[55], j is defined as the number of dissolved Ag atoms per one site of the original {111} surface of master alloy in one unit of time. Note that with this definition, j has the unit of number/site/second and, upon choosing a reference potential, corresponds to the dissolution current density usually used in electrochemical dealloying experiments.

Figure 3.1a shows the evolution of j versus the dealloying time, t, for $\phi = 1.15$ eV. Similar to the prior study [55], where the same set of parameters were used, there are three apparent stages in the course of j. Dealloying begins–stage A–when the first few layers of the surface starts to dissolve. At stage A, there is nucleation of Au atoms islands by diffusion and passivation. The two waves at stage A represent the dissolution of the first two layers. The overall high j at stage A is because of the more exposed Ag atoms of the first few layers and the decrease of j is due to the passivation of Au atoms diffusion. The following–stage B (the plateau in the figure)–characterized by an essentially constant j illustrates that a steady-state dissolution front penetrates through the sample. j drops sharply at the end of stage B which indicates the dissolution front has swept the entire sample. Then j exhibits continuously decrease–stage C. The

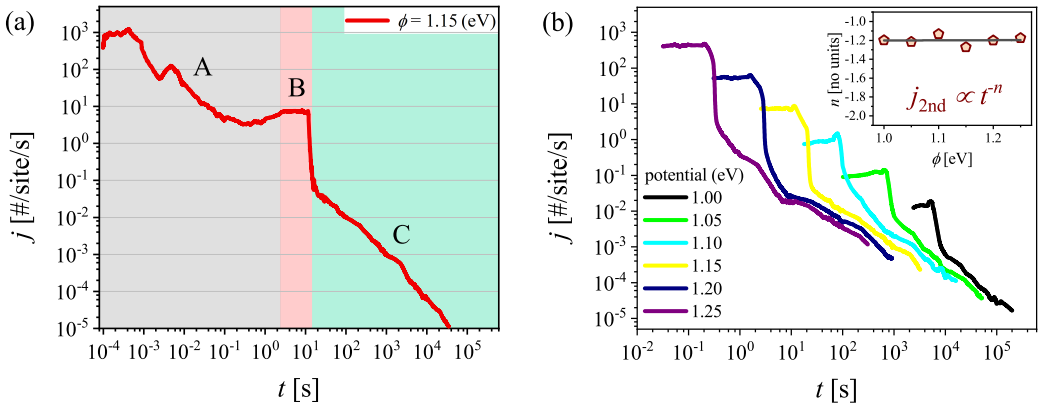

Figure 3.1: Evolution of dealloying rate, represented by the dissolution flux density, during dealloying at different potentials, ϕ. (a) Flow densities, j, versus dealloying time, t, for ϕ = 1.15 eV. Colored background regions represent the different dealloying stages: (A) dealloying of the initial few surface layers with surface roughening and passivation, (B) steady-state dealloying with corrosion front penetrating the entire simulation box, (C) dealloying and coarsening of the ligaments in the nanoporous network established in B. (b) similar graph with (a) of $j(t)$ for different ϕ but only stages B and C are displayed. Inset: exponent n in the power law $j \propto t^n$ for various ϕ at stage C. Note the horizontal fitting line in the inset figure indicates n is independent of ϕ and has a mean value $n = 1.20 \pm 0.07$. All axes in figures (a) and (b) are logarithmically displayed.

logarithmic time axis allows the figure to display phenomena on extremely different timescales. By inspection of the Figure 3.1a one can then see that the process for stage A is very fast but has the longest time duration for stage C.

Figure 3.1b illustrates similar graphs of Figure 3.1a with j as a function of t, but results for different dealloying potentials, ϕ. For clarity, stage A is excluded and only stages B and C are shown in Figure 3.1b. The same two well-defined separated stages are observed for all potentials. At the steady-state stage, j decreases and time duration increases with decreasing ϕ. It is shown that all potentials exhibit the same general phenomenology, especially the two well-separated stages. This observation can be further illustrated by fitting of the $j(t)$ curves for different ϕ. After extraction of the data for stage C, fittings for the data at different ϕ of j as a function of t show a power scaling law:

$$j_{2\text{nd}} \propto t^{-n}, \tag{3.1}$$

with the exponent $n = 1.20 \pm 0.07$ which is independent of ϕ. Here subscript 2nd of $j_{2\text{nd}}$ denotes the secondary dealloying stage which corresponds to stage C in $j(t)$ graph and will be described in the subsequent section.

3.2 Residual Ag and two steps of dealloying

The previous section explored that there are two main well-defined separated stages with distinguish j during dealloying. The various value of j reveals the different dissolution velocity of Ag atoms, implying the different evolution of residual Ag in that

two stages. The linear-log plots in Figure 3.2a show the respective changes of Ag atom fraction, x_{Ag}, during the dealloying as a function of t for different potentials ϕ. In congruence with the steady-state stage B in graphs of $j(t)$ (Figure 3.1), all simulated curves show an initial sharp drop of x_{Ag}. In this stage, the dissolution of Ag from the master alloy has an essentially constant rate as the corrosion front moves to the depth of the sample. Then the $x_{\mathrm{Ag}}(t)$ graphs exhibit a discontinuous change in slope. The transition points (open circles in Figure 3.2a) correspond to the severe drop of j in Figure 3.1b indicating the corrosion front has been swept over the entire sample and all master alloy has been consumed. The later process links to the dealloying of the ligaments of 3D bicontinuous networks. Irrespective of the applied potential, the dealloying process with an initially high rate of Ag reduction becomes orders of magnitude slower after a critical point. Taking $\phi = 1.15\,\mathrm{eV}$ as an example: while it only takes ~14 s for the Ag content to decrease from 0.75 to ~0.18 (b to d in Figure 3.2a), another period of more than $2.5 \times 10^4\,\mathrm{s}$ is needed to dissolve the remaining Ag (d to e in Figure 3.2a).

These transition points (open circles in Figure 3.2a) associated with the sharp drop in j mark the instant when the corrosion front has completely crossed the entire sample. This phenomenon has been observed for all ϕ. In line with Ref [29], the process before and after the transition points was defined as *primary* dealloying stage and *secondary* dealloying respectively.

Taking ϕ=1.15 eV as an example, the evolution of the microstructures during dealloying are rendered and displayed in Figures 3.2 b-e. Stage B exhibits a fast dissolution which corresponds to the steady-state dealloying stage. During stage B, the corrosion front propagates to the bottom of simulation box (Figures 3.2 b-c). While stage C shows a slow dissolution process. At stage C, the dissolution occurs along with the coarsening of ligaments (Figures 3.2 c-e).

A careful examination suggests a fundamental difference between the microstructure of simulated Au-Ag systems in the primary and secondary dealloying stages: During the primary dealloying: (i) the onset of dealloying exhibits the dissolution of the few surface layers associated with the roughening and passivation of surface (Figure 3.2b). (ii) then the simulated Au-Ag systems consist of a homogeneous undealloyed remnant of the master alloy and a network system attaching to it (Figure 3.2c). The microstructure of the primary dealloyed sample, which was obtained right after the primary dealloying stage, resembles three-dimensional, uniform, bicontinuous networks of nanoscale ligaments (Figure 3.2d). The secondary dealloying, while continuing to remove residual Ag atoms inside the ligaments, coarsens the ligaments but maintains the underlying network structure (Figure 3.2e).

With the conception of primary and secondary dealloying established, the current simulated data yield several important observations concerning the difference of j and x_{Ag} between these two dealloying steps. First, as shown in Figure 3.1, a constant dealloying rate implies that the corrosion front moves at a constant velocity during primary dealloying. Secondary dealloying, on the other hand, exhibits a power law behavior in which j decays with time for $j_{\mathrm{2nd}} \propto t^{-n}$ and n is independent of ϕ. Second, the inset figure in Figure 3.2a shows that the primary dealloyed samples contain a relatively high Ag fraction and a higher ϕ results in a decrease in residual Ag fraction. The x_{Ag} of the primary dealloyed samples, for example, decreases from 0.35 to 0.10

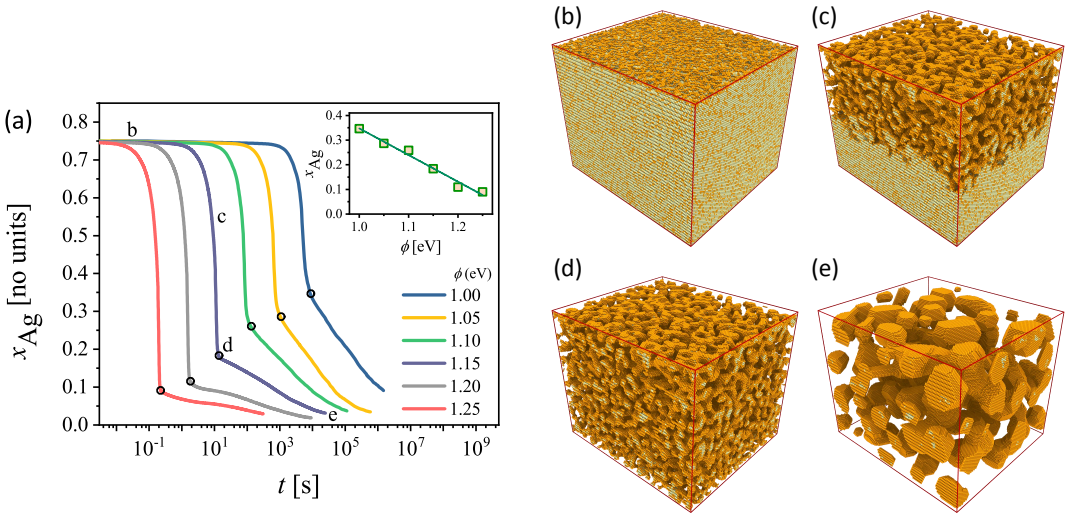

Figure 3.2: Evolution of Ag fraction and microstructure during dealloying. (a) Linear-log graph of Ag fraction, x_{Ag}, as a function of dealloying time, t, during dealloying at different ϕ. Note the two well-separated steps for $x_{\mathrm{Ag}}(t)$: the first significant fast drop in x_{Ag} step and the slow down x_{Ag} decreasing step. The transition point (open circles) for the slope of $x_{\mathrm{Ag}}(t)$ marks the end of the primary dealloying stage and the onset of the secondary dealloying stage. Inset shows x_{Ag} of primary dealloyed samples, which were taken immediately after the primary stage and before the onset of the secondary stage, as a function of ϕ. In (b-d), at $\phi = 1.15$ eV, microstructure at different dealloying time steps is rendered, as indicated by the markers on the respective graph in (a). The randomly distributed Ag and Au atoms in the master alloy and the rough structure in the first few layers after the dissolution in (b) illustrates the surface roughening and nucleation of Au atoms islands. A debuting ligament network can be seen in the partially dealloyed sample (c). This 3D bicontinuous network completes its establishing at the transition point (d). Further dealloying coarsens the ligaments, yet maintains the network structures (e).

when ϕ increases from 1.00 eV to 1.25 eV. However, the graphs of $x_{\mathrm{Ag}}(t)$ decay to near 0 for all ϕ, indicating the secondary dealloying will remove almost all the remaining Ag.

3.3 Composition profile and morphology

Next, the composition profile of the partially dealloyed structure during primary dealloying is investigated. Figure 3.3 displays the rendering of a snapshot for the microstructure of a partially dealloyed structure (top) and clusters of Ag atoms in the same partially dealloyed structure (center) in a subvolume of the sample, associated with the corresponding Ag composition profile of the sample versus each layer (bottom). At the center, all the gold atoms have been removed, and a cluster analysis has been performed to identify individual and isolated silver clusters. Each of those silver clusters has been assigned a distinct color. For explanation of the cluster analysis see Section 2.2.2. It is evident that the corrosion front has a transition region of finite thickness that separates the virgin alloy and the primary dealloyed NPG. During the corrosion front moving to virgin alloy, the silver clusters transit from the single per-

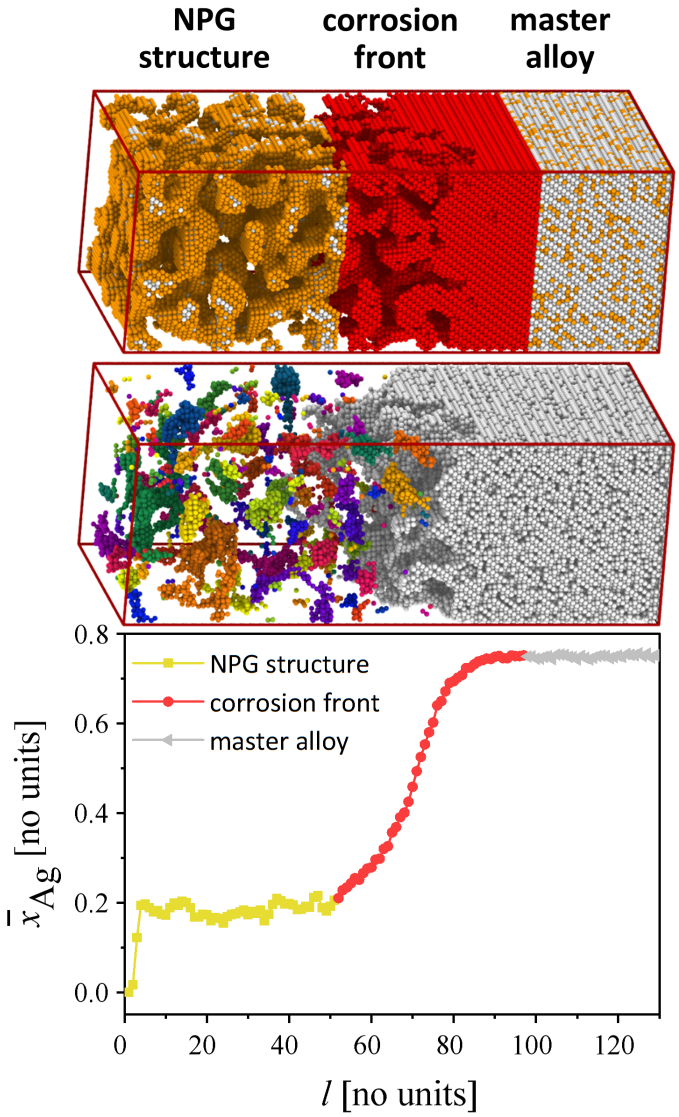

Figure 3.3: Composition profile of partially dealloyed structure during primary dealloying. A partially dealloyed structure (top) with the rendering of Au-Ag atoms at potential, ϕ = 1.15 eV and time, t=7.4 s shows three regions: Dealloyed nanoscale network (left), corrosion front (middle), and undealloyed virgin alloy (right). The color of the Au atoms is golden, and of the Ag atoms is gray. Rendering of silver clusters (center) shows consecutive Ag cluster in master alloy segregate to isolated Ag clusters in the dealloyed ligaments network. The unique color is rendered for distinguishing each contiguous Ag cluster. Graph (bottom) of the corresponding Ag fraction, $\bar{x}_{Ag}$, of each layer l shows sensibly identical Ag fraction in each layer in the primary dealloyed part. $\bar{x}_{Ag}$ of each layer increases gradually in the corrosion front to reach the composition of undealloyed master alloy. For clarity, only a subvolume of 1/3 of the corner of the sample from left to right in the corrosion direction is shown.

colating cluster (gray) of the virgin alloy to isolated clusters of Ag (colored). These isolated clusters of Ag take similar shapes to the ligaments and are homogeneously distributed in the ligaments network region. The graph of the composition profile, at the bottom of the figure, is analyzed by calculating the average Ag fraction, $\bar{x}_{Ag}$, of the plane perpendicular to the corrosion direction for each layer in the entire sample versus

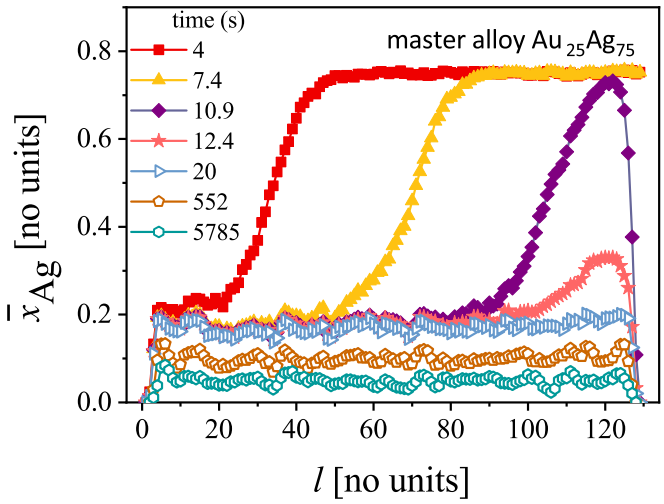

Figure 3.4: Composition profiles during primary (closed symbols) and secondary (open symbols) dealloying stages. Sensibly constant values over time of x_{Ag} in the primary dealloyed region implicate the secondary dealloying behind the corrosion front is negligible. Abscissa axis gives layer number. Dealloying potential $\phi = 1.15$ eV.

the layer, l, with l= 1 .. 129. Here l = 1 refers to the external surface layer. Each layer in the NPG structure region displays a sensibly identical Ag fraction with $\bar{x}_{\mathrm{Ag}} \approx 0.18$. As can be seen in the inset of Figure 3.2a, that value of Ag fraction $\bar{x}_{\mathrm{Ag}} \approx 0.18$ corresponds to the residual Ag fraction in the primary alloyed structure. For the corrosion front region (with the thickness of 45 layers and 10.5 nm), $\bar{x}_{\mathrm{Ag}}$ gradually increases from 0.18, $\bar{x}_{\mathrm{Ag}}$ of NPG structure region to 0.75, $\bar{x}_{\mathrm{Ag}}$ of the virgin master alloy. The gradual increase of $\bar{x}_{\mathrm{Ag}}$ is quite likely not the signature of a composition gradient in the solid part of the alloy, but rather the consequence of convolving the essentially constant composition of the corroded alloy with the rough morphology of the corrosion front.

Figure 3.4 plots the composition profile with the same analysis method used in Figure 3.3 for samples in the dealloying process at different times. The sensibly constant composition in primary dealloyed NPG structure is observed for all samples during primary dealloying stage (4 s to 10.9 s). The corrosion front region moves to the depth layer as the dealloying proceeds. $\bar{x}_{\mathrm{Ag}}$ of the primary dealloyed sample (t =20 s) shows homogeneous profile of the Ag through the depth. As dealloying time progresses, at the much longer times which represent the secondary dealloying stage the composition profile, $\bar{x}_{\mathrm{Ag}}(l)$ (open symbols in figure) exhibits a slow and uniform drop.

The observed progression of the composition profile suggests that in the primary dealloying stage the dissolution of Ag behind the corrosion front appears to be negligible. This is simply because of the much lower dealloying rate, j of the secondary dealloying. Primary dealloying happens within a very short time period but the secondary dealloying stage takes a much longer duration. Based on that difference in timescales, two dealloying stages can be analyzed and discussed separately. Hence, in the analysis in Section 4.1, the evaluation of Ag cluster size and ligament size of a partially dealloyed sample in the primary stage was done on the NPG structure part, while such evaluations will be conducted on the entire structure at the secondary stage.

Figure 3.5 shows slices of a NPG structure during primary and secondary dealloying

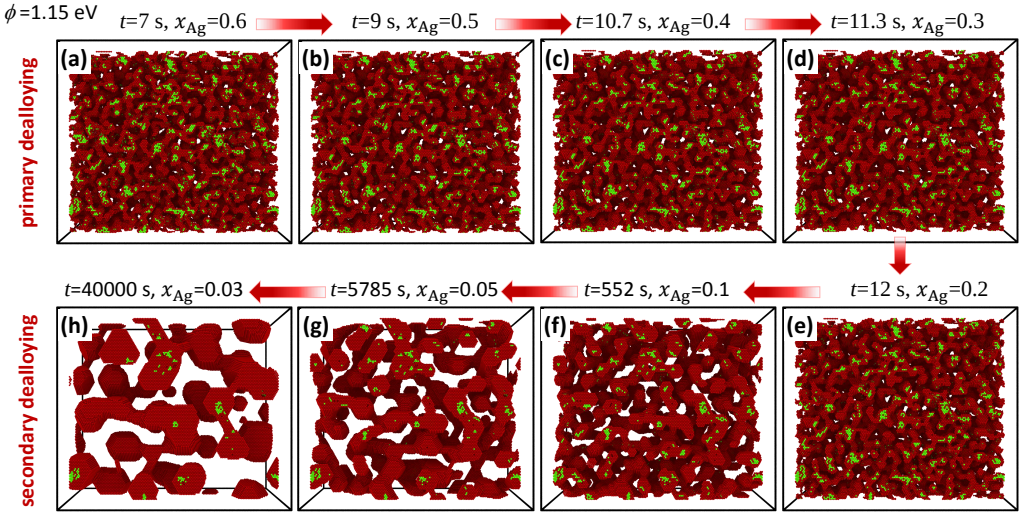

Figure 3.5: Renderings of slices cutting through NPG structures at different t during dealloying at ϕ = 1.15 eV. A red and green color is assigned to the Au and Ag atoms, respectively. (a-d) Discrete Ag clusters are formed during primary dealloying. No changes in ligament size and mean cluster size are visually apparent. (e-h) Ag clusters are gradually dispersed through secondary dealloying and ligaments are coarsened. It appears that silver clusters size does not change and no redistribution of Ag atoms has been observed.

at $\phi = 1.15\,\text{eV}$, exemplifying that Ag atoms (green) are distributed in silver cluster surrounded by Au atoms layers (red). No substantial change on the size and quantity is observed in the primary dealloying stage while the Ag fraction has been reduced from 0.75 to 0.3 in this stage (Figures 3.5a-d). The ligaments at this stage also show no obvious coarsening.

By contrast, during the secondary dealloying stage, as shown in Figures 3.5e-h, many Ag clusters disappeared along with the ligament size growing while the silver fraction only reduces from 0.20 to 0.03. Apparently, some silver clusters are shown in all of those snapshots and their sizes show no change as dealloying proceeds. It is seen that the Ag clusters are buried in the ligaments which are passivated by a mono-layer of pure Au atoms on the surface. Therefore, Ag clusters have a smaller characteristic size than ligaments because of their spatial distribution. A quantitative analysis of L_{Ag} and L_{lig} will be presented in Section 4.1. The evolution of both sizes during dealloying and the relation between these two sizes will be revealed.

3.4 Discussion

Two-stage characteristic of dealloying

Our simulations reinforce that the dealloying process incorporates two evidently distinct stages, i.e. primary and secondary dealloying. During the primary stage, a 3D network is formed while most of the less noble atoms are dissolved. As a result of that process, the ligament network's initial topology is established, as well as the lower limits of the ligament size that can be reached by dealloying. The secondary dealloying describes a step where the network structure is coarsened as a result of

surface diffusion. As the microstructure evolves, the less noble atoms, which were retained after the primary dealloying process, gradually dissolve. This is because they are exposed at the surfaces during the evolution of the microstructure. When it comes to experiments, the two stages usually occur *simultaneously*: A primary dealloying front moves into the depth, while a secondary dealloying follows behind it in its wake.

At any given moment in time, primary and secondary dealloying will occur simultaneously in separate regions of a macroscopic sample in corrosion experiments. By contrast, since our sample size is extremely small, the two processes are essentially separated on the basis of the time axis in our study. It is significant to note that the corrosion front sweeps through the simulation volume very quickly during primary dealloying, and secondary dealloying becomes apparent much later. Consequently, primary and secondary dealloying can be analyzed separately and discussed in this thesis.

Chapter 4

Length scale evolution of nanoporous network

This Chapter will concentrate on the evolution of the characteristic length scale during dealloying (Section 4.1) and coarsening (Section 4.2) of NPG microstructures.

4.1 Ag cluster size and ligament size evolution during dealloying

In Chapter 3, KMC dealloying simulations demonstrate that there are two stages for the dealloying: i) the primary dealloying, in which the initial network of nanoscale ligaments is established and the silver clusters are embedded in ligaments; ii) the secondary dealloying, in which the number of silver clusters decreases as ligaments coarsen. In Section 4.1.1, the size of silver cluster and ligament of the structures generated by dealloying simulations in Chapter 3 will be analyzed via the envelope functions (see Section 2.3.1 for detailed information of the analysis method). In Section 4.1.2, based on the calculated results, the evolution of silver cluster size and ligament size during primary and secondary dealloying will be discussed. Then, the relation between two sizes will be revealed, and the parameters determining the ligament size during dealloying will also be discussed in Section 4.1.2.

4.1.1 Silver cluster size and ligament size

For the dealloying simulations produced NPG structures, the envelope function (see Section 2.3.1) was used for the analysis of silver cluster size and ligament size. Figures 4.1a,b plot the envelope functions of Ag atoms only, $H_{\mathrm{Ag-Ag}}(r)$, and for all atoms, $H_{\mathrm{total}}(r)$, for simulated dealloying structure with $\phi = 1.15$ eV at different dealloying time. The main observation from this figure is the difference of initial slope between $H_{\mathrm{Ag-Ag}}(r)$ and $H_{\mathrm{total}}(r)$. As detailed described in Section 2.3.1, the initial slope of the envelope function can be used to estimate the size of the microstructural feature under investigation. An identical initial slope, which does not depend on the time, can be seen in graphs of $H_{\mathrm{Ag-Ag}}(r)$, implying the invariant Ag cluster size during the entire dealloying process. By contrast, the initial slope of $H_{\mathrm{total}}(r)$ decreases for structures

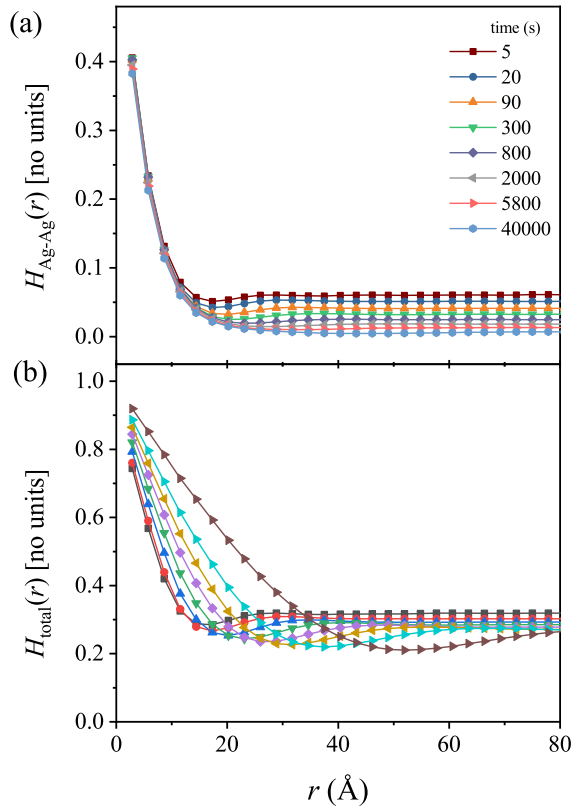

Figure 4.1: Analysis of size during dealloying. The overpotential is $\phi = 1.15$ eV. (a) Ag-Ag envelope function, $H_{\text{Ag-Ag}}(r)$, at different times shows an identical initial slope, suggesting invariant mean cluster size. (b) $H_{\text{total}}(r)$ for the whole system only exhibits increases in the initial slopes in the secondary dealloying stage (time > 20 s). In order to construct $H(r)$ in Figures a-b, a bin size of 2.885 Å was used.

at times, t >20 s which indicates an increase in ligament size after that time.

The above observations are further illustrated by the plots of evolution of Ag cluster size and ligament size. The corresponding results for characteristic ligament size and Ag cluster size, evaluated by Eq 2.23 from the initial slope of Figures 4.1a,b, as a function of dealloying time, t, are shown in Figure 4.2, along with x_{Ag} at the respective time.

The data in Figure 4.2 yields two notable observations:

First, during primary dealloying stage, despite a significant reduction of x_{Ag} from 0.75 to 0.18, both L_{Ag} and L_{lig} remain constant with values of L_{Ag} =0.94 nm and L_{lig} =1.23 nm, respectively.

Second, as soon as the dealloying enters the secondary stage, L_{lig} starts increasing. L_{lig} keeps growing throughout this stage to attain a size which is more than 3 times larger, $L_{\text{lig}} \approx 4$ nm, at the end. At the same time, the remaining Ag is further removed, so x_{Ag} decreases from 0.18 to 0.03. L_{Ag}, surprisingly, stays invariant with the value of $L_{\text{Ag}} \approx 0.94$ nm during the secondary dealloying stage.

It is important to note that the above findings regarding the evolution of the size of Ag clusters and ligaments usually hold to all dealloying potentials, ϕ, investigated here.

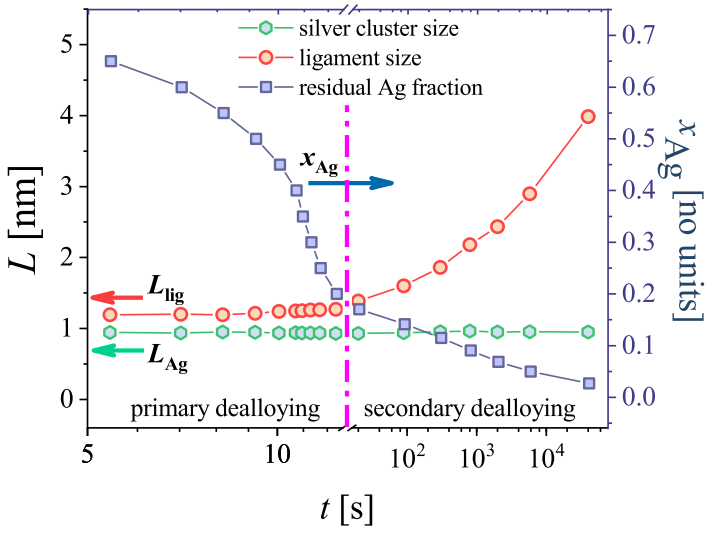

Figure 4.2: Quantitative analysis confirms that both mean Ag cluster size, L_{Ag}, and ligament size, L_{lig}, are invariant during primary dealloying, as Ag fraction, x_{Ag}, decreases drastically. In the secondary dealloying, while L_{lig} increases due to surface-controlled coarsening, L_{Ag} stays invariant.

4.1.2 Parameters determining the ligament size during dealloying

Since these observations for the evolution of silver cluster size and ligament size in previous subsection are valid for other applied potential as well, one might ask whether ϕ has any influence on L_{lig} and L_{Ag}. In Figure 4.3, the inverse of L_{Ag} and L^0_{lig} of the primary dealloyed structures at each ϕ is shown. Here primary dealloyed structures correspond to the structures at the instant of the end of primary dealloying and the onset of the secondary dealloying stage (the transition points, i.e. open circles, in Figure 3.2a). The inverse of the two characteristic sizes, $1/L_{\mathrm{Ag}}$ and $1/L^0_{\mathrm{lig}}$, are seen to linearly increase as ϕ increases. Most notably, straight lines of best fit to both data sets converge to the identical ϕ-value, $\phi = 0.900 \pm 0.002$ eV, in the limit of infinite size. Thus the corresponding $\phi = 0.900$eV represents the minimum ϕ required for proceeding with dealloying and the evolution of porosity [149]. There appears to be a constant ratio between two sizes based on this observation. The slopes of two fitting lines give the ratio with $L_{\mathrm{lig}}/L_{\mathrm{Ag}} = 1.28$. The invariant ratio is confirmed by the calculation of that ratio at each ϕ, as shown in the inset figure. The ratio in inset exhibits an identical value of 1.30 ± 0.07 for all ϕ.

Figure 4.4a plots the ligament size, L_{lig}, during the secondary dealloying for various ϕ versus t. The data points at different ϕ coincide in a common graph, $L_{\mathrm{lig}}(t)$. Furthermore, at long time $L_{\mathrm{lig}}(t)$ evolves along the scaling growth law $L_{\mathrm{lig}} \propto t^{1/4}$. This growth law usually is applied for processes dominated by surface diffusion [84] and also has been proved to be valid for the NPG coarsening [150]. The coarsening process and the coarsening law of NPG microstructres will be investigated in detail in Section 4.2. An important observation here is that the coarsening at secondary dealloying is dominated by the common graph of $L_{\mathrm{lig}}(t)$. In other words, despite decisively influencing the structural sizes at the primary dealloying stage, the dealloying potential,

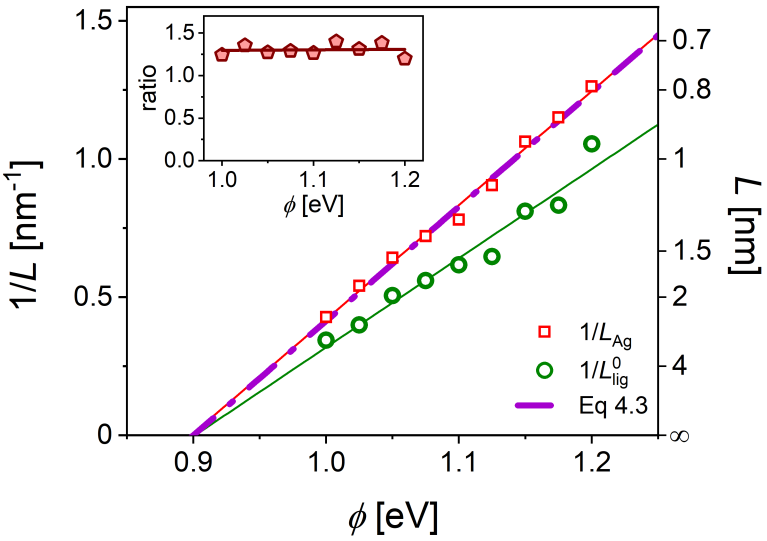

Figure 4.3: Characteristic size during primary dealloying stage for different ϕ. Open symbols: Inverse of Ag cluster size, L_{Ag}, and of ligament size, L_{lig}, of primary dealloyed structures (structures of the instant at transition points (open circles) in Figure 3.2a) as a function of dealloying potential, ϕ. Solid lines: linear fittings of data $1/L_{\mathrm{Ag}}$ and $1/L_{\mathrm{lig}}$, respectively. Note sensibly identical abscissa intercepts at $\phi = 0.900 \pm 0.002$eV of extrapolation for linear fittings. Dash-dotted line: Eq 4.3, the intercept of the abscissa is fitted to the data, and the slope is modeled using the simulation's materials parameters. According to Eq 4.3, the slope predicted by it is about 0.3 lower than the slope actually observed for L_{lig}. Inset figure depicts ratio between L_{lig} and L_{Ag} versus ϕ; The horizontal fitting line in inset indicates a nearly identical ratio of 1.30 ± 0.07 which is independent of ϕ.

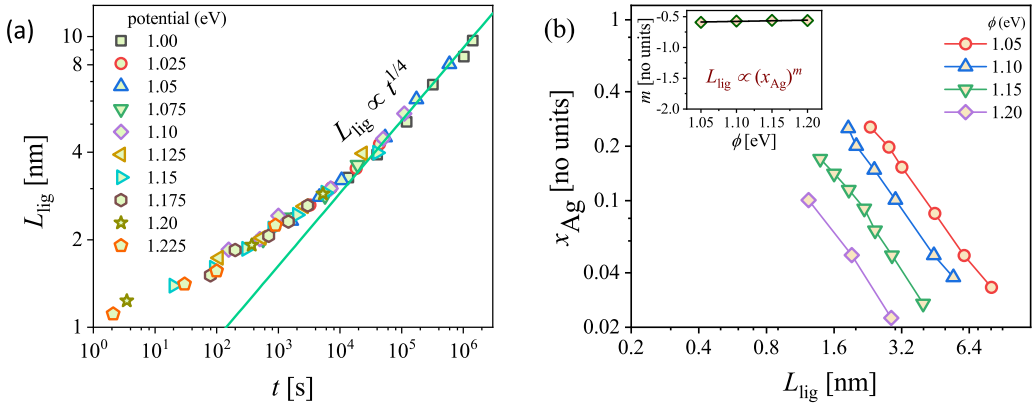

Figure 4.4: Characteristic size during secondary dealloying stage for different ϕ. (a) Ligament size during secondary dealloying, L_{lig} as a function of dealloying time, t, at various ϕ. Note all graphs for different ϕ evolve along identical scaling behavior and trend towards $L \propto t^{1/4}$ for long times. (b) Ag fraction, x_{Ag} versus ligament size, L_{lig} during secondary dealloying. Inset shows the exponent of Eq. 4.1 extracted from fitting of data sets, $m = -0.57 \pm 0.02$. All axes in this figure are shown logarithmically.

ϕ, exhibits little affected to the coarsening kinetics at the secondary stage. Another important observation in Figure 4.4a is that as the secondary dealloying stage takes much longer than primary stage (for example, at ϕ=1.15 eV, it takes a period ranging

from 10^4 s to about 10^6 s which is 99% of the entire dealloying time), the ligament size after dealloying only depends on the dealloying time, t, according to $L_{\text{lig}}(t)$, and is irrespective to ϕ.

Experimental studies [29, 31] have shown the silver fraction in sets of samples of as prepared NPG to go down systematically as the ligament size goes up. Fig. 4.4b shows the Ag fraction x_{Ag} as a function of ligament size, L_{lig} at different ϕ at secondary dealloying. The linear variation in the log-log graph suggests the power law

$$L_{\text{lig}} \propto (x_{\text{Ag}})^m \,. \tag{4.1}$$

The exponent m can be seen from the inset figure to be sensibly invariant of ϕ, $m = -0.57 \pm 0.02$.

4.1.3 Discussion

Ligament size during primary dealloying

Simulation results show that the ligament size varies as $L^{-1} \propto (\phi - \phi_0)$ with $\phi_0 \approx 900\,\text{meV}$. In principle, this law would be expected if ϕ_0 could be identified with the Nernst potential and if the surface curvature, scaling with L^{-1}, can be correlated with overpotential, $\eta = (\phi - \phi_0)/q_{\text{e}}$ by a Gibbs-Thomson relation. A major reason for adopting this concept is that, in the simulation in this work, 900 meV is adequate to compensate for the free energy of alloy crystallization. For the model here, since the lattice here is rigid, the formation energy also corresponds to the enthalpy, which is 6 bonds per atom at bond energies of −150meV, or −900meV. When the rigid lattice consists of pure components, its entropy is zero (in terms of vibrations and configurations). In addition, under our simulation conditions, dissolution events of Eq 2.13 occur much more frequently than diffusion jumps of Eq 2.12. The solid solution's configuration space is then not ergodically sampled within the brief timescale between an Ag atom being exposed to the mobile surface layer and the atom's dissolution. Therefore, the entropy of mixing contributions from master alloys should not significantly affect the processes under investigation.

The proportional relationship between $1/L$ and η implies that it requires higher overpotential to generate smaller structure. This phenomena would be the inverse of the Gibbs-Thomson relation, i.e. a tendency to result in faster dissolution at smaller sizes and a high overpotential.

This inverse behavior of higher overpotential to generation versus dissolution of smaller structures can be explained by the sign of the curvature of the structure: the convex particles (positive curvature) in Gibbs-Thomson relation, but the concave pores (negative curvature) in the dealloying scenario. In a classic coarsening scenario convex particles with smaller size tend to dissolve more readily. The corrosion front, on the other hand, has concave pore channels (negative curvature). To induce porosity evolution, dissolution needs a stronger driving force at small sizes [149, 151]. There has been discussion of an "inverse Gibbs-Thomson effect" in the context of dealloying [67], and an inverse relationship between η and alloy dissolution length scale has been demonstrated experimentally [152]. The results of the simulations in this thesis support that notion.

As has been established in the field, the evolution of the microstructure during dealloying can be attributed to two main competing processes: surface diffusion tends to smoothen the surface corrugation and to passivate, and dissolution creates new pore channels to spread into the virgin master alloy below the surface [55, 149, 153]. As a consequence, no single concept can provide valid predictions of microstructure evolution on its own, such as expressed by the Gibbs-Thomson relation, overpotential correlates with curvature. It is nonetheless true that at each given value of η, the aforementioned relation does set a minimum size limit for the pore channel. Taking this lower limit into account and comparing it with our observations seems worthwhile.

The corrosion front can be modeled as a cylindrical pore channel with diameter L and a hemispherical cup (mean curvature $\kappa = -4/L$), at its end. It is required to have a minimum overpotential of [149]

$$\eta = \frac{\gamma\Omega\kappa}{q_e} = \frac{4\gamma\Omega}{Lq_e}, \tag{4.2}$$

where γ, Ω and q_e denote the specific surface excess free energy (or surface tension), atomic volume and elementary charge, respectively. In our calculations for {111}, {100}, and {110} terraces, the excess energy, evaluated by the broken bonds per area of surface using our values of E_b and a, is γ = 0.50, 0.58, and 0.62J/m^2, respectively. Their average, γ = 0.57J/m^2 is used here as a preliminary estimate of a rough surface. The value of γ for different terraces here is half of the corresponding value calculated in Section 2.2.3. This is because in the dealloying model described in Section 2.2.2, the value of bond energy, E_b, is half that used in Section 2.2.3. To simplify the computation, instead of 1/2, a value of 1 was used for the charge transfer coefficient, α, in Eq.4 in Ref [55] (due to $\alpha = 1$, it is omitted in Eq 2.13 in Section 2.2.2). This essentially scales the bond energy by 1/2. In other words, for dealloying simulations, if $\alpha = 1/2$ in Eq 2.13 in Section 2.2.2, a value of bond energy, E_b = -0.3 eV will be applied which will be identical with the value used in the coarsening scenario.

Solving Eq 4.2 for L and taking $\phi = \phi_0 + \eta q_e$, a lower limit for the pore size, L_{min} can be determined,

$$L_{min} = \frac{4\gamma\Omega}{\phi - \phi_0}. \tag{4.3}$$

An illustration of the prediction of Eq 4.3 in Fig 4.3 is represented by the bold dashed-dotted line of L^{-1} versus ϕ. With the simulation results ϕ_0= 900 meV and the simulation's input values for Ω and γ, Eq 4.3 was adapted to compute the slope. As can be seen, the slope from Eq 4.3 corresponds quite exactly with the data for silver cluster sizes. There is less precision in the agreement with the ligament size, which is the relevant quantity in this case. Taking the slope of the regression equation, it is found that Eq 4.3 underestimates the ligament size by about a factor of 1.3. However, the equation represents a lower limit for the pore size, so this could still be considered as a remarkable agreement. Note that nanoporous metals are expected to have reasonably similar pore and ligament sizes if φ is not too small. Based on the results of this study, it can be concluded that the capillary terms of the Gibbs-Thomson relation are important for linking ligament size to dealloying potential.

Nernst potential can also be estimated using ϕ_0 = 900meV based on the above arguments. When ϕ approaches to ϕ_0, the excess energy will become less and less

available for the creation of surfaces, bulk dealloying won't be possible anymore. It is necessary to impose a critical dealloying potential above ϕ_0, called ϕ_c, to proceed the evolution of the porosity. This expectation is confirmed by the fact that, for $Ag_{75}Au_{25}$, the model's ϕ_c is in the range of 900 to 950 meV [55]. However, our simulation does not support such a scenario conclusively. Since the fact that it is ignored in the algorithm that silver atoms can be redeposited, the equilibrium between dissolution and redeposition through the exchange current, which is described as Nernst potential, cannot be captured in the model.

Ag cluster size during primary dealloying stage

A key application of dealloying is to form nanomaterials with extremely small microstructures, as described in the introduction. Therefore, it would be interesting to investigate how dealloying conditions impact ligament size. This lower limit is determined by the primary dealloying. It is challenging, yet, to isolate the primary dealloying ligament size in typical experiments due to the two dealloying processes (primary and secondary) occurs simultaneously. Previously, it has been discussed how the dealloying potential impacted the dealloying ligament size. Here it will be explored how the aforementioned challenges can be resolved.

Although, it may be challenging to discuss L in absolute terms, but it is easier to discuss in ratio terms, $L^0_{\mathrm{lig}}/L_{\mathrm{Ag}}$. Essentially, it results from a passivating layer being redistributed on the pore surfaces due to the remaining more noble element. If the microstructure remains fairly self-similar, it is also likely that the relative quantities of the remaining more noble elements and the remnants of the pristine master alloy will also remain relatively similar. Passivation layer thickness scales with ligament size, which results in self-similar product structures. A significant finding from our analysis is that $L^0_{\mathrm{lig}}/L_{\mathrm{Ag}} = 1.3$ regardless of the absolute ligament size of the primary dealloying. In light of the finding that L_{Ag} also remains stable after coarsening, postmortem examinations of the silver cluster size in dealloyed NPG may help identify the size of the initial structure established by the primary dealloying. It has been demonstrated by TEM [31, 60] and by atom probe tomography [68] that size of those survived Ag clusters can be measured in experiments. Based on measurements of L_{Ag}, L^0_{lig} can be inferred. Thereby, experiments could provide a database that finally would enable us to conclude on initial structure size during the primary dealloying.

Studies of dealloying also explore the cluster size from a different perspective: the parting limit. The parting limit is simply the minimum amount of less noble element that must be present for bulk dealloying to take place. Intrinsically, this relates to percolation thresholds: percolating clusters of less-noble elements must spread the macroscopic volume of the solid solution in order for bulk dealloying to occur [154–156]. When percolating at high density sites, the size of the ligaments may be related to the lateral extension of percolating clusters if the fraction of less noble element is close to the parting limit [62, 152]. x_{Ag} in the master alloy of our simulations was considerably higher than the parting limit. As demonstrated by Fig 3.4a, a single, extended cluster of silver indeed appears within the master alloy. As a result, after primary dealloying, the characteristic structure size is not governed by the size of the percolating silver clusters in the master alloy. In contrast, there are plenty of considerations relating to the competition between passivation and corrosion, as well as the instabilities of the

advancing corrosion front [50, 55]. In addition, Eq 4.3 entails a lower limit for the characteristic length scale because of the balance of energy in Gibbs-Thomson-type relations.

Ligament coarsening during the secondary dealloying stage

During the secondary dealloying process, the ligament size evolves asymptotically at large time to follow the power law scaling of $L \propto t^{1/4}$. In spite of the fact that not all experiments agree on a well-known scaling law for NPG coarsening [71, 86, 87], the $L \propto t^{1/4}$ law fits well with the theory established by Herring [84] for the curvature-driven coarsening based on surface diffusion. This scaling and the coarsening behavior of NPG microstructures will be demonstrated in kinetic Monte Carlo simulations of coarsening in Section 2.2.3.

The surface diffusion is not correlated with the alloying potential in the model in this study. The coarsening appears independent of ϕ in this work. It should be acknowledged that the experimental situation may be different. This is because the applied potential may have a significant impact on the surface diffusion coefficient [157, 158] and, consequently, on the coarsening rate [29].

Ag cluster size during secondary dealloying stage

Our simulations reveal that, despite coarsening of the ligaments into which silver clusters are embedded, the characteristic length scale of silver clusters retains its original size from primary dealloying. In this context, it is worth emphasizing the fact that for gold at room temperature, equilibrium vacancy concentrations and bulk diffusivity are extraordinarily low [29, 159]. Our simulations have accounted for that latter observation, which means that bulk diffusion is not considered in our simulation code. Consequently, as long as the silver clusters remain buried in ligaments with a passivation surface layer of Au atoms, their configuration is frozen resulting in a constant mean size. In response to ligaments becoming coarser, gold is redistributed along the ligaments surface by surface diffusion. Dissolution of silver occurs whenever the silver cluster is exposed to the surface. This will result in the cluster rapidly shrinking and disappearing.

4.2 Ligament size evolution during coarsening

The porous network with interconnected ligaments and nodes of NPG has been established during dealloying. The microstructure of as-prepared NPG will be changed during the coarsening process. A fundamental understanding of the microstructural evolution of NPG during coarsening is essential for further tuning and optimization of its chemical, catalytic as well as mechanical properties. In fact, experimentalists often use the coarsening process as a technique for post-dealloying processing, namely for tuning the ligament size. In this section, the coarsening process of NPG microstructures will be investigated in isolation, independent of the dealloying.

KMC coarsening simulations were run on the open source platform SPPARKS with periodic boundary conditions in 3D. The simulation method is introduced in detail in Section 2.2.3. The initial NPG structures with solid fraction in the range covered by experiments were prepared by using the leveled-wave model (see Section 2.1.1 and Section 2.1.3). The ligament size of coarsening simulations generated structures was analyzed (see Section 2.3.2 for detailed information of ligament size evaluation). The evolution of morphology and ligament size during coarsening will be explored in this Section. The coarsening law for NPG network will be revealed. The impact of temperature and simulation box edge length on the coarsening will be also discussed.

4.2.1 Temperatures and initial configurations

For coarsening simulations, two temperatures were used: T = 900K and 1800 K. Those two temperatures were chosen based on the following considerations: (i) T < 900K will cost prohibitive computing time due to the higher energy barriers for transport cannot be efficiently overcome at low T. (ii) T > 1800K, the vacancy concentration and the fraction of single atoms in the (lattice-) gas are no longer negligible and so bulk transport may start to contribute. Figure 4.5a and b show the equilibrium status of simulated Wulff shapes of the nanoparticles at 900 and 1800 K, respectively. In contrast to the perfect faceted surface at 900 K in Figure 4.5a, the Wulff shape of nanoparticle at 1800 K shows a rougher surface with numerous surface defects. The difference in the degree of surface roughness gives the chance to investigate the impact of thermal roughening on the microstructure evolution during coarsening.

The initial configurations with different solid fractions, φ, for the coarsening simulations are generated by the leveled-wave model. Taking the configuration at $\varphi = 0.35$ as an example, as shown in Figure 4.5c, the leveled-wave generated microstructure shows the nanoscale bicontinuous network which resembles structure of experimental NPG. Surfaces in this initial state are rough due to the projection of the leveled random field onto crystal lattices. This configuration corresponds to 120 wavevectors with a H value of $\sqrt{449}$. The distribution and orientation of those 120 wavevectors are shown in Figure 4.5d. In reciprocal space, the directions of the 120 wavevectors are uniformly distributed around the unit sphere. As a result, there is no apparent microstructural texture observed from the initial configuration in Figure 4.5c. Figure 4.5e and f display the final coarsened microstructures at 900 K and 1800 K, respectively. The ligaments were coarsened while the bicontinuous network is maintained. The coarsened structures exhibit some visible microstructural textures with ligaments preferentially

oriented parallel to the simulation box edges.

4.2.2 Evolution of morphology

Figure 4.6 shows renderings of subsets with the size of $50 \times 50 \times 50$ lattice spacings of the entire simulation box, exhibiting the microstructure evolution. The initial state in Figure 4.6a shows small ligaments with rough surfaces. Snapshots of structures after the relaxation but before substantial coarsening occurs at T = 900 K and T = 1800 K are shown in Figures 4.6b and c, respectively. These figures testify that the surface of NPG samples evolves from the initial rough state toward the more favorable faceted surfaces during the initial relaxation process even for the smallest structures. Figures 4.6d and e show the final state of coarsened structures at 900 K (d) and 1800 K (e). It shows more

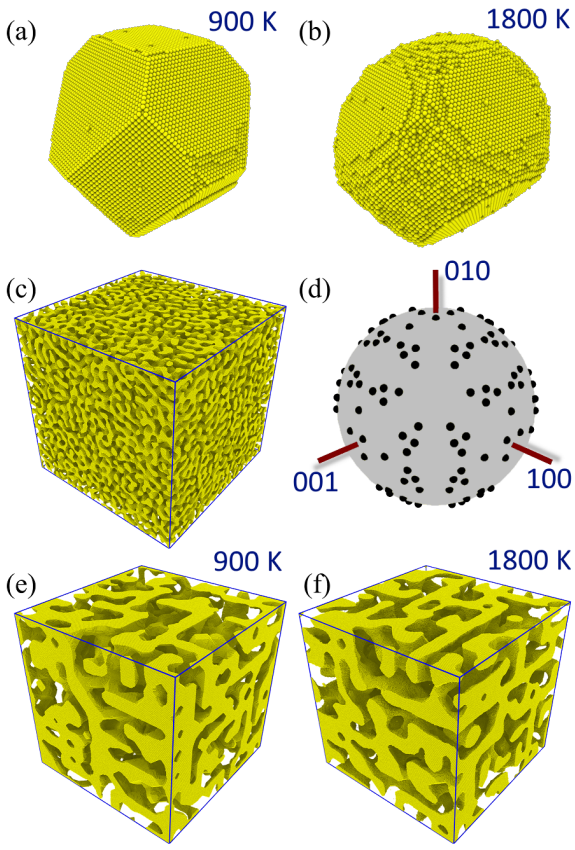

Figure 4.5: Simulation temperatures, initial configuration and coarsened microstructures. (a) and (b) show Wulff shapes of nanoparticles at equilibrium status for temperatures T = 900K and 1800 K, respectively. Note the faceted surface at T=900 K and more rough surface at 1800 K. (c) displays the initial leveled-wave configurations with solid fraction, $\varphi = 0.35$. (d) illustrates the 120 wavevectors (black dots), used for generating the microstructure in (c), projected onto the unit sphere in the reciprocal space. The 100-type orthogonal coordinate system is also shown. (e) and (f) show final structures during coarsening for initial structure (c) at 900 K and 1800 K, respectively. Note the microstructural texture appears in the coarsened structure. The cubic simulation box in (c), (e), (f) has the edge length of 200 lattice spacing and directions of [100], [010] and [001]. Yellow spheres denote Au atom positions.

prevailing {111}- and {100} terraces, with similar numbers of atoms in both. Notably, the surface of the structure at lower temperature forms as large facets, whereas rougher surfaces are observed at the higher temperature.

4.2.3 Evolution of characteristic size

Two different strategies were used when generating the initial configurations. Initial structures for the simulations at 900 K were produced to have the identical apparent ligament diameter, L_{ap} but different characteristic spacing $\tilde{L}$ by selecting different H, therefore different random fields with different characteristic q to achieve identical specific surface area, S_{V}. By contrast, for the simulations at 1800 K, the initial structures were generated with identical $\tilde{L}$ while different L_{ap}. To realize this, different values

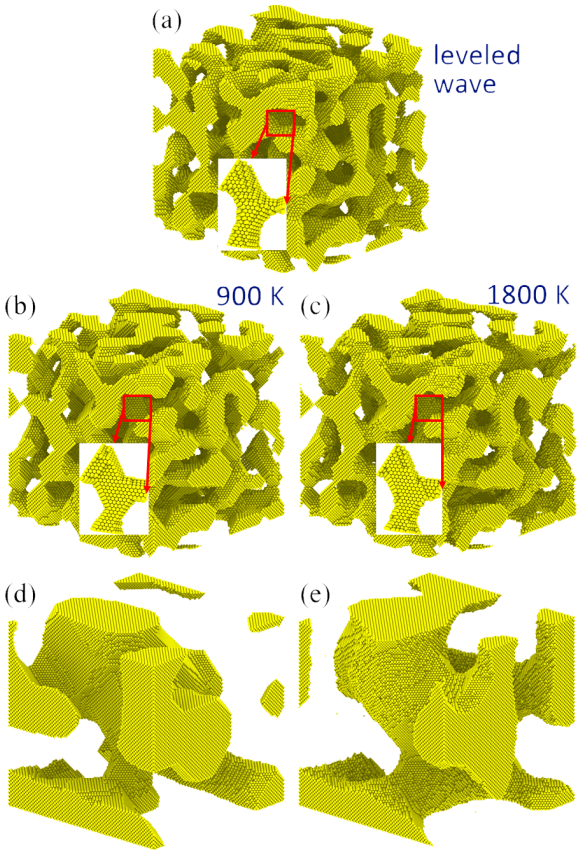

Figure 4.6: Subset renderings of microstructure evolution during coarsening at different T with $\varphi = 0.35$. (a): initial configuration with rough surface generated by the leveled-wave method. (b) and (c): the relaxed structures prior to significant coarsening. (b), structure at $t = 1.1 \times 10^6\,\nu^{-1}$ at temperature $T = 900$ K; (c) structure at $t = 10^8\,\nu^{-1}$ at $T = 1800$ K. An example ligament is shown in (a)-(c) insets respectively, which show the initial roughness and faceting during relaxation. (d) and (e): final coarsened structure at $T = 900$ K (d) and 1800 K (e). Note different roughness between structure at two temperatures: lower temperature produces large facets, and higher temperature produces rougher surfaces. Subsets shown here are cut from entire simulation box and have the same size of $50 \times 50 \times 50$ lattice spacings. The displayed yellow spheres represent the positions of the atoms.

were chosen for level cuts on the same random field to get a structure with different φ. The mentioned H and q are parameters used in the generation of Gaussian random fields for the leveled-wave model (see Section 2.1.1). More detailed description for the sample preparation of coarsening simulations refers to Section 2.2.3.

Figures 4.7a and b depict the evolution of two sizes, L_{ap} and $\tilde{L}$ versus time for structures with different the solid fractions, φ during coarsening at 900 K and 1800 K, respectively. L_{ap} and $\tilde{L}$ in the figure were determined by Eqs 2.23 and 2.25 respectively, with the specific surface area analyzed by Ovito based on the Delaunay tessellation of the atomic structure of the solid (see Section 2.3.2). Those values of sizes for the initial configurations are systematically smaller (by $11 \pm 2\%$) than their representative values analyzed directly from, first, the leveled random fields [32]. The deviation comes from the discrete atomic roughness of the initial surface which will increase the surface area, A. Second, in the surface reconstruction algorithm, the position of surface atoms centers are treated as the surface. The leveled wave surface is dislocated inward by these displacements. The solid volume, V_{S}, is thus underestimated. As a consequence, the specific surface area, S_{V}, is overestimated which leads to the smaller size values in the figure. The sizes analysis method for the leveled random field can only work on the initial configurations and not to the coarsened structures (see Section 2.3.2 for detailed information). It is then the precise value of ligament size can be assessed only for the initial configurations based on the leveled-wave model. By contrast, the surface reconstruction method has to be used to estimate the ligament size of coarsened structures. In spite of these systematic variations, the sizes match the template of the leveled-wave very well.

Graphs in Figures 4.7a and b exhibit three stages of size evolution during coarsening. Firstly, the sizes stay sensibly invariant for a very short time. This stage corresponds to the surface relaxation which brings the initial rough surface to the more faceted state as discussed in Figure 4.6. Then the sizes grow with the power law of $t^{1/4}$ (solid line in figures) which is consistent with the classical growth law for curvature-driven surface diffusion process based on Ref [84]. Finally, the coarsening slows down. A tentative explanation is the effect of the finite size of the simulation box that once the ligament size approaches the box size, the microstructure evolution no longer represents bulk behavior. This issue will be inspected at the end of this subsection, see below. It is seen that the above observations are generally applied for simulations at both temperatures.

The most remarkable point from Figures 4.7a and b is the different convergence behavior of graphs for L_{ap} and $\tilde{L}$. They start from the same initial L_{ap}, the evolution of L_{ap} can be seen in Figures 4.7a to depend on φ. By contrast, Figure 4.7a and b show that the $\tilde{L}$ of structures with different φ converge to a common graph, even when the initial $\tilde{L}$ differs. The finding of an evolution of $\tilde{L}$ independent of φ indicates that $\tilde{L}$ instead of L_{ap} is the intrinsic size parameter to describe the coarsening behavior of nanoporous metal networks.

If a focus is put on the comparison between simulations at two temperatures in Figures 4.7a and b, it is found that compared to 900 K, coarsening occurs almost 2 orders of magnitude faster at 1800 K. Except for the acceleration, the coarsening behaviors at 900 K and 1800 K show qualitative agreement with each other even though their surface morphologies, as discussed in Section 4.2.2, are different as faceted at 900 K versus rough at 1800 K. Graphs of $\tilde{L}$ evolution of the simulations for structure

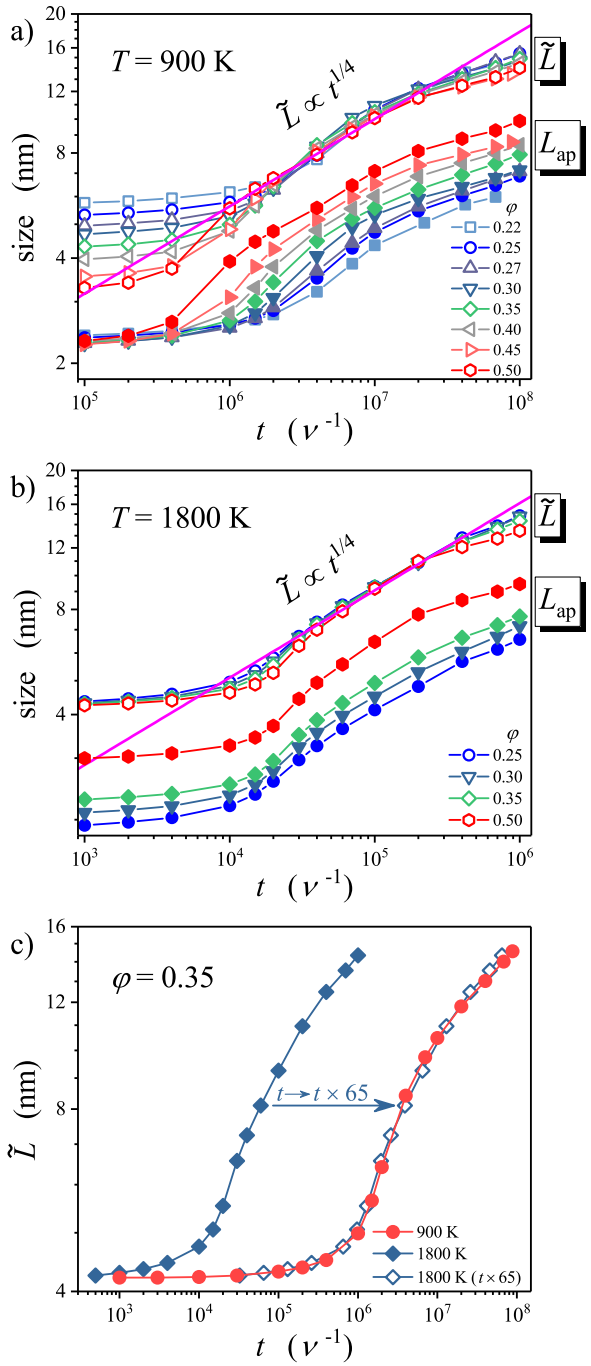

Figure 4.7: Time-evolution of characteristic structure sizes during coarsening. (a) and (b): Apparent ligament diameter, L_{ap}, (closed symbols) and characteristic spacing between neighboring ligaments, $\tilde{L}$, (open symbols) versus time, t, of structures with different solid fractions, φ, during coarsening at temperatures T = 900 K (a) and 1800 K (b). Symbol shapes are linked to φ in legends. The straight line represents the $t^{1/4}$ kinetics (with arbitrary prefactor). Note curves of $\tilde{L}$ converged and curves of L_{ap} diverged. (c): Kinetic comparison of different temperatures for φ = 0.35 structure. Closed symbols denote direct simulation results and open symbols show results at 1800 K with the time axis multiplied by 65. Note the graph after a shift of results at 1800 K (open symbols) exhibits superposition with the graph of 900 K. All axes in this figure are shown logarithmically.

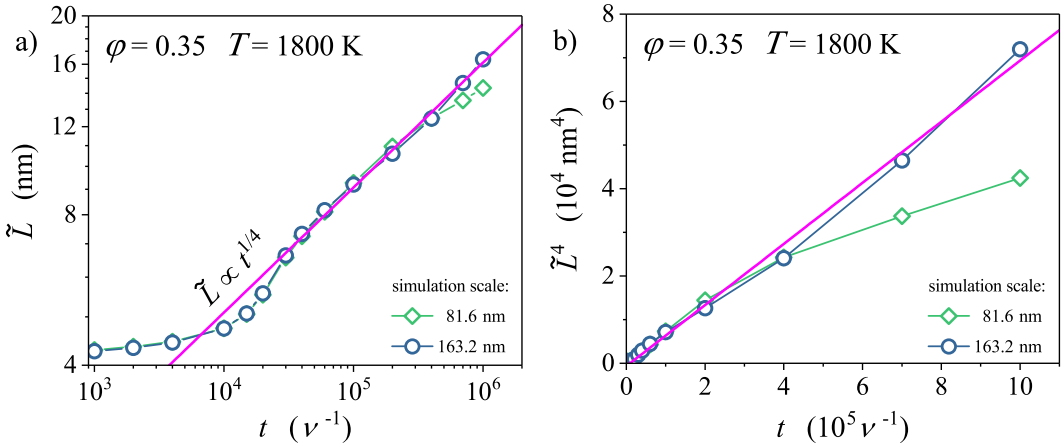

Figure 4.8: Comparison of coarsening with different simulation box sizes. Exemplified by T = 1800K and φ = 0.35, (a) shows a log-log graph of characteristic ligament spacing $\tilde{L}$ as a function of time t. Diamond symbols: standard size simulation box with an edge length of 200 lattice spacings (81.6 nm); Circle symbols: larger simulation box with an edge length of 400 lattice spacings (163.2 nm). Solid line: $t^{1/4}$ kinetics (with arbitrary prefactor). Slowdown at the third stage is only seen for the graph of the smaller box indicating the effect of the artifact of the finite box size. (b) shows $\tilde{L}^4$ as a function of t with the same data. Note the linearity of the graph of $\tilde{L}^4(t)$ for the larger box. Data in this figure confirms that the coarsening law of the simulation is inherently $\tilde{L} \propto t^{1/4}$.

with $\varphi = 0.35$ at 900 K and 1800 K in Figures 4.7c exemplified the quantitative comparison of coarsening between temperatures. The same initial configuration was used for simulations of structure with $\varphi = 0.35$ at 900 K and 1800 K. It is seen that if the time axis of the graph of $\tilde{L}(t)$ at 1800 K is multiplied by 65, then the new graph (open symbols) coincides quite precisely with the graph at 900 K. This precise consistency indicates the same temperature-dependence throughout the evolution of the microstructure.

Let's recall the observation of the slowdown of coarsening at the third stage in Figures 4.7 where the reason was argued as the effect of the finite simulation box. To verify this argument and the power law coarsening of $t^{1/4}$, an extra simulation for the structure with φ= 0.35 and with the edge length of the simulation box doubled compared to the previous runs (i.e. 400 lattice spacings or 163.2 nm) were performed at T= 1800 K. The sizes of initial configuration for larger simulation box are identical with the structure with φ= 0.35 of previous runs (Tables 2.1 and 2.2). Figure 4.8a shows how $\tilde{L}(t)$ evolves over time at 1800 K for simulations with larger (circle symbols) and standard (diamond symbols) simulation box. The coarsening law of $t^{1/4}$ continues until the time range corresponds to the third stage for the runs with the larger box which indicates the slowdown in this stage of coarsening with a smaller box is indeed caused by the box size. It is seen that graphs for two different box sizes are superimposed which confirms the growth scaling law, $t^{1/4}$. This coarsening power law is further supported by the linearly increasing evolution of $\tilde{L}^4(t)$ in Figure 4.8b.

4.2.4 Discussion

Assessing the initial microstructures

The experimental observations of coarsening of dealloying-made nanoporous gold motivated the study of coarsening simulations. The two processes, dealloying and coarsening, are fundamentally different. The less noble elements are dissolved by chemical or electrochemical driving forces, increasing porosity and surface area over time. A coarsening process, on the other hand, is driven by the desire to reduce the net excess surface energy introduced by dealloying. Porosity is retained during this process, while surface area decreases. The coarsening simulations in this study is motivated to explore the coarsening behavior and the evolution of connectivity in the bulk (the evolution of connectivity during coarsening will be discussed in Section 5.3). It requires large-scale NPG model structures as the basis for coarsening. The numerical NPG structures used in this work which have 32 or 256 million sites are not conveniently generated by KMC dealloying simulations. It thus another NPG structures generation approach have to be found for the initial configurations of coarsening simulation in this work.

These initial structures are approximated by the leveled random field that provides microstructure at the end of the early-stage spinodal decomposition [111]. Therefore, the findings in this work are also relevant to how the spinodal structure varies during coarsening, in other words, to the late-stage spinodal decomposition. The initial structures may not obviously be able to provide useful approximations to the microstructure of nanoporous gold due to the distinct differences between dealloying and early spinodal decomposition. Yet, Ref [32] shows microstructure based on leveled random fields have excellent agreement with experiments on nanoporous gold in terms of elastic properties and of the scaled genus. The leveled wave model is distinguished as that model which has by far the strongest confirmation of similarity to experimental NPG. The initial configurations in this work are motivated by and supported by the above considerations.

Microscopic details of the KMC simulation of diffusion

A simplified representation of the experimental scenario is the basis of our KMC approach. In our simulations, the rigid lattice prevents surface atoms from relaxing at the atomic scale, as well as capillary forces induced long-range bulk plastic and elastic deformation. A simplified formulation of the activation energies of the individual diffusion events is used, with no consideration for the possible impacts of adsorbates. It focuses instead on the most basic principles behind the coarsening of metal network structures, that is, the (anisotropic) excess energy of the surface and the diffusion of that energy along the surface and the step edges, rather than through the bulk. A comparative study of KMC simulations in Refs [55, 160, 161] shows that this model is adequate as semiquantitative agreement with experimental data on various aspects of the evolution of the structural properties of NPG through dealloying.

Our KMC simulation does not represent coarsening timescales quantitatively due to its simplified representation of diffusion. Nevertheless, one may wonder if the simulation reflects the coarsening rate roughly realistically. Using the value $\nu = 10^{12}$ s^{-1} for the attempt frequency [127, 129], at 900 K, an increase of ligament size from 4 to 16 nm during coarsening will take $10^8\nu = 100\mu$s (see Fig 4.7(c)). At room temperature, the same coarsening process would take slightly over half an hour if extrapolating the

kneitc by using the activation energy of 0.65 eV. The time constant in NPG appears reasonable since several hours of dealloying at room temperature produces NPG samples with ligament sizes of 20-40 nm [107] due to coarsening behind the dealloying front ("secondary dealloying" [161, 162]).

Kinetics of coarsening and appropriate size parameter

It is emphasized in this study that the characteristic spacing between ligament centers, $\tilde{L}$, is more intrinsically associated with the coarsening kinetics than the ligament diameter, L_{ap}, with regard to the microstructure evolution controlled by surface migration. It is relevant since many experiments on NPG use a average size of ligament diameter L, –similar to our L_{ap}–to parameterize the characteristic microstructural length scale. Through electrochemistry, other experiments calculate L as the inverse of a specific surface area. From information in reciprocal space, it is possible to determine the more intrinsic parameter $\tilde{L}$ which links to an underlying wavelength. Small-angle scattering experiments [112, 113, 163] or fourier transforms of electron micrographs [71] can provide this information based on peak positions. Yet, there are rarely experimental studies that have reported $\tilde{L}$. This study shows that coarsening kinetics follow the expected $t^{1/4}$ scaling law for coarsening process dominated by surface migration [84].

Chapter 5

Evolution of the nanoporous network's connectivity

Studies of the mechanical properties of nanoporous metal [82, 96–98] emphasize that the connectivity is an important microstructural characteristic of NP metal. The questions of how the connectivity is generated on nanoporous network and how will the connectivity evolve are still not fully understood at the onset of this thesis. In this Chapter, the evolution of nanoporous network's connectivity during the processes of dealloying (Section 5.1), shrinkage (Section 5.2) and coarsening (Section 5.3) will be investigated.

5.1 What connectivity is generated during dealloying

In Section 4.1, the evolution of ligament size, L, of the structures generated by dealloying simulations in Chapter 3 has been exhibited. In this section, the topological genus, G, of the same sets of dealloying simulations generated structures will be evaluated by using the open-source software CHomP [148]. Based on the results of L and G, the evolution of connectivity, g will be explored. In Chapter 3, the composition of initial configuration is $Ag_{75}Au_{25}$. In order to reveal the impacts of solid fraction, φ, on g of dealloying-made structures, new dealloying simulations were run with composition of initial configuration $Ag_{65}Au_{35}$.

5.1.1 Generation of genus during dealloying

As the connectivity of nanoporous networks depends on their φ [32], here two sets of simulation with Au fraction in the master alloy, x_{Au}, is 0.25 and 0.35 were run. Figure 5.1a and b plot genus, G, as a function of time, t, during dealloying. G first increases to a peak point for all dealloying potentials, ϕ. This increasing part of the curve corresponds to the generation of a porous microstructure, consisting of ligaments and tunnels, during the primary dealloying stage. The increasing of G is because the formation of porosity during the establishing of the 3D nanoporous network (see Figure 3.2b to d). Then G decreases during secondary dealloying due to the coarsening of the ligaments (see Figure 3.2d to e). Figure 5.1c shows genus of the primary dealloyed (at the end of primary dealloying stage) structures, G_0, at various ϕ for dealloying of

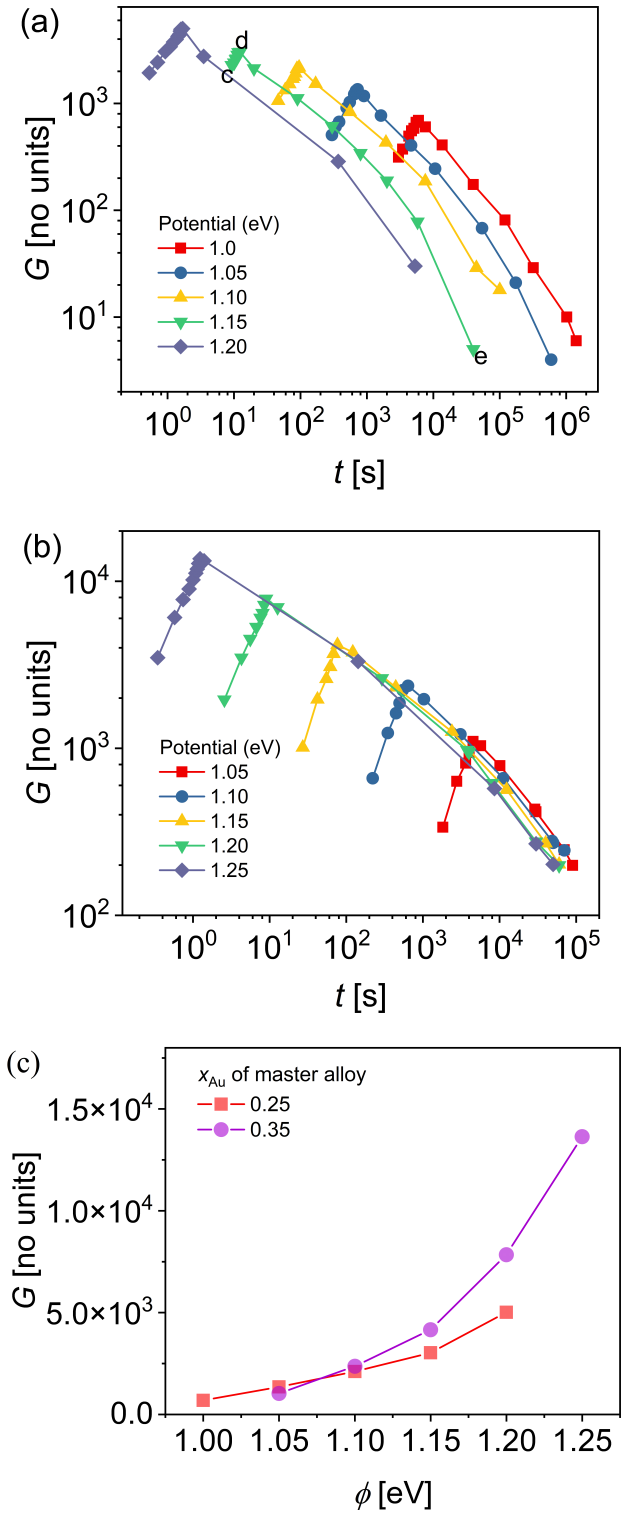

Figure 5.1: Topological genus, G, as a function of dealloying time, t, at different ϕ with Au content in master alloy (a) x_{Au}=0.25 and (b) x_{Au}=0.35. Open symbols in (a) show G value of respective microstructure shown in Figure 3.2 c to e. (c) Genus of the primary dealloyed structure, G_0, versus dealloying potential, ϕ. Here, the primary dealloyed structures represent the structures at the end of primary dealloying (the transition point in Figure 3.2). G_0 is then the peak point of each graph in Figure (a) and (b).

x_{Au}=0.25 and x_{Au}=0.35. G_0 increases with increasing of ϕ. It is seen that G_0 of structures at x_{Au}=0.35 dealloying is essentially higher that at x_{Au}=0.35 dealloying except the value at $\phi = 1.05$ eV.

5.1.2 What connectivity is generated during dealloying

To investigate the evolution of solid fraction, φ, during dealloying, the φ versus the dealloying time, t, at different potentials, ϕ, and for x_{Au}=0.25 and x_{Au}=0.35 is displayed in Figure 5.2 a and b, respectively. It is seen that φ decreases as dealloying proceed at both x_{Au} because of the further dissolution of Ag atoms during secondary dealloying stage.

The comparison between the dealloying potential, ϕ, shows that the lower ϕ generates structures with higher initial φ and φ decreases more rapidly. This finding is consistent with the observation in Figure 3.2a in Section 3.2 that residual Ag of primary dealloyed structures decreases linearly as ϕ increasing. The further dissolution of Ag in secondary dealloying requires the moving away of the surface monolayer of Au atoms. The more Ag content of structures at lower ϕ leads to more rapid dissolution once the buried Ag clusters are exposed to the surface. When all the residual Ag atoms are removed from ligaments, the φ value will go to the value of x_{Au}, i.e. 0.25 and 0.35, for the reference dash line in the graphs. Figure 3.2b also shows that φ of the primary dealloyed structure exceed 0.5 at $\phi = 1.15$ eV, 1.10 eV and 1.05 eV for the dealloying of x_{Au}=0.35.

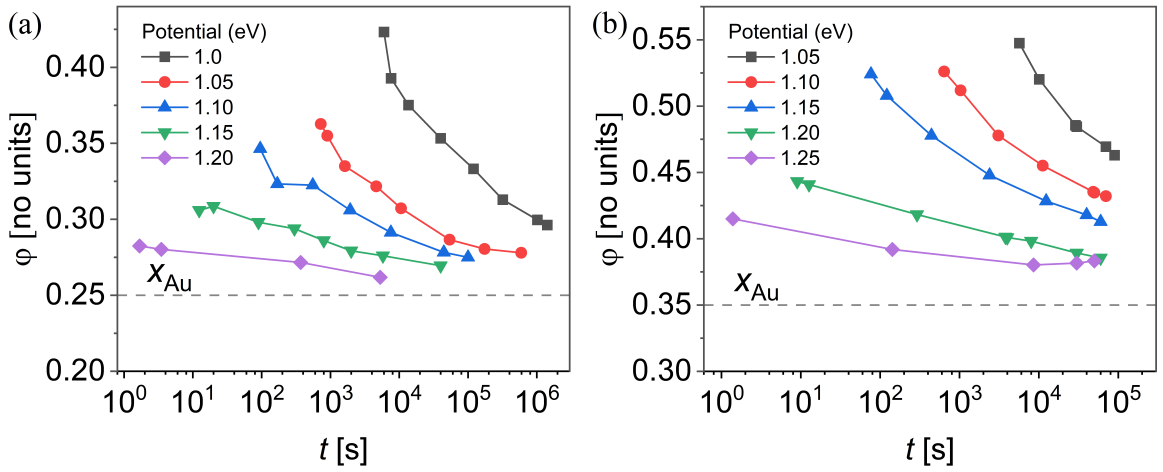

Figure 5.2: Evolution of solid fraction, φ, during secondary dealloying of x_{Au}=0.25 (a) and of x_{Au}=0.35 (b). The first point of the data at each ϕ represents the φ of the primary dealloyed structure at the corresponding ϕ.

Figure 5.3 plots g as a function of L at various ϕ with x_{Au}=0.25 (Figure 5.3a) and x_{Au}=0.35 (Figure 5.3b). L is normalized with the initial value, L_0. Here, L_0 is the ligament size of the primary dealloyed structures. Figure 5.3a shows that g of the structures with x_{Au}=0.25 depends on ϕ, irrespective of the state of coarsening. Higher potential gives a smaller scale genus. By contrast, as shown in Figure 5.3b, the g graphs at x_{Au}=0.35 evolve to a certain value at all ϕ as L increasing. It shows that g

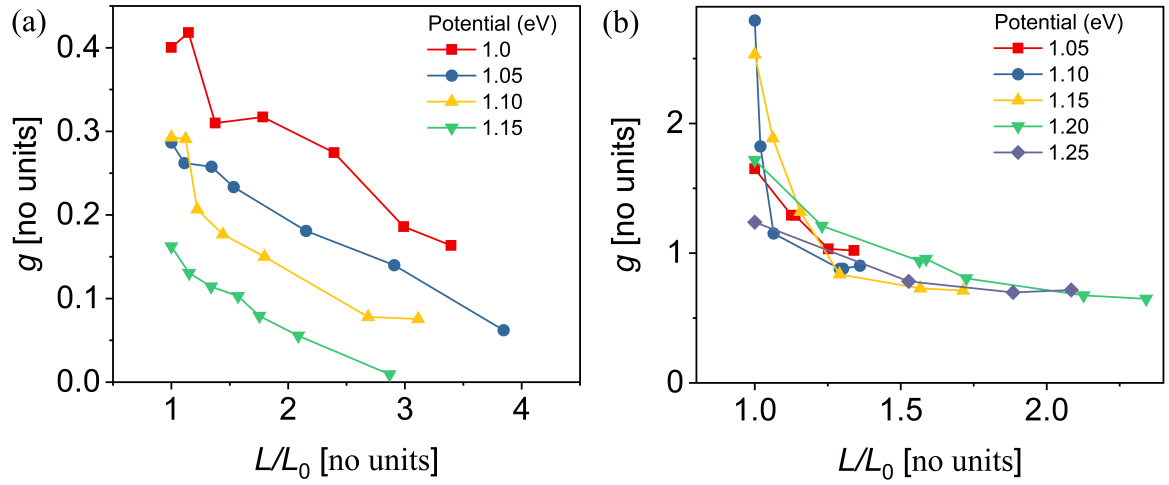

Figure 5.3: Scaled genus, g, versus characteristic size, L/L_0 during dealloying of simulation for the gold fraction in master alloy, x_{Au}=0.25 (a) and of x_{Au}=0.35 (b). L_0 is the ligament size of the primary dealloyed structures.

decreases rapidly at the beginning of coarsening and then g evolves to a straight line with an identical value for various ϕ.

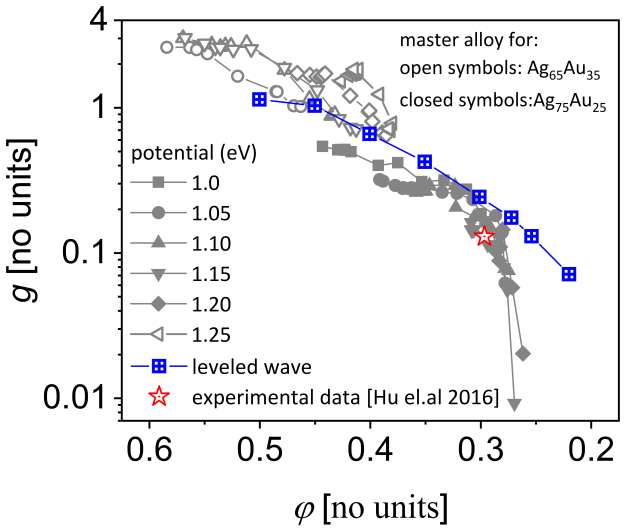

Figure 5.4: Scaled genus, g, versus solid fraction, φ. g at different dealloying times versus φ for structures dealloying at various dealloying potentials, ϕ for Au content in master alloy of 0.25 and 0.35. Fraction of Au atoms in master alloy for open symbols: $Ag_{65}Au_{35}$ and for closed symbols: $Ag_{75}Au_{25}$. Blue cross square symbols represent g of leveled-wave structures shown in Table 2.1. With Eq. 2.23, the ligament size, L, for all leveled-wave structures were calculated with L=2.9±0.1 nm. Red star symbol is the experimental data by focused-ion-beam sectioning (FIB) method [20]. Note that the abscissa is displayed as φ decreasing from right to left because φ decreases with the removal of Ag atoms during dealloying.

The leveled-wave structures show excellent agreement with experimental as-

dealloyed nanoporous samples on the connectivity and on the mechanical properties [32]. Here g values of leveled-wave structures were used as a benchmark to compare with the g evolution during dealloying.

There is an analytical equation for the relation of scaled genus, g, and solid fraction, φ, for the leveled-wave model (Eq.16 and Fig.5 in Ref. [32]). The ligament spacing, $\tilde{L}$, is used to scale the genus there. However, the ligament size, L, of the dealloying simulation made NPG structures in this work was assessed by using the envelope function. The L here is the same with the mean ligament diameter, L_{ap}, which is different with $\tilde{L}$. The difference between L_{ap} and $\tilde{L}$ has been introduced in Section 2.1.2. It is thus convenient to use the same method to calculate L for leveled-wave model generated structures. Based on the previous considerations, those numerical leveled-wave structures in Table 2.1 were used here. The value of L and g of leveled-wave structures was evaluated by the same methods used for the KMC-dealloying generated structures.

The scaled genus, g, calculated via Eq. 2.32 for leveled-wave structures is depicted in Figure 5.4 as blue cross square symbol. From the autocorrelation function, by using Eq. 2.23, the ligament size, L, for all leveled-wave structures was calculated as L=2.9±0.1 nm. Comparing the data of different x_{Au} values it is seen that, the graph of g for x_{Au}=0.35 is either above or on the graph of leveled-wave structure. Yet, the g data of x_{Au}=0.25 is either on the graph of leveled-wave structure or lower. When $\varphi < 0.3$ for the x_{Au}=0.25 runs, g of dealloyed structures decreases dramatically and does not evolve along the graph of the leveled-wave structure anymore. The reason for the rapidly decreasing of g when $\varphi < 0.3$ is because of the non-self-similar coarsening of the nanoporous network for structures with $\varphi < 0.3$. It shows dealloying simulation generated structure has similar g value with the experimental data by focused-ion-beam sectioning (FIB) method from Ref. [20].

5.1.3 Discussion

The results of genus, G, for different x_{Au} shown in Figure 5.1c, namely, lesser G at lesser x_{Au}, are consistent with experimental observations that the network is well-connected for as-dealloyed NPG at φ = 0.35 while there are numerous broken ligaments in φ = 0.25 NPG [23, 24]. As shown in Chapter 3, the primary dealloying stage plays an important role to establish the 3D bicontinuous network. The formation of the porous structure leads to the increase of G during the primary dealloying. The G value at the end of primary dealloying is higher for x_{Au}=0.35 except for the structure at ϕ = 1.05 eV. Note the bicontinuous network of NPG is symmetrical with the φ = 0.50 for the solid and pore phase. Thus, the lower G at ϕ = 1.05 eV for x_{Au}=0.35 is observed due to the φ = 0.56 (Figure 5.2b) which exceeds 0.5. The decreasing of G after a maximum value is because of the coarsening during secondary dealloying.

During the secondary dealloying, the dissolution of the buried Ag clusters makes the ligaments thinner and the solid fraction smaller. These two effects occur simultaneously with ligaments coarsening. The dissolution makes the secondary dealloying process different from the coarsening which will be discussed in Section 5.3. The finding that g evolving along the data set of leveled-wave model when $\varphi \geqslant 0.30$ during secondary dealloying indicates that the removal of the Ag atoms from the nano-ligaments will

not affect connections in the network. In other words, the connections in network are established by the primary dealloying and retained during secondary dealloying when $\varphi \geqslant 0.30$. This finding also emphasizes the validation of the leveled-wave model, even though the two NPG structure generation processes are different. In Section 5.3, the evolution of connectivity during coarsening will be investigated in isolation, independent of the dealloying based on the initial configurations generated by the leveled-wave model.

5.2 Evolution of connectivity during shrinkage

This section will explore the results of connectivity evolution during volume shrinkage of NPG structures. Based on the leveled-wave model, an unrelaxed structure with a realistic microstructure morphology is generated (see Section 2.1.4 for detailed description). Then the numerical NPG structure is feed to MD simulation and see how the realistic interatomic potentials prompt relaxation (see Section 2.2.4 for the description of the MD simulation).

5.2.1 Initial and relaxed microstructure

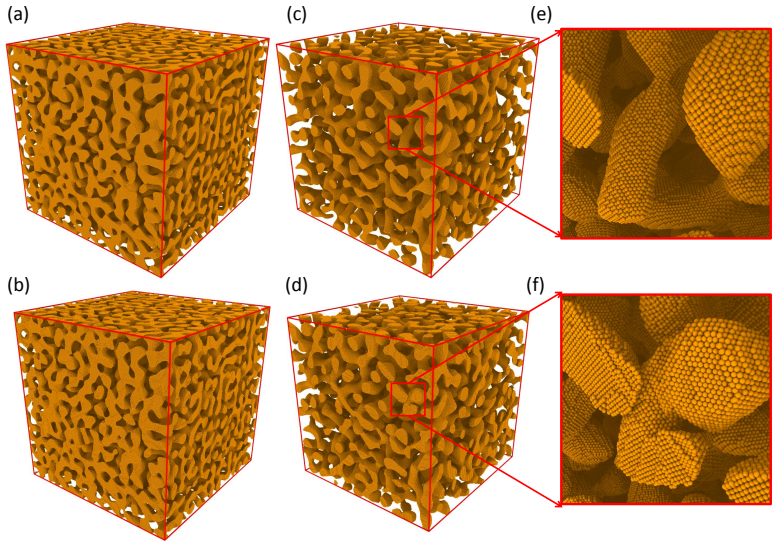

Figure 5.5: Initial and relaxed microstructures of NPG. Different solid fraction initial leveled-wave structures are shown in (a) φ = 0.35 and (c) φ = 0.20. The corresponding molecular dynamic relaxed structures at 300 K for 2 ns are shown in (b) (φ = 0.35) and (d) (φ = 0.20). Figure (e) and (f) are an enlarged region of initial structure (c) and MD relaxed structure (d) of φ = 0.20 respectively. Note that figure (f) shows the reconnections of dangling ligaments during shrinkage and the same magnification was applied when figure (a-d) was rendered. The smaller box size in (d) and (e) represent the volume shrinkage during relaxation.

The initial leveled-wave configurations for φ = 0.35 and 0.20 is shown in Figure 5.5a and c respectively. The structures are shown in Figure 5.5a and c have an identical

ligament size of L=3.5 nm. The sample preparation for shrinkage simulation refers to Section 2.1.4. The microstructures after 2 ns MD relaxation are displayed in Fig. 5.5b (φ = 0.20) and d (φ = 0.35). For structure with initial φ = 0.20, the relaxed structure shows a larger relative volume shrinkage of 0.21 (Figure 5.5d) and new ligaments connections are observed during shrinkage (Figure 5.5f). Here relative volume shrinkage is defined as the ratio between volume change during relaxation simulation, $-\Delta V$, and initial volume, V_0. By contrast, much less $-\Delta V$ (0.07) for the relaxed structure at φ = 0.35 is shown in Figure 5.5c and the microstructure of relaxed structure is similar to the initial configuration in Fig. 5.5a. The relaxed structure of φ also shows no new ligaments connections ((Figure 5.5c and e).

5.2.2 Volume shrinkage and genus

Figure 5.6a plots, $-\Delta V/V_0$, versus relaxation time, t. $-\Delta V/V_0$ initially increases fast and then converges to a stable value. In contrast to a shorter $-\Delta V/V_0$ stabilization time of t=0.4 s for φ = 0.35, 0.30 and 0.25, it takes 4 times longer time for $-\Delta V/V_0$ to become stable for φ = 0.20. Note that the first point of each graph in Figure 5.6a starts from a non-zero value. That small shrinkage comes from the energy minimization step before the thermal relaxation (see Section 2.2.4 for more details of MD shrinkage simulation procedure). The $-\Delta V/V_0$ value at the stable stage represents the total relative volume shrinkage. It is seen that there is more relative volume shrinkage for structures with smaller φ. For example, the relative volume shrinkage increases from 0.07 at φ=0.35 to 0.21 at φ=0.20. The structure with φ = 0.20 shows the largest total relative volume shrinkage of 0.21, which is 2 times the shrinkage of the model with φ = 0.25. For NPG structure, the percolation limit is φ=0.159, if a structure has φ which is less than this value, it can not form as nanoscale network [32]. The value of φ=0.20 is near to the percolation limit, there are more dangling ligaments which makes it much less stable. On the other hand, the ligaments have a high aspect ratio for the structure with φ=0.20. Therefore, they are less stable against the plateau Rayleigh instability.

Figure 5.6b shows the topological genus, G, as a function of relaxation time, t. It is seen that G keeps constant at φ = 0.30 and 0.35 and increases slightly (9%) at φ = 0.25. For the structure with φ = 0.20, G increases around 50% which is consistent with the observation of many new ligaments connections happening during shrinkage as shown in Figure 5.5c and e.

5.2.3 Evolution of connectivity

Next the scaled genus evolution during shrinkage of NPG structure will be explored. Figure 5.7 plots g (Eq. 2.34) versus φ of four various φ leveled-wave configurations during the relaxation. The first data point of each φ structure is set right on the theory line. This observation indicates the validation of our implementation of the leveled-wave model. For the structures with high φ, for instance φ=0.35 and 0.30, g evolves sensibly invariantly during the shrinkage which tells us the densification of the structures leaves the connectivity unchanged. When the initial φ less than 0.30, i.e. φ=0.25 and 0.20, g increases with increasing φ during shrinkage. When

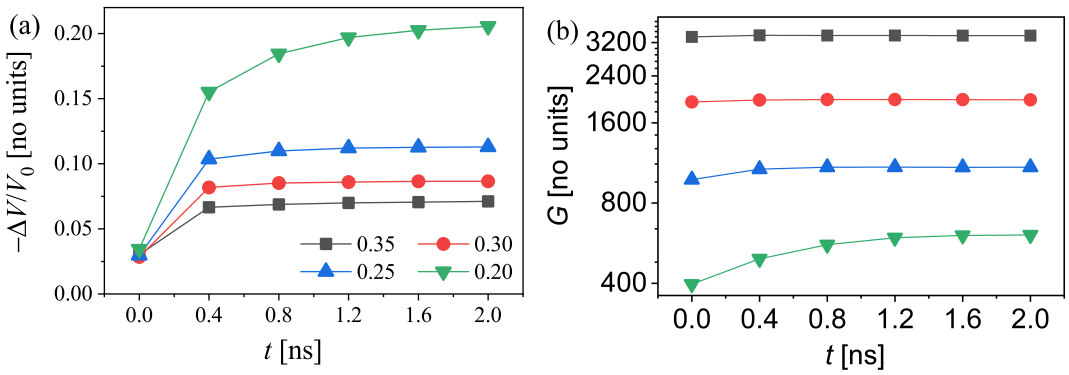

Figure 5.6: Volume shrinkage, $-\Delta V/V_0$, and topological genus, G, evolution during NPG shrinkage. (a) Volume shrinkage, $-\Delta V/V_0$, and (b) genus, G, versus relaxation time, t, for solid fractions φ = 0.20, 0.25, 0.30 and 0.35 of leveled-wave NPG configurations. Here, ΔV represents the change of volume and V_0 is the initial volume.

initial φ less than 0.30, with the smaller initial value of φ, the more φ increased and meanwhile the traces of $g(\varphi)$ slope upwards, indicating that the relaxation will enhance the connectivity. This trend is strong for the structure at φ=0.20. It is seen that g increases by 50% from 0.54 to 0.81 with a final φ=0.25 after relaxation for the structure at initial φ=0.20. The observations can be explained by the fact that there are abundant "dangling" ligaments which are disconnected from the main network in the low φ structure. The densification during shrinkage brings those dangling ends of disconnected ligaments in contact with neighboring ends in the porous structures, thereby resulted in formation of new connections. For denser structures, there are fewer dangling ligaments to re-connect during shrinkage. This re-connection activities are well illustrated in Figure 5.5e and f.

5.2.4 Discussion

Experimental studies on the shrinkage of NPG during dealloying reveal that the shrinkage increases with increasing dealloying potential [5, 29] and the secondary dealloying plays the main role in the shrinkage [29]. Our simulations suggest that the φ of NPG also affects the shrinkage, i.e. the structures at lower φ encountered larger shrinkage during MD relaxation.

It is also noteworthy to point out that our on-lattice dealloying simulations can not involve shrinkage during dealloying. This is because shrinkage requires a displacement of the lattice. Currently, there is no consensus on the mechanisms underlying the shrinkage during dealloying. One mechanism suggests that the origin of such volume shrinkage is the high concentration of lattice defects and local plastic deformation sites [69] initiated by mass transport via plastic flow [110] during the dealloying process. Ye et al. [29] attributed the shrinkage during dealloying to the agglomeration and collapse of injected vacancies, which are induced by the dealloying, shortening the ligament and resulting in the shrinkage of the NPG network. Both of these two mechanisms suggest that the aspect ratio of NPG's ligaments will decrease with shrinkage, thereby enhancing the φ. The shortening of ligaments also implies the network connectivity

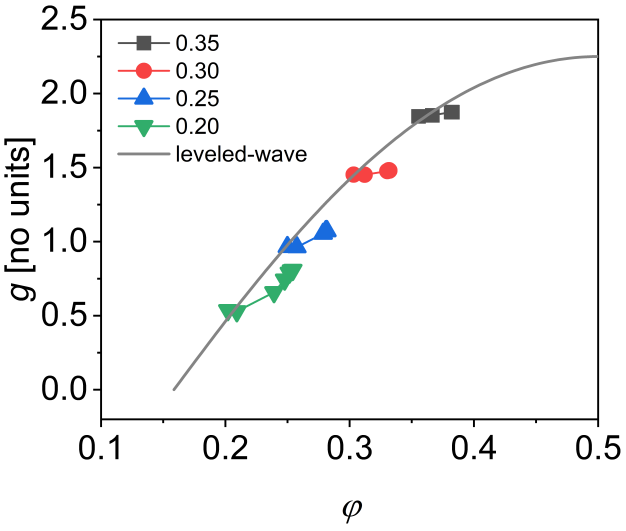

Figure 5.7: Evolution of connectivity during shrinkage of molecular dynamics relaxation. Scaled genus, g, as a function of solid fraction, φ of MD relaxed leveled-wave structures. The solid line represents the theoretical value of connectivity for the leveled-wave initial structures [32]. Symbols are the evolution of g and φ during relaxation of structures with different initial solid fractions, as shown in the legend. The initial point of each structure is sensibly on the theory line and φ increases as the relaxation proceeds. All relaxation simulations are under identical conditions and run for the same time periods.

should be kept unchanged. Our findings of the negligible variation on g during shrinkage at $\varphi \geqslant 0.30$ confirmed that argument of unchanged network connectivity. Yet, the g increases at lower φ especially when $\varphi = 0.20$ during shrinkage. This increase of connectivity at lower φ is a result of the re-connection of the neighboring nodes or longer ligaments (dangling ligaments in the experimental samples) with the contraction of the volume.

5.3 Evolution of connectivity during coarsening

In this section, the connectivity of the coarsening simulations produced structures in Chapter Section 4.2 will be analyzed. Then the evolution of genus and connectivity during coarsening will be explored.

5.3.1 Evolution of genus

Firstly, it is investigated how the network topology evolves during coarsening. Figure 5.8a and 5.8b depict the topological genus, G and the Betti number, B_0 versus coarsening time, t, respectively during coarsening at 900 K. The Betti number reveals the homology group of a structure. The first three Betti numbers are, B_0-the number of connected components, B_1-the number of tunnels, B_2-the number of cavities [144, 145]. Figure 5.8a shows that G stays sensibly invariant for times up to 10^6 s and afterwards G decays drastically with the coarsening time. G decreases faster for the structure

with a less solid fraction φ. Notably, the final G value of the structure with φ = 0.22 approaches zero, indicating a complete disassembly of the sample into isolated dense clusters.

The disassembly into isolated clusters can be inspected by the number of connected components as shown in Figure 5.8b. Samples with $\varphi > 0.35$ retain their initial B_0 value of 1 or change negligibly. In contrast, coarsening significantly increases B_0 of samples with lower φ. For example, while there were roughly 25 connected components in the sample with φ = 0.25 at t = 10^5 s, that value of B_0 increased to ~ 200 at the end of the coarsening process. In other words, what started out as a single connected cluster has now disintegrated into 200 fragments that are disconnected from each other. This increase in the number of connected components in these NPG samples, along with the decrease of the genus G, is due to ligament breaking through pinch-off events, as exemplified in the inset of Figure 5.8a.

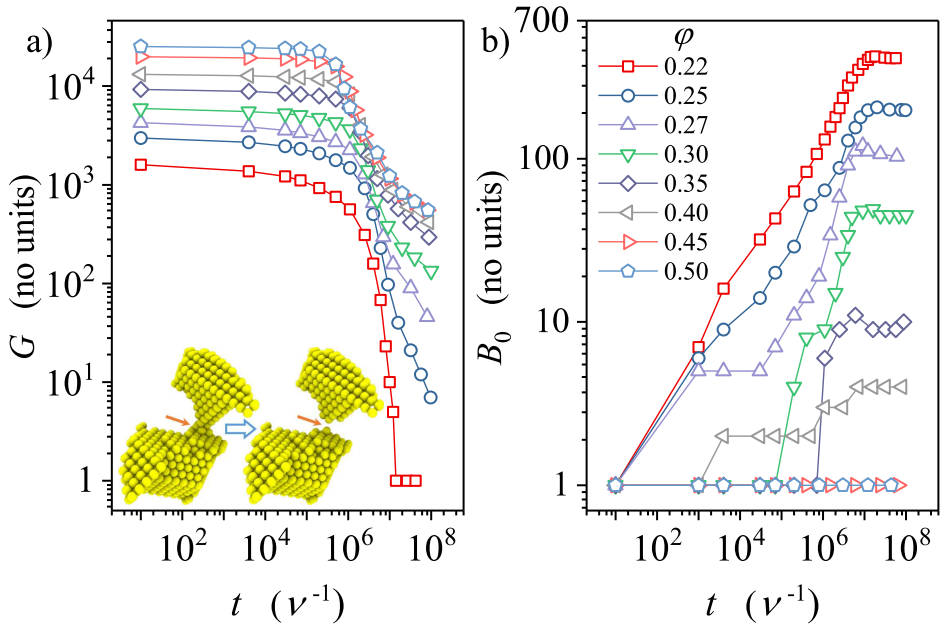

Figure 5.8: Evolution of the topology and isolated clusters during coarsening. The temperature here is 900 K. (a) topological genus, G, of coarsened structure at different solid fraction φ as a function of coarsening time, t. Inset exemplifies a pinch-off event. (b) number of isolated clusters represented by the Betti number, B_0 versus t for structures during coarsening. Note the logarithmic axis. Different symbol shapes of solid fraction, φ are indicated in legend in (b).

Next, let's see the microstructure of coarsened structures. Figure 5.9a-c render the microstructures of coarsened sample with φ=0.22, 0.25 and 0.35, respectively. Each isolated cluster is shown in an individual color. It is seen that the coarsened structure at φ=0.22 forms as all isolated clusters and there are numerous isolated clusters in the coarsened sample with φ=0.25. By contrast, Figure 5.9b shows no isolated clusters for coarsened sample at φ=0.35. The observation is consistent with the finding of increasing of B_0 during coarsening in Figure 5.8b. These disconnected isolated clusters will not bear load when the NPG samples are under compression [82]. Figure 5.9b shows that for the sample with φ=0.25, only a 50% part of the structure can be

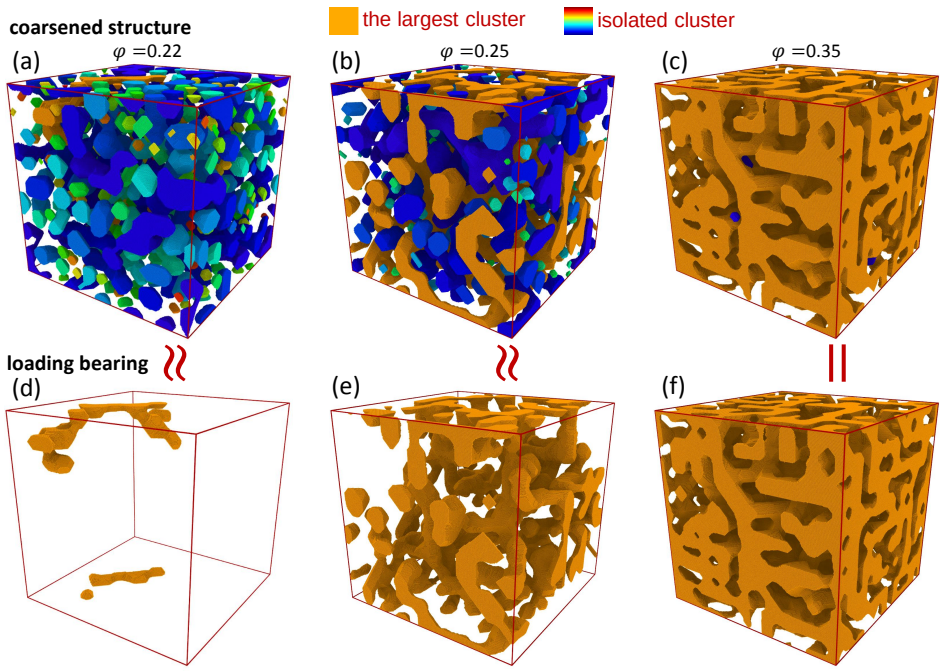

Figure 5.9: Microstructure of coarsened structures. Rendering of coarsened structures with solid fraction φ=0.22 (a), 0.25 (b) and 0.35 (c). The coarsening simulations for (a-c) were run under the same conditions (temperature, T=900 K) and for identical time period of $8\times10^6\nu^{-1}$. Each isolated cluster is distinguished by an individual color. Note all components form as isolated clusters in (a) and many isolated clusters in (b). Load-bearing part of samples for φ=0.22 (d), 0.25 (e) and 0.35 (f). The load-bearing part is the largest cluster and all other isolated clusters are removed. When the NPG sample is under loading, only the largest cluster will bear the loading. Note 50% parts of the structure are removed for coarsened structure at φ=0.25.

the effective load-bearing network after the time range of coarsening in this study. However, the network maintains well connected during coarsening for structure with φ=0.35 (Figure 5.9d).

5.3.2 Evolution of connectivity

In the following section, the evolution of connectivity during coarsening will be shown. For simulations at 900 K, Figure 5.10a reveals the scaled genus, g, (Eq. 2.35) of the largest component versus solid fraction, φ, at different coarsening state which is indicated in the legend. The bold solid line refers to the theory scaled genus value of the initial leveled-wave configurations, which is determined by

$$g = \frac{2\pi\alpha^3}{3\sqrt{3}}(1-\xi^2)e^{-\xi^2/2} \tag{5.1}$$

with $\xi = \sqrt{2}\,\mathrm{erf}^{-1}(2\varphi-1)$ [32]. The symbols represent scaled genus analyzed via eq. 2.35 on the discrete atomic structures generated by our KMC coarsening simulations. It can be seen that for the initial state ($\tilde{L} = \tilde{L}_0$), the numerical analysis underestimates g. The reason for the lower g value than the theory line for discrete atomic structures

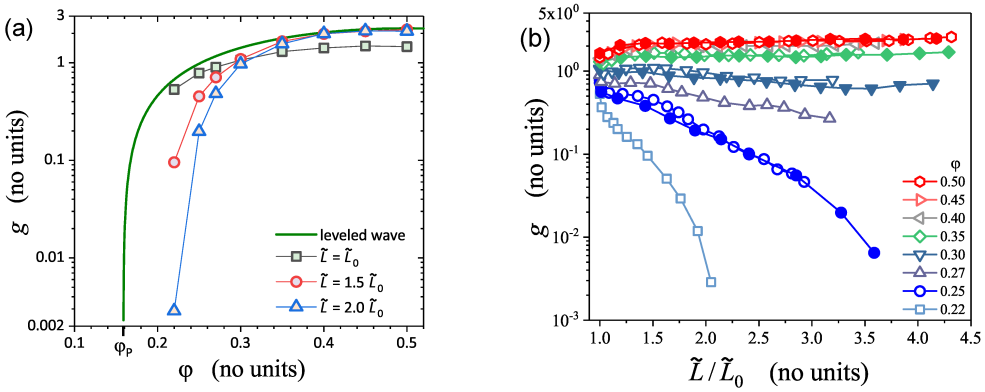

Figure 5.10: Evolution of connectivity during coarsening. (a) Scaled genus, g, as a function of solid fraction, φ, plotted for structures at various coarsening stages. The bold solid green line represents theoretical value of the initial structure from leveled wave model (Eq 5.1); φ_P = 0.159 is the theoretical value of percolation threshold. The open symbols denote numerical results for different coarsening stages: square—initial geometry ($\tilde{L} = \tilde{L}_0$), and coarsened structures to circle—$\tilde{L} = 1.5\tilde{L}_0$ and to triangle—$\tilde{L} = 2.0\tilde{L}_0$, see legend. Note that various evolution of g at different φ: g of structures at $\varphi > 0.3$ converge towards the theoretical line, while structures at $\varphi < 0.3$ move away from it. (b) Scaled genus, g, versus normalized characteristic spacing size, $\tilde{L}/\tilde{L}_0$, between the center of neighboring ligaments. $\tilde{L}_0$ represents the initial value before the onset of coarsening. Each symbol shape corresponds to a various solid fraction, φ, as displayed in legend. Open symbols: coarsening at 900 K; closed symbols: 1800 K. Note the coarsening process tends to decrease the connectivity of structures with $\varphi < 0.3$.

is because $\tilde{L}$ is underestimated by the surface reconstruction algorithm. As coarsening proceeds, the ligament size increases to $\tilde{L} = 1.5\tilde{L}_0$ and then to $\tilde{L} = 2.0\tilde{L}_0$, the scaled genus, g of structures with $\varphi > 0.3$ evolves towards and precisely meets to the theory line. In other words, the connectivity during coarsening keeps invariant for structures at $\varphi > 0.3$. By contrast, during coarsening, g of structures with $\varphi < 0.3$ move away from the theory line of the leveled-wave model. The decreasing trend of g during coarsening is enhanced for the structure with a lesser solid fraction. The more φ approaches the percolation threshold of the theory ($\varphi_P = \frac{1}{2}[1 - \mathrm{erf}(\sqrt{2}^{-1})] \approx 0.16$ [32]), the faster connectivity is lost during coarsening.

To further elucidate the observations above, Figure 5.10b plots g as a function of scaled spacing size, $\tilde{L}/\tilde{L}_0$ for structures with various φ during coarsening at both 900 K and 1800 K temperatures. Here $\tilde{L}_0$ denotes the corresponding spacing size of the initial sample with various φ. In the figure, data points of 900 K runs (open symbols) show excellent agreement with of the 1800 K run (closed symbols). More importantly, it confirms the conclusion that the solid fraction, φ of the sample is a decisive parameter for the evolution trend of connectivity during coarsening. g of structures with $\varphi \geq 0.3$ keeps sensibly invariant during coarsening. At these φ, the structures show self-similar coarsening. By contrast, a decreasing of g is observed for those samples with $\varphi < 0.3$. Furthermore, the lesser φ of the structure, the more prominent the decrease of g. For instance, comparing to the initial value, when the ligaments coarsen to $\tilde{L}/\tilde{L}_0 = 1.5$, the g value of samples with φ= 0.27, 0.25, 0.22 decreases by the factor of 1.3, 1.7 and 5.6 respectively. The difference of that factor between various φ expands when

coarsening proceeds. For example, the g value of structure, when the size grows to $\tilde{L}/\tilde{L}_0$ = 2.0, decreases by the factor of 1.9, 4.0 and 185. The loss of connectivity is consistent with the observations in Figure 5.9 that the structure with φ=0.22 turns into isolated clusters and 50% of component is disconnected for structure with φ=0.25 within the same coarsening time period. These findings in Figure 5.10a and b lead to the conclusion that the solid fraction, φ, is the decisive parameter for the connectivity evolution during coarsening of the nanoporous structure. It suggests that within the range of our simulations, there appears to be a transition between apparently self-similar coarsening for $\varphi \geq 0.3$ and a behavior with progressive loss of connectivity and eventually a percolation-to-cluster transition for $\varphi < 0.3$.

5.3.3 Discussion

Impact of faceting

Depending on the ratio of length over the diameter of slender cylindrical rods, small fluctuations in diameter cause the reduction of the energy and result in pinch-off of the rod by the Plateau-Rayleigh instability [164], as long as the ratio of length over diameter is higher than π. It is expected for this instability to occur even if the ligaments appear short and thick at high φ, since there can be redistribution of matter over distances greater than the "length" of ligaments (the distance between neighboring nodes). Structures at all solid fractions indeed exhibit pinch-off events.

The Plateau-Rayleigh instability is affected by anisotropy of the specific surface free energy, γ, and may slow down when there are steep cusps in γ of crystal surfaces at low-index orientations [165]. Fluctuations that initiate the instability are suppressed when terraces are prevented from rotating out of their low index/low energy orientation by the cusps. It is also possible to influence coarsening exponents by the existence of facets, which result from steep cusps in γ [166]. Hence, the almost perfect facets displayed in the structures at 900 K indicate steep cusps in γ. It is possible to understand the enhanced roughness at 1800 K by recognizing that step-edge excess free-energy (line tension) decreases at higher temperatures as a result of the configurational entropy associated with step-edge fluctuations. Consequently, the cusps become shallower due to the decrease in step-edge energy. Significantly, while faceting or roughness are different between the two temperatures, there is no qualitative difference in coarsening behavior between them. It is noted that there is an abundance of kink sites in all structures, even in the equilibrated small particles of Fig 4.5. In these particles, the number of atoms in the outer surface is insufficient for a perfectly faceted surface, so some kinks are necessary to form such a surface. Kinks provide an alternative pathway for microstructure evolution in network structures due to their easy migration of step edges. This pathway differs from the coordinated rotation of the terraces out of their low-index orientation, as it is considered in Ref [165].

Microfacets have been observed on the surface of NPG in transmission electron micrographs [167], and facets along ligaments have been reported in coarsened NPG [87, 168, 169]. This seems natural, since the Wulff shape of gold retains facets at temperatures close to its melting point [170]. Scanning electron micrographs from other studies of NPG, however, show curved, hence, rough surfaces [20, 82, 86, 95, 96]. In simulations and experiments, however, the time exponent for coarsening is consistent.

The fact that the coarsening kinetics independent of the degree of faceting is significant from this perspective. Even though their confidence limits are wide, our simulation captures fundamental features of experiments on NPG, regardless of the faceting.

Impact of solid faction

The loss of connectivity is of particular relevance when it comes to the coarsening of spinodal structures in polymer blends, where a percolation-to-cluster transition can occur during the coarsening process [138, 171–174]. The transition can be restricted to highly asymmetric blends ($\varphi \ll 0.5$) as described in Ref [174], but it can also take place at any phase fraction [172]. A loss of connections during spinodal coarsening has been demonstrated in experiments [138, 175] and simulations [144]. In an experiment with polymer blends, Ref [138] reported invariant scaled connectivity during coarsening at $\varphi = 0.5$, whereas a tenfold decrease of g at $\varphi = 0.35$, with a fourfold increase in domain size. In our simulation, similar trends are observed. The phase-field investigation conducted in Ref [139] revealed that mixtures undergoing spinodal decomposition via bulk diffusion exhibit bicontinuous structures at phase fractions of $\varphi = 0.5$, 0.40, and 0.36. These mixtures exhibit self-similar coarsening behavior. However, for mixtures with phase fractions of $\varphi = 0.30$ and 0.22, percolation does not occur at any stage of the process.

As one of the major findings of the present study, it is of particular importance to note that the solid fraction is a decisive parameter for the evolution of scaled genus during coarsening by surface diffusion. During coarsening, g remains sensible invariant if $\varphi \geq 0.3$, by contrast, g decreases at lower solid fraction. Once the characteristic length scale reaches twice the initial value, the structure with the smallest φ even decomposes completely. In this context, there are parallels between our observations on surface-transport mediated coarsening of network structures mimicking nanoporous metals by dealloying and those for spinodal decomposition by bulk diffusion in Ref [139]. Yet, the network structures in the present study display substantially greater stability than the spinodal structures at $\varphi = 0.36$. Hence, it is noteworthy that our findings align well with the experimental observations reported in Ref [138] regarding the evolution of the scaled genus in spinodally decomposed polymer blends.

A qualitative interpretation of the link between φ and the variation (or not) of g during coarsening can be derived from the fact that there is a competition between the rate at which ligaments break and the rate at which matter is transported from the damaged ligaments to the surviving ones [82]. It is expected that structures at lower φ have thinner ligaments will undergo faster pinch-off. Yet, since the coarsening scaling law for NPG is independent of φ, for a given value of $\tilde{L}$, the diffusion distance to its neighboring, surviving ligaments is independent of φ. It is, therefore, reasonable to assume that φ will not affect sensibly the time it takes for the material to be re-distributed from the broken ligaments to the neighbors. Consequently, structures with a lesser solid fraction can have more dangling ligaments at any given instant, making them less connected.

Chapter 6

Summary and outlook

6.1 Summary

In this thesis, the microstructure evolution of nanoscale bicontinuous network is studied by the means of KMC and MD simulations. The microstructural features of NPG investigated in this thesis are mainly concentrated on the residual less noble component (silver in silver-gold system) content, characteristic length scale, as well as the topological connectivity.

The KMC dealloying simulations demonstrate, for the first time in the atomistic simulation, that the dealloying process occurs in two stages. During the primary dealloying step, the initial network of nanoscale ligaments is established; during the subsequent secondary dealloying, coarsening and further dissolution proceeds. As a result of primary dealloying, silver clusters are embedded in ligaments with a passivation layer of gold atoms at the surface. At secondary dealloying, the number of silver clusters decreases as ligaments coarsen. The atomistic simulation is well recognized for having been instrumental in identifying and confirming the atomic-scale mechanisms of dealloying. Yet, that only pertains to primary dealloying. This thesis provides for the first time clear and independent evidence, from numerical atomistic simulation, that secondary dealloying can also be understood and acts as has been postulated based on indirect, experimental evidence.

The evolution of the characteristic length scale during dealloying and coarsening was explored:

- The silver cluster size, L_{Ag}, scales with the ligament size, L^0_{lig}, at the end of primary dealloying. Yet, this work for the first time showed that despite the increase in ligament size during secondary dealloying, L_{Ag} remains constant. In light of the finding that L_{Ag} also remains stable after coarsening, postmortem examinations of L_{Ag} in dealloyed NPG may help identify L^0_{lig}, as a crucial characteristic which has been challenging to access by experiment. L_{Ag} can be measured in experiments by TEM [31, 60] and by atom probe tomography [68]. Based on measurements of L_{Ag}, L^0_{lig} can be inferred. Thereby, experiments could provide a database that finally would enable us to conclude on the primary dealloying ligament size.

- The time exponent for coarsening is clearly predicted by early theory, but that

experimental studies of NPG show huge scatter and have not provided a conclusive confirmation. The coarsening simulations in this thesis provided remedies to this issue. According to the coarsening simulations, the coarsening law for characteristic ligament spacing is universal, while this is not the case for the ligament diameter. All the simulation parameters, such as the structure geometry, the driving force and the surface diffusion mechanism, were set in a realistic way. It thus excluded all extrinsic artifacts that the experiments can be suffered. The expected time exponent of $1/4$ for surface-diffusion dominated coarsening process is confirmed in this thesis. Since this thesis shows the largest scale coarsening simulation in the field so far, the resulted exponent of $1/4$ here is quiet convincing. It suggests that deviations from this exponent in the experimental literatures are quite likely due to artifacts, for instance from impurities but possibly also from uncertainties in determining the mean size.

This thesis points out that the solid fraction, φ, plays a significant role in the evolution of nanoporous network's connectivity:

- KMC studies of the dealloying show that the connectivity, g, when $\varphi \geqslant 0.30$ during dealloying, evolves sensibly along with a g-φ curve of the leveled-wave model, whereas g diminishes when $\varphi < 0.30$ for structures dealloyed from the parent alloy of $Ag_{75}Au_{25}$. This is the first time that an atomistic study of the dealloying has looked into the scaled genus and into the suggestion based on the leveled wave model, and therefore entirely indirect, lacking contact to the physics of dealloying - that the scaled genus varies with the solid fraction.

- For NPG structures at $\varphi \geqslant 0.30$, the effect of shrinkage on g is negligible. In contrast, g increases during shrinkage at $\varphi = 0.20$ and at $\varphi = 0.25$ (with lesser increasing). This is the first time that the shrinkage process of nanoporous network is accessed by simulation and the impacts of shrinkage on connectivity are investigated. The findings in this thesis provide fundamental insights to the experimental observations related to shrinkage, such as the unexpected high mechanical property and high volume shrinkage for the NPG samples dealloyed from parent alloy with 20% atom fraction of Au [23, 24].

- Structures with a solid fraction of $\varphi \geqslant 0.30$ maintain their connectivity during coarsening, while those structures with $\varphi < 0.30$ will become more and more disconnected. There are contradictory results in the experiments on the topic of connectivity evolution during coarsening. This thesis provides a conclusive answer to this question. The findings of this study also have implications for the design of lightweight metal network structures. For instance, the hierarchical nested-network nanoporous gold [54] will have more enhancements on mechanical properties when $\varphi \geqslant 0.30$ for each hierarchy-level structures.

6.2 Outlook

This thesis focused on the evolution of NPG microstructures. The evolution of three important microstructural features of nanoporous networks was studied: the resid-

ual less noble component content, the characteristic length scale, and the topological connectivity. Some questions need further investigation.

Firstly, in the KMC dealloying simulation, the redeposition of Ag atoms during the corrosion of Ag, which is essential in experiments, was not considered in the present algorithm. Thus, it is worth including the Ag redeposition in the KMC model.

Secondly, in experiments, volume shrinkage happens simultaneously during dealloying and coarsening. While, in this thesis, the dealloying, shrinkage and coarsening have to be studied separately. It is worth developing new simulation strategies to combine the KMC (-dealloying or -coarsening) and MD (shrinkage) simulation to study those processes in a more realize manner.

Thirdly, how those microstructural features influence the mechanical properties of NPG is worth to further study. It is worth studying the impact of the residual less noble component content and its distribution on the mechanical properties of NP metals. The evolution of connectivity of nanoporous network during coarsening is studied in this thesis, while a quantitative relation of g and mechanical properties of coarsened structure is worth further investigation.

References

[1] G Gottstein. Physical foundations of materials science, 2004.

[2] William D Callister and David G Rethwisch. *Materials science and engineering: an introduction*, volume 9. Wiley New York, 2018.

[3] K Sieradzki and RC Newman. Stress-corrosion cracking. *Journal of physics and chemistry of solids*, 48(11):1101–1113, 1987.

[4] Juergen Biener, Andrea M Hodge, Joel R Hayes, Cynthia A Volkert, Luis A Zepeda-Ruiz, Alex V Hamza, and Farid F Abraham. Size effects on the mechanical behavior of nanoporous au. *Nano letters*, 6(10):2379–2382, 2006.

[5] S Parida, D Kramer, CA Volkert, H Rösner, J Erlebacher, and J Weissmüller. Volume change during the formation of nanoporous gold by dealloying. *Physical Review Letters*, 97(3):035504, 2006.

[6] Haijun Jin, Lilia Kurmanaeva, Jörg Schmauch, Harald Rösner, Yulia Ivanisenko, and Jörg Weissmüller. Deforming nanoporous metal: Role of lattice coherency. *Acta Materialia*, 57(9):2665–2672, 2009.

[7] H-J Jin, Dominik Kramer, Yulia Ivanisenko, and Jörg Weissmüller. Macroscopically strong nanoporous pt prepared by dealloying. *Advanced Engineering Materials*, 9(10):849–854, 2007.

[8] Shan Shi, Jürgen Markmann, and Jörg Weissmüller. Actuation by hydrogen electrosorption in hierarchical nanoporous palladium. *Philosophical Magazine*, 97(19):1571–1587, 2017.

[9] Shan Shi, Jürgen Markmann, and Jörg Weissmüller. Verifying larché–cahn elasticity, a milestone of 20th-century thermodynamics. *Proceedings of the National Academy of Sciences*, 115(43):10914–10919, 2018.

[10] Congcheng Wang and Qing Chen. Reduction-induced decomposition: spontaneous formation of monolithic nanoporous metals of tunable structural hierarchy and porosity. *Chemistry of Materials*, 30(11):3894–3900, 2018.

[11] Mei Yan. Nanoporous copper metal catalyst in click chemistry: Nanoporosity dependent activity without supports and bases. In *Development of New Catalytic Performance of Nanoporous Metals for Organic Reactions*, pages 17–53. Springer, 2014.

[12] Lukas Lührs and Jörg Weissmüller. Nanoporous copper-nickel–macroscopic bodies of a strong and deformable nanoporous base metal by dealloying. *Scripta Materialia*, 155:119–123, 2018.

[13] Yi-Hou Xiang, Ling-Zhi Liu, Jun-Chao Shao, and Hai-Jun Jin. A universal scaling relationship between the strength and young's modulus of dealloyed porous fe0. 80cr0. 20. *Acta Materialia*, 186:105–115, 2020.

[14] Denis Garoli, Andrea Schirato, Giorgia Giovannini, Sandro Cattarin, Paolo Ponzellini, Eugenio Calandrini, Remo Proietti Zaccaria, Francesco D'Amico, Maria Pachetti, Wei Yang, et al. Galvanic replacement reaction as a route to prepare nanoporous aluminum for uv plasmonics. *Nanomaterials*, 10(1):102, 2020.

[15] Wei Yang, Zhao-Ping Luo, Wei-Kang Bao, Hui Xie, Ze-Sheng You, and Hai-Jun Jin. Light, strong, and stable nanoporous aluminum with native oxide shell. *Science Advances*, 7(28):eabb9471, 2021.

[16] Ilya Vladimirovich Okulov, Sviatlana V Lamaka, Takeshi Wada, Kunio Yubuta, Mikhail L Zheludkevich, Jörg Weissmüller, Jürgen Markmann, and Hidemi Kato. Nanoporous magnesium. *Nano Research*, 11(12):6428–6435, 2018.

[17] Hua-Jun Qiu, Gang Fang, Yuren Wen, Pan Liu, Guoqiang Xie, Xingjun Liu, and Shuhui Sun. Nanoporous high-entropy alloys for highly stable and efficient catalysts. *Journal of Materials Chemistry A*, 7(11):6499–6506, 2019.

[18] Rui-Qi Yao, Yi-Tong Zhou, Hang Shi, Wu-Bin Wan, Qing-Hua Zhang, Lin Gu, Yong-Fu Zhu, Zi Wen, Xing-You Lang, and Qing Jiang. Nanoporous surface high-entropy alloys as highly efficient multisite electrocatalysts for nonacidic hydrogen evolution reaction. *Advanced Functional Materials*, 31(10):2009613, 2021.

[19] Soo-Hyun Joo, Jae Wung Bae, Won-Young Park, Yusuke Shimada, Takeshi Wada, Hyoung Seop Kim, Akira Takeuchi, Toyohiko J Konno, Hidemi Kato, and Ilya V Okulov. Beating thermal coarsening in nanoporous materials via high-entropy design. *Advanced Materials*, 32(6):1906160, 2020.

[20] Kaixiong Hu, Markus Ziehmer, Ke Wang, and Erica T Lilleodden. Nanoporous gold: 3d structural analyses of representative volumes and their implications on scaling relations of mechanical behaviour. *Philosophical Magazine*, 96(32-34): 3322–3335, 2016.

[21] Markus Ziehmer, Kaixiong Hu, Ke Wang, and Erica T Lilleodden. A principle curvatures analysis of the isothermal evolution of nanoporous gold: Quantifying the characteristic length-scales. *Acta materialia*, 120:24–31, 2016.

[22] Erica T Lilleodden and Peter W Voorhees. On the topological, morphological, and microstructural characterization of nanoporous metals. *MRS bulletin*, 43(1): 20–26, 2018.

[23] Birthe Zandersons, Lukas Lührs, Yong Li, and Jörg Weissmüller. On factors defining the mechanical behavior of nanoporous gold. *Acta Materialia*, 215:116979, 2021.

[24] Ling-Zhi Liu, Ye-Yuan Zhang, Hui Xie, and Hai-Jun Jin. Transition from homogeneous to localized deformation in nanoporous gold. *Physical Review Letters*, 127(9):095501, 2021.

[25] Dirk Jalas, L-H Shao, Rashmi Canchi, Toshiya Okuma, Slawa Lang, Alexander Petrov, Jörg Weissmüller, and Manfred Eich. Electrochemical tuning of the optical properties of nanoporous gold. *Scientific reports*, 7(1):1–8, 2017.

[26] Dominik Kramer, Raghavan Nadar Viswanath, and Jörg Weissmüller. Surface-stress induced macroscopic bending of nanoporous gold cantilevers. *Nano Letters*, 4(5):793–796, 2004.

[27] A Wittstock, V Zielasek, J Biener, CM Friend, and M Bäumer. Nanoporous gold catalysts for selective gas-phase oxidative coupling of methanol at low temperature. *Science*, 327(5963):319–322, 2010.

[28] Xingyou Lang, Akihiko Hirata, Takeshi Fujita, and Mingwei Chen. Nanoporous metal/oxide hybrid electrodes for electrochemical supercapacitors. *Nature nanotechnology*, 6(4):232–236, 2011.

[29] Xinglong Ye, Ning Lu, Xiaoju Li, Kui Du, Jun Tan, and Haijun Jin. Primary and secondary dealloying of Au (Pt)-Ag: structural and compositional evolutions, and volume shrinkage. *Journal of The Electrochemical Society*, 161(12):C517–C526, 2014.

[30] Matthias Graf, Benedikt Roschning, and Jörg Weissmüller. Nanoporous gold by alloy corrosion: Method-structure-property relationships. *Journal of The Electrochemical Society*, 164(4):C194–C200, 2017.

[31] Tobias Krekeler, Anastasia V Straßer, Matthias Graf, Ke Wang, Christian Hartig, Martin Ritter, and Jörg Weissmüller. Silver-rich clusters in nanoporous gold. *Materials Research Letters*, 5(5):314–321, 2017.

[32] Celal Soyarslan, Swantje Bargmann, Marc Pradas, and Jörg Weissmüller. 3D stochastic bicontinuous microstructures: Generation, topology and elasticity. *Acta Materialia*, 149:326–340, 2018.

[33] Hai-Jun Jin, Xiao-Lan Wang, Smrutiranjan Parida, Ke Wang, Masahiro Seo, and Jörg Weissmüller. Nanoporous au- pt alloys as large strain electrochemical actuators. *Nano letters*, 10(1):187–194, 2010.

[34] E Detsi, ZG Chen, WP Vellinga, PR Onck, and J Th M De Hosson. Actuating and sensing properties of nanoporous gold. *Journal of nanoscience and nanotechnology*, 12(6):4951–4955, 2012.

[35] Xing-Long Ye and Hai-Jun Jin. Sealing-free fast-response paraffin/nanoporous gold hybrid actuator. *Nanotechnology*, 28(38):385501, 2017.

[36] Huajun Qiu, Luyan Xue, Guanglei Ji, Guiping Zhou, Xirong Huang, Yinbo Qu, and Peiji Gao. Enzyme-modified nanoporous gold-based electrochemical biosensors. *Biosensors and Bioelectronics*, 24(10):3014–3018, 2009.

[37] Charlotte Stenner, Li-Hua Shao, Nadiia Mameka, and Jörg Weissmüller. Piezoelectric gold: Strong charge-load response in a metal-based hybrid nanomaterial. *Advanced Functional Materials*, 26(28):5174–5181, 2016.

[38] Erkin Şeker, Wei-Chuan Shih, and Keith J. Stine. Nanoporous metals by alloy corrosion: Bioanalytical and biomedical applications. *MRS Bulletin*, 43(1):49–56, 2018.

[39] Jay Patel, Logudurai Radhakrishnan, Bo Zhao, Badharinadh Uppalapati, Rodney C Daniels, Kevin R Ward, and Maryanne M Collinson. Electrochemical properties of nanostructured porous gold electrodes in biofouling solutions. *Analytical chemistry*, 85(23):11610–11618, 2013.

[40] Wei-Chuan Shih, Greggy M Santos, Fusheng Zhao, Oussama Zenasni, and Md Masud Parvez Arnob. Simultaneous chemical and refractive index sensing in the 1–2.5 μm near-infrared wavelength range on nanoporous gold disks. *Nano letters*, 16(7):4641–4647, 2016.

[41] Daniel A McCurry and Ryan C Bailey. Nanoporous gold membranes as robust constructs for selectively tunable chemical transport. *The Journal of Physical Chemistry C*, 120(37):20929–20935, 2016.

[42] Caixia Xu, Jixin Su, Xiaohong Xu, Pengpeng Liu, Hongjuan Zhao, Fang Tian, and Yi Ding. Low temperature CO oxidation over unsupported nanoporous gold. *Journal of the American Chemical Society*, 129(1):42–43, 2007.

[43] Y. Ding and M. W. Chen. Nanoporous metals for catalytic and optical applications. *MRS Bulletin*, 34:569–576, 2009.

[44] Yan Yu, Lin Gu, Xingyou Lang, Changbao Zhu, Takeshi Fujita, MingWei Chen, and Joachim Maier. Li storage in 3d nanoporous au-supported nanocrystalline tin. *Advanced Materials*, 23(21):2443–2447, 2011.

[45] Qing Chen, Yi Ding, and Mingwei Chen. Nanoporous metal by dealloying for electrochemical energy conversion and storage. *MRS Bulletin*, 43(1):43–48, 2018.

[46] Juergen Biener, Andrea M Hodge, Alex V Hamza, Luke M Hsiung, and Joe H Satcher Jr. Nanoporous au: A high yield strength material. *Journal of applied physics*, 97(2):024301, 2005.

[47] CA Volkert, ET Lilleodden, D Kramer, and J Weissmüller. Approaching the theoretical strength in nanoporous au. *Applied Physics Letters*, 89(6):061920, 2006.

[48] Nicolas J Briot, Tobias Kennerknecht, Christoph Eberl, and T John Balk. Mechanical properties of bulk single crystalline nanoporous gold investigated by millimetre-scale tension and compression testing. *Philosophical Magazine*, 94(8): 847–866, 2014.

[49] Douglas A Crowson, Diana Farkas, and Sean G Corcoran. Mechanical stability of nanoporous metals with small ligament sizes. *Scripta Materialia*, 61(5):497–499, 2009.

[50] Jonah Erlebacher, Michael J Aziz, Alain Karma, Nikolay Dimitrov, and Karl Sieradzki. Evolution of nanoporosity in dealloying. *nature*, 410(6827):450, 2001.

[51] J Rugolo, J Erlebacher, and Karl Sieradzki. Length scales in alloy dissolution and measurement of absolute interfacial free energy. *Nature materials*, 5(12): 946–949, 2006.

[52] Yi Ding and Jonah Erlebacher. Nanoporous metals with controlled multimodal pore size distribution. *Journal of the American Chemical Society*, 125(26):7772–7773, 2003.

[53] Zhen Qi and Jörg Weissmüller. Hierarchical nested-network nanostructure by dealloying. *Acs Nano*, 7(7):5948–5954, 2013.

[54] Shan Shi, Yong Li, Bao-Nam Ngo-Dinh, Jürgen Markmann, and Jörg Weissmüller. Scaling behavior of stiffness and strength of hierarchical network nanomaterials. *Science*, 371(6533):1026–1033, 2021.

[55] Jonah Erlebacher. An atomistic description of dealloying porosity evolution, the critical potential, and rate-limiting behavior. *Journal of the Electrochemical Society*, 151(10):C614–C626, 2004.

[56] AM Hodge, RT Doucette, MM Biener, J Biener, O Cervantes, and AV Hamza. Ag effects on the elastic modulus values of nanoporous au foams. *Journal of Materials Research*, 24(4):1600–1606, 2009.

[57] Ling Zhang, Luyang Chen, Hongwen Liu, Ying Hou, Akihiko Hirata, Takeshi Fujita, and Mingwei Chen. Effect of residual silver on surface-enhanced raman scattering of dealloyed nanoporous gold. *The Journal of Physical Chemistry C*, 115(40):19583–19587, 2011.

[58] Arne Wittstock and Marcus Bäumer. Catalysis by unsupported skeletal gold catalysts. *Accounts of chemical research*, 47(3):731–739, 2014.

[59] LC Wang, Y Zhong, D Widmann, J Weissmüller, and RJ Behm. On the role of residual ag in nanoporous au catalysts for co oxidation: a combined microreactor and tap reactor study. *ChemCatChem*, 4(2):251–259, 2012.

[60] Christoph Mahr, Paromita Kundu, Anastasia Lackmann, Daniele Zanaga, Karsten Thiel, Marco Schowalter, Martin Schwan, Sara Bals, Arne Wittstock, and Andreas Rosenauer. Quantitative determination of residual silver distribution in nanoporous gold and its influence on structure and catalytic performance. *Journal of catalysis*, 352:52–58, 2017.

[61] Anastasia Lackmann, Marcus Bäumer, Gunther Wittstock, and Arne Wittstock. Independent control over residual silver content of nanoporous gold by galvanodynamically controlled dealloying. *Nanoscale*, 10(36):17166–17173, 2018.

[62] DM Artymowicz, J Erlebacher, and RC Newman. Relationship between the parting limit for de-alloying and a particular geometric high-density site percolation threshold. *Philosophical Magazine*, 89(21):1663–1693, 2009.

[63] Zhen Qi, Ulla Vainio, Andreas Kornowski, Martin Ritter, Horst Weller, Haijun Jin, and Jörg Weissmüller. Porous gold with a nested-network architecture and ultrafine structure. *Advanced Functional Materials*, 25(17):2530–2536, 2015.

[64] Wilke Dononelli, Gabriele Tomaschun, Thorsten Klüner, and Lyudmila V Moskaleva. Understanding oxygen activation on nanoporous gold. *ACS Catalysis*, 9(6):5204–5216, 2019.

[65] Alex Ricardo Silva Olaya, Franziska Kühling, Christoph Mahr, Birthe Zandersons, Andreas Rosenauer, Jörg Weissmüller, and Gunther Wittstock. Promoting effect of the residual silver on the electrocatalytic oxidation of methanol and its intermediates on nanoporous gold. *ACS catalysis*, 12(8):4415–4429, 2022.

[66] Jonah Erlebacher. Mechanism of coarsening and bubble formation in high-genus nanoporous metals. *Physical review letters*, 106(22):225504, 2011.

[67] I. McCue, J. Snyder, X. Li, Q. Chen, K. Sieradzki, and J. Erlebacher. Apparent inverse gibbs-thomson effect in dealloyed nanoporous nanoparticles. *Physical Review Letters*, 108(22), 2012.

[68] A. A. El-Zoka, B. Langelier, G. A. Botton, and R. C. Newman. Enhanced analysis of nanoporous gold by atom probe tomography. *Materials Characterization*, 128: 269–277, 2017.

[69] S. Parida, D. Kramer, C. A. Volkert, H. Rösner, J. Erlebacher, and J. Weissmüller. Volume change during the formation of nanoporous gold by dealloying. *Physical Review Letters*, 97(3):035504, 2006.

[70] Bao Lin, Lingxue Kong, Peter D Hodgson, Stephen Mudie, Adrian Hawley, and Ludovic F Dumée. Controlled porosity and pore size of nano-porous gold by thermally assisted chemical dealloying–a saxs study. *RSC advances*, 7(18):10821–10830, 2017.

[71] LH Qian and Mingwei Chen. Ultrafine nanoporous gold by low-temperature dealloying and kinetics of nanopore formation. *Applied Physics Letters*, 91(8): 083105, 2007.

[72] Dylan V Pugh, Aziz Dursun, and Sean G Corcoran. Electrochemical and morphological characterization of pt–cu dealloying. *Journal of the electrochemical society*, 152(11):B455, 2005.

[73] Yi Ding, Y-J Kim, and Jonah Erlebacher. Nanoporous gold leaf:"ancient technology"/advanced material. *Advanced Materials*, 16(21):1897–1900, 2004.

[74] EG Seebauer and CE Allen. Estimating surface diffusion coefficients. *Progress in surface science*, 49(3):265–330, 1995.

[75] DV Pugh, A Dursun, and SG Corcoran. Formation of nanoporous platinum by selective dissolution of cu from cu 0.75 pt 0.25. *Journal of materials research*, 18 (1):216–221, 2003.

[76] Shan Shi, Jürgen Markmann, and Jörg Weissmüller. Synthesis of uniform bulk nanoporous palladium with tunable structure. *Electrochimica acta*, 285:60–69, 2018.

[77] Rong Li and Karl Sieradzki. Ductile-brittle transition in random porous Au. *Physical Review Letters*, 68(8):1168, 1992.

[78] Yu-chen Karen Chen, Yong S Chu, JaeMock Yi, Ian McNulty, Qun Shen, Peter W Voorhees, and David C Dunand. Morphological and topological analysis of coarsened nanoporous gold by x-ray nanotomography. *Applied Physics Letters*, 96(4):043122, 2010.

[79] Giorgio Pia, Alberto Cincotti, and Francesco Delogu. Thermally and catalytically induced coarsening of nanoporous au. *Materials Letters*, 183:114–116, 2016.

[80] LH Qian, XQ Yan, T Fujita, A Inoue, and MW Chen. Surface enhanced raman scattering of nanoporous gold: Smaller pore sizes stronger enhancements. *Applied Physics Letters*, 90(15):153120, 2007.

[81] Anant Mathur and Jonah Erlebacher. Size dependence of effective young's modulus of nanoporous gold. *Applied physics letters*, 90(6):061910, 2007.

[82] Lingzhi Liu, Xinglong Ye, and Haijun Jin. Interpreting anomalous low-strength and low-stiffness of nanoporous gold: Quantification of network connectivity. *Acta Materialia*, 118:77–87, 2016.

[83] Haijun Jin, Jörg Weissmüller, and Diana Farkas. Mechanical response of nanoporous metals: A story of size, surface stress, and severed struts. *MRS Bulletin*, 43(1):35–42, 2018.

[84] Conyers Herring. Effect of change of scale on sintering phenomena. *Journal of Applied Physics*, 21(4):301–303, 1950.

[85] Giorgio Pia and Francesco Delogu. Coarsening of nanoporous au: Relationship between structure and mechanical properties. *Acta Materialia*, 99:29–38, 2015.

[86] Satoko Kuwano-Nakatani, Takeshi Fujita, Kazuki Uchisawa, Daichi Umetsu, Yu Kase, Yusuke Kowata, Katsuhiko Chiba, Tomoharu Tokunaga, Shigeo Arai, Yuta Yamamoto, et al. Environment-sensitive thermal coarsening of nanoporous gold. *Materials Transactions*, 56(4):468–472, 2015.

[87] Yuchen Karen Chen-Wiegart, Steve Wang, Yong S Chu, Wenjun Liu, Ian McNulty, Peter W Voorhees, and David C Dunand. Structural evolution of nanoporous gold during thermal coarsening. *Acta materialia*, 60(12):4972–4981, 2012.

[88] AM Hodge, J Biener, JR Hayes, PM Bythrow, CA Volkert, and AV Hamza. Scaling equation for yield strength of nanoporous open-cell foams. *Acta Materialia*, 55(4):1343–1349, 2007.

[89] Nicolas J. Briot, Tobias Kennerknecht, Christoph Eberl, and T. John Balk. Mechanical properties of bulk single crystalline nanoporous gold investigated by millimetre-scale tension and compression testing. *Phil. Mag.*, 94(8):847–866, 2014.

[90] H. J. Jin and J. Weissmüller. A material with electrically tunable strength and flow stress. *Science*, 332(6034):1179–1182, 2011.

[91] Nadiia Mameka, Jürgen Markmann, and Jörg Weissmüller. On the impact of capillarity for strength at the nanoscale. *Nature Communications*, 8(1):1976, 2017.

[92] Lukas Lührs, Birthe Zandersons, Norbert Huber, and Jörg Weissmüller. Plastic poisson's ratio of nanoporous metals: A macroscopic signature of tension–compression asymmetry at the nanoscale. *Nano Letters*, 17(10):6258–6266, 2017.

[93] Shaofeng Sun, Xiying Chen, Nilesh Badwe, and Karl Sieradzki. Potential-dependent dynamic fracture of nanoporous gold. *Nat Mater*, 14(9):894–898, 2015.

[94] N Badwe, X Chen, DK Schreiber, MJ Olszta, NR Overman, EK Karasz, AY Tse, SM Bruemmer, and K Sieradzki. Decoupling the role of stress and corrosion in the intergranular cracking of noble-metal alloys. *Nature materials*, 17(10): 887–893, 2018.

[95] Nadiia Mameka, Ke Wang, Jürgen Markmann, Erica T Lilleodden, and Jörg Weissmüller. Nanoporous gold-testing macro-scale samples to probe small-scale mechanical behavior. *Materials Research Letters*, 4(1):27–36, 2016.

[96] KR Mangipudi, E Epler, and CA Volkert. Morphological similarity and structure-dependent scaling laws of nanoporous gold from different synthesis methods. *Acta Materialia*, 140:337–343, 2017.

[97] Ling-Zhi Liu and Hai-Jun Jin. Scaling equation for the elastic modulus of nanoporous gold with "fixed" network connectivity. *Applied Physics Letters*, 110 (21):211902, 2017.

[98] Norbert Huber. Connections between topology and macroscopic mechanical properties of three-dimensional open-pore materials. *Frontiers in Materials*, 5:69, 2018.

[99] Bao-Nam Dinh Ngô, Alexander Stukowski, Nadiia Mameka, Jürgen Markmann, Karsten Albe, and Jörg Weissmüller. Anomalous compliance and early yielding of nanoporous gold. *Acta Materialia*, 93:144–155, 2015.

[100] Lingzhi Liu and Haijun Jin. Scaling equation for the elastic modulus of nanoporous gold with "fixed" network connectivity. *Applied Physics Letters*, 110(21):211902, 2017.

[101] Norbert Huber. Connections between topology and macroscopic mechanical properties of three-dimensional open-pore materials. *Frontiers in Materials*, 5:69, 2018.

[102] Diana Farkas, Alfredo Caro, Eduardo Bringa, and Douglas Crowson. Mechanical response of nanoporous gold. *Acta Materialia*, 61(9):3249–3256, 2013.

[103] Xiao-Yu Sun, Guang-Kui Xu, Xiaoyan Li, Xi-Qiao Feng, and Huajian Gao. Mechanical properties and scaling laws of nanoporous gold. *Journal of Applied Physics*, 113(2):023505, 2013.

[104] Hansol Jeon, Na-Ri Kang, Eun-Ji Gwak, Jae-il Jang, Heung Nam Han, Jun Yeon Hwang, Sukbin Lee, and Ju-Young Kim. Self-similarity in the structure of coarsened nanoporous gold. *Scripta Materialia*, 137:46–49, 2017.

[105] Yongwoo Kwon, Katsuyo Thornton, and Peter W Voorhees. Coarsening of bicontinuous structures via nonconserved and conserved dynamics. *Physical Review E*, 75(2):021120, 2007.

[106] Yongwoo Kwon, K Thornton, and PW Voorhees. Morphology and topology in coarsening of domains via non-conserved and conserved dynamics. *Philosophical Magazine*, 90(1-4):317–335, 2010.

[107] M. Graf, B. Roschning, and J. Weissmüller. Nanoporous gold by alloy corrosion: Method-structure-property relationships. *Journal of The Electrochemical Society*, 164(4):C194–C200, 2017.

[108] Erkin Seker, Michael L Reed, and Matthew R Begley. A thermal treatment approach to reduce microscale void formation in blanket nanoporous gold films. *Scripta Materialia*, 60(6):435–438, 2009.

[109] Yu-chen Karen Chen-Wiegart, Steve Wang, Ian McNulty, and David C Dunand. Effect of ag–au composition and acid concentration on dealloying front velocity and cracking during nanoporous gold formation. *Acta materialia*, 61(15):5561–5570, 2013.

[110] Ke Ma, John S Corsi, Jintao Fu, and Eric Detsi. Origin of the volume contraction during nanoporous gold formation by dealloying for high-performance electrochemical applications. *ACS Applied Nano Materials*, 1(2):541–546, 2018.

[111] John W. Cahn. Phase separation by spinodal decomposition in isotropic systems. *The Journal of Chemical Physics*, 42(1):93–99, 1965.

[112] C. J. Dotzler, B. Ingham, B. N. Illy, K. Wallwork, M. P. Ryan, and M. F. Toney. In situ observation of strain development and porosity evolution in nanoporous gold foils. *Advanced Functional Materials*, 21(20):3938–3946, 2011.

[113] Bao Lin, Lingxue Kong, Peter D Hodgson, Stephen Mudie, Adrian Hawley, and Ludovic F Dumée. Controlled porosity and pore size of nano-porous gold by thermally assisted chemical dealloying–a saxs study. *RSC advances*, 7(18):10821–10830, 2017.

[114] Daan Frenkel and Berend Smit. *Understanding molecular simulation: from algorithms to applications*, volume 1. Elsevier, 2001.

[115] Alexander Stukowski. Visualization and analysis of atomistic simulation data with ovito–the open visualization tool. *Modelling and Simulation in Materials Science and Engineering*, 18(1):015012, 2009.

[116] Nicholas Metropolis, Arianna W Rosenbluth, Marshall N Rosenbluth, Augusta H Teller, and Edward Teller. Equation of state calculations by fast computing machines. *The journal of chemical physics*, 21(6):1087–1092, 1953.

[117] Michael P Allen and Dominic J Tildesley. *Computer simulation of liquids*. Oxford university press, 2017.

[118] Alfred B Bortz, Malvin H Kalos, and Joel L Lebowitz. A new algorithm for monte carlo simulation of ising spin systems. *Journal of Computational Physics*, 17(1):10–18, 1975.

[119] HC Kang and WH Weinberg. Dynamic monte carlo with a proper energy barrier: surface diffusion and two-dimensional domain ordering. *The Journal of chemical physics*, 90(5):2824–2830, 1989.

[120] Kristen A Fichthorn and W Hh Weinberg. Theoretical foundations of dynamical monte carlo simulations. *The Journal of chemical physics*, 95(2):1090–1096, 1991.

[121] Mie Andersen, Chiara Panosetti, and Karsten Reuter. A practical guide to surface kinetic monte carlo simulations. *Frontiers in chemistry*, 7:202, 2019.

[122] Jonah D Erlebacher. Kinetic rate law issues in the morphological relaxation of rippled crystal surfaces. In *Dynamics of Crystal Surfaces and Interfaces*, pages 97–107. Springer, 2002.

[123] Peter Kratzer. Monte carlo and kinetic monte carlo methods. *arXiv preprint arXiv:0904.2556*, 2009.

[124] J. Erlebacher. Mechanism of coarsening and bubble formation in high-genus nanoporous metals. *Physical Review Letters*, 106(22):225504, 2011.

[125] Peter Haasen. *Physical Metallurgy*. Cambridge University Press, 2013.

[126] Corbett C. Battaile. The kinetic monte carlo method: Foundation, implementation, and application. *Computer Methods in Applied Mechanics and Engineering*, 197(41-42):3386–3398, 2008.

[127] Steve Plimpton, Corbett Battaile, Mike Chandross, Liz Holm, Aidan Thompson, Veena Tikare, Greg Wagner, E Webb, X Zhou, C Garcia Cardona, et al. Crossing the mesoscale no-man's land via parallel kinetic monte carlo. *Sandia Report SAND 2009-6226*, 2009. URL `http://spparks.sandia.gov/`.

[128] Y. Umeno, C. Elsässer, B. Meyer, P. Gumbsch, M. Nothacker, J. Weissmüller, and F. Evers. Ab initio study of surface stress response to charging. *Epl*, 78(1): 13001, 2007.

[129] Julius Koettgen, Tobias Zacherle, Steffen Grieshammer, and Manfred Martin. Ab initio calculation of the attempt frequency of oxygen diffusion in pure and samarium doped ceria. *Physical Chemistry Chemical Physics*, 19(15):9957–9973, 2017.

[130] Steve Plimpton. Fast parallel algorithms for short-range molecular dynamics. Technical report, Sandia National Labs., Albuquerque, NM (United States), 1993.

[131] SM Foiles, MI Baskes, and Murray S Daw. Embedded-atom-method functions for the fcc metals cu, ag, au, ni, pd, pt, and their alloys. *Physical review B*, 33 (12):7983, 1986.

[132] Shuichi Nosé. A unified formulation of the constant temperature molecular dynamics methods. *The Journal of chemical physics*, 81(1):511–519, 1984.

[133] William G Hoover. Canonical dynamics: Equilibrium phase-space distributions. *Physical review A*, 31(3):1695, 1985.

[134] Matthias Graf, Bao-Nam Dinh Ngô, Jörg Weissmüller, and Jürgen Markmann. X-ray studies of nanoporous gold: Powder diffraction by large crystals with small holes. *Physical review materials*, 1(7):076003, 2017.

[135] Jörg Löffler and Jörg Weissmüller. Grain-boundary atomic structure in nanocrystalline palladium from x-ray atomic distribution functions. *Physical review B*, 52 (10):7076, 1995.

[136] J Markmann, V Yamakov, and J Weissmüller. Validating grain size analysis from x-ray line broadening: a virtual experiment. *Scripta Materialia*, 59(1): 15–18, 2008.

[137] P Debye, HR Anderson Jr, and H Brumberger. Scattering by an inhomogeneous solid. ii. the correlation function and its application. *Journal of applied Physics*, 28(6):679–683, 1957.

[138] Carlos R. Lopez-Barron and Christopher W. Macosko. Characterizing interface shape evolution in immiscible polymer blends via 3d image analysis. *Langmuir*, 25(16):9392–9404, 2009.

[139] Yongwoo Kwon, K. Thornton, and P. W. Voorhees. Morphology and topology in coarsening of domains via non-conserved and conserved dynamics. *Philosophical Magazine*, 90(1-4):317–335, 2010.

[140] S. Cattarin, D. Kramer, A. Lui, and M. M. Musiani. Preparation and characterization of gold nanostructures of controlled dimension by electrochemical techniques. *Journal of Physical Chemistry C*, 111(34):12643–12649, 2007.

[141] C. Lakshmanan, R. N. Viswanath, S. R. Polaki, R. Rajaraman, S. Dash, and A. K. Tyagi. Surface area of nanoporous gold: Effect on temperature. *Electrochimica Acta*, 182:565–572, 2015.

[142] Alexander Stukowski. Computational analysis methods in atomistic modeling of crystals. *JOM*, 66(3):399–407, 2014.

[143] Wikipedia. Genus (mathematics), 12. 2022. URL `https://en.wikipedia.org/wiki/Genus_(mathematics)`.

[144] Marcio Gameiro, Konstantin Mischaikow, and Thomas Wanner. Evolution of pattern complexity in the cahn–hilliard theory of phase separation. *Acta Materialia*, 53(3):693–704, 2005.

[145] Tomasz Kaczynski, Konstantin Mischaikow, and Marian Mrozek. *Computational Homology*. Springer, 2006.

[146] Friedrich Ernst Peter Hirzebruch and Matthias Kreck. On the concept of genus in topology and complex analysis. *Notices of the American Mathematical Society*, 56(6):713–719, 2009.

[147] Tomasz Kaczynski, Konstantin Michael Mischaikow, and Marian Mrozek. *Computational homology*, volume 3. Springer, 2004.

[148] Konstantin Mischaikow, Hiroshi Kokubu, Marian Mrozek, Pawe Pilarczyk, Tomas Gedeon, Jean-Philippe Lessard, and Marcio Gameiro. Chomp: Computational homology project. *Software available at http://chomp. rutgers. edu*, 2014.

[149] K. Sieradzki, N. Dimitrov, D. Movrin, C. McCall, N. Vasiljevic, and J. Erlebacher. The dealloying critical potential. *Journal of the Electrochemical Society*, 149(8): B370–B377, 2002.

[150] Yong Li, Bao-Nam Dinh Ngô, Jürgen Markmann, and Jörg Weissmüller. Topology evolution during coarsening of nanoscale metal network structures. *Physical review materials*, 3(7):076001, 2019.

[151] K. Sieradzki. Curvature effects in alloy dissolution. *Journal of the Electrochemical Society*, 140(10):2868–2872, 1993.

[152] J. Rugolo, J. Erlebacher, and K. Sieradzki. Length scales in alloy dissolution and measurement of absolute interfacial free energy. *Nature Materials*, 5(12):946–949, 2006.

[153] J. Weissmüller, R. C. Newman, H. J. Jin, A. M. Hodge, and J. W. Kysar. Nanoporous metals by alloy corrosion: Formation and mechanical properties. *MRS Bulletin*, 34(8):577–586, 2009.

[154] K Sieradzki, JS Kim, AT Cole, and RC Newman. The relationship between dealloying and transgranular stress-corrosion cracking of Cu-Zn and Cu-Al alloys. *Journal of The Electrochemical Society*, 134(7):1635–1639, 1987.

[155] K Sieradzki, RR Corderman, K Shukla, and RC Newman. Computer simulations of corrosion: selective dissolution of binary alloys. *Philosophical Magazine A*, 59 (4):713–746, 1989.

[156] Qing Chen and Karl Sieradzki. Mechanisms and morphology evolution in dealloying. *Journal of The Electrochemical Society*, 160(6):C226, 2013.

[157] J. M. Dona and J. Gonzalez-Velasco. The dependence of the surface-diffusion coefficients of gold atoms on the potential - its influence on reconstruction of metal lattices. *Surface Science*, 274(2):205–214, 1992.

[158] J. M. Dona and J. Gonzalez-Velasco. Mechanism of surface-diffusion of gold adatoms in contact with an electrolytic solution. *Journal of Physical Chemistry*, 97(18):4714–4719, 1993.

[159] Xiaoqian Li, Qing Chen, Ian McCue, Joshua Snyder, Peter Crozier, Jonah Erlebacher, and Karl Sieradzki. Dealloying of noble-metal alloy nanoparticles. *Nano letters*, 14(5):2569–2577, 2014.

[160] J. Erlebacher, M. J. Aziz, A. Karma, N. Dimitrov, and K. Sieradzki. Evolution of nanoporosity in dealloying. *Nature*, 410(6827):450–453, 2001.

[161] Tobias Krekeler, Anastasia V. Straßer, Matthias Graf, Ke Wang, Christian Hartig, Martin Ritter, and Jörg Weissmüller. Silver-rich clusters in nanoporous gold. *Materials Research Letters*, 5:314–321, 2017.

[162] Xing-Long Ye, Ning Lu, Xiao-Ju Li, Kui Du, Jun Tan, and Hai-Jun Jin. Primary and secondary dealloying of au(pt)-ag: Structural and compositional evolutions, and volume shrinkage. *Journal of The Electrochemical Society*, 161(12):C517–C526, 2014.

[163] Matthias Graf, Bao-Nam Dinh Ngô, Jörg Weissmüller, and Jürgen Markmann. X-ray studies of nanoporous gold: Powder diffraction by large crystals with small holes. *Physical Review Materials*, 1(7):076003, 2017.

[164] LordRayleigh. On the instability of jets. *Proceedings of the London Mathematical Society*, s1-10(1):4–13, 1878.

[165] JW Cahn. Stability of rods with anisotropic surface free energy. *Scripta Metallurgica*, 13(11):1069–1071, 1979.

[166] S. Biagi, C. Misbah, and P. Politi. Universality classes for unstable crystal growth. *Physical Review E*, 89(6):13, 2014.

[167] Takeshi Fujita, Pengfei Guan, Keith McKenna, Xingyou Lang, Akihiko Hirata, Ling Zhang, Tomoharu Tokunaga, Shigeo Arai, Yuta Yamamoto, Nobuo Tanaka, Yoshifumi Ishikawa, Naoki Asao, Yoshinori Yamamoto, Jonah Erlebacher, and

Mingwei Chen. Atomic origins of the high catalytic activity of nanoporous gold. *Nature Materials*, 11(9):775–780, 2012.

[168] F. Kertis, J. Snyder, Lata Govada, Sahir Khurshid, N. Chayen, and J. Erlebacher. Structure/processing relationships in the fabrication of nanoporous gold. *JOM*, 62(6):50–56, 2010.

[169] Ye Sun, Sofie A. Burger, and T. John Balk. Controlled ligament coarsening in nanoporous gold by annealing in vacuum versus nitrogen. *Philosophical Magazine*, 94(10):1001–1011, 2014.

[170] Hila Sadan and Wayne D. Kaplan. Au–sapphire (0001) solid–solid interfacial energy. *Journal of Materials Science*, 41(16):5099–5107, 2006.

[171] J. Läuger, R. Lay, and W. Gronski. The percolation-to-cluster transition during spinodal decomposition of an off-critical polymer mixture. observation by light scattering and optical microscopy. *The Journal of Chemical Physics*, 101(8): 7181–7184, 1994.

[172] JeKyun Lee and ChangDae Han. Evolution of a dispersed morphology from a co-continuous morphology in immiscible polymer blends. *Polymer*, 40(10):2521–2536, 1999.

[173] I. Demyanchuk, S. A. Wieczorek, and R. Holyst. Percolation-to-droplets transition during spinodal decomposition in polymer blends, morphology analysis. *Journal of Chemical Physics*, 121(2):1141–1147, 2004.

[174] D. Y. Hsu, C. M. Chou, C. Y. Chuang, and P. D. Hong. Percolation of phase-separating polymer mixtures. *Acs Macro Letters*, 4(12):1341–1345, 2015.

[175] J. M. Hyde, M. K. Miller, M. G. Hetherington, A. Cerezo, G. D. W. Smith, and C. M. Elliott. Spinodal decomposition in fe-cr alloys: Experimental study at the atomic level and comparison with computer models—iii. development of morphology. *Acta Metallurgica et Materialia*, 43(9):3415–3426, 1995.

Publications & Conferences

Publications

1. G. Henkelmann, D. Waldow, M. Liu, L. Lührs, Y. Li, J. Weissmüller. **Self-Detachment and Subsurface Densification of Dealloyed Nanoporous Thin Films**, *Nano Letters*, (2022) 6787-6793.

2. T. Sardhara, R. Aydin, Y. Li, N. Piché, R. Gauvin, C. J. Cyron, M. Ritter. **Training deep neural networks to reconstruct nanoporous structures from FIB tomography images using synthetic training data**, *Frontiers in materials*, (2022) 2296.

3. Y. Li, B.-N. D. Ngô, J. Markmann, J. Weissmüller. **Evolution of length scales and of chemical heterogeneity during primary and secondary dealloying**, *Acta Materialia*, (2021) 117424.

4. S. Shi, Y. Li, B.-N. D. Ngô, J. Markmann, J. Weissmüller. **Scaling behaviour of stiffness and strength of hierarchical network nanomaterials**, *Science*, 371 (6533) (2021) 1026–1033.

5. B. Zandersons, L. Lührs, Y Li, J Markmann, J Weissmüller. **On factors defining the mechanical behavior of nanoporous gold**, *Acta Materialia*, (2021) 116979.

6. Y. Li, B.-N. D. Ngô, J. Markmann, J. Weissmüller. **Datasets for the microstructure of nanoscale metal network structures and for its evolution during coarsening**, *Data in Brief*, 29 (2020) 105030.

7. Y. Li, B.-N. D. Ngô, J. Markmann, J. Weissmüller. **Topology evolution during coarsening of nanoscale metal network structures**, *Physical Review Materials*, 3 (2019) 076001.

Conference contributions

1. Y Li, J Markmann, and J Weissmüller. **Evolution of length scales and connectivity during dealloying of nanoporous metals**, Fourth International Symposium on Nanoporous Materials by Alloy Corrosion, 23-26 April 2023, Lake Bostal, Germany. (*Poster presentation*)

2. Y Li, J Markmann, and J Weissmüller. **Silver-rich clusters reveal the initial ligament size during nanoporous gold dealloying via kinetic Monte Carlo simulation**, DPG Meeting (German Physical Society), 27 September-01 October 2021, Online conference, Germany. (*Oral presentation*)

3. Y Li, B-N D Ngô, J Markmann, and J Weissmüller. **Microstructure evolution of silver-rich clusters during nanoporous gold dealloying**, MSE 2020-Material Science and Engineering conference, 20-25 September 2020, Darmstadt (online conference), Germany. (*Oral presentation*)

4. Y Li, B-N D Ngô, J Markmann, and J Weissmüller. **Topology evolution during coarsening of nanoporous gold via kinetic Monte Carlo simulation**, Intergranular and Interphase Boundaries in Materials conference, 01-05 July 2019, Paris, France. (*Poster presentation*)

5. Y Li, B-N D Ngô, J Markmann, and J Weissmüller. **Topology evolution during coarsening of nanoporous gold via kinetic Monte Carlo simulation**, DPG Spring Meeting (German Physical Society), 01-05 April 2019, Regensburg, Germany. (*Oral presentation*)

Zusammenfassung

Summary

This thesis explores the evolution of these microstructural features: residual silver, characteristic length scale, and topological connectivity in nanoporous gold (NPG). Kinetic Monte Carlo was used to simulate the dealloying and coarsening processes. Molecular Dynamics was used to simulate the shrinkage process of NPG structures. It is found that the dealloying occurs in two stages. In the primary dealloying, silver clusters are embedded in the ligaments; in the secondary dealloying, the number of silver clusters is reduced. The silver cluster size retains constant during the whole dealloying and scales with the initial ligament size established in the primary dealloying. The finding of coarsening law provides a conclusive confirmation for scattered experimental results. This thesis points out that the solid fraction plays a significant role in the evolution of the nanoporous network's connectivity during the dealloying, coarsening and shrinkage processes.

Zusammenfassung

In dieser Arbeit wird die Entwicklung der folgenden mikrostrukturellen Merkmale untersucht: Restsilber, charakteristische Längenskala und topologische Konnektivität in nanoporösem Gold (NPG). Die kinetische Monte-Carlo-Methode wurde verwendet, um die Entlegierungs und Vergröberungsprozesse zu simulieren. Der Schrumpfungsprozess der NPG-Strukturen wurde mit Molekulardynamik simuliert. Es wurde festgestellt, dass die Entlegierung in zwei Phasen abläuft. Beim primären Entlegieren werden Silbercluster in die Ligamente eingebettet; beim sekundären Entlegieren wird die Anzahl der Silbercluster reduziert. Die Größe der Silbercluster bleibt während des gesamten Entlegieren konstant und skaliert mit der ursprünglichen Ligamentgröße, die beim primären Entlegieren festgelegt wurde. Die Feststellung des Vergröberungsgesetzes liefert Erklärung für verstreute experimentelle Ergebnisse. Diese Arbeit zeigt, dass der Feststoffanteil eine wichtige Rolle bei der Entwicklung der Konnektivität des nanoporösen Netzwerks während der Entlegierungs, Vergröberungs und Schrumpfungsprozesse spielt.